EFFECT OF SURFACE TREATMENT ON THE MECHANICAL PROPERTIES OF THE POLYSULFONE-Al/Li BONDED SYSTEM INCLUDING THIN FILM STUDIES OF MOISTURE INTRUSION AND THE VISCOELASTIC RESPONSE OF THE INTERPHASE REGION

by

Chan Uk Ko

Dissertation submitted to the Faculty of the Virginia Polytechnic Institute and State University in partial fulfillment of the requirements for the degree of:

Doctor of Philosophy

in

Materials Engineering Science

APPROVED:

Dr. J.P. Wightman, Chairman

Dr. H.F. Brinson

Dr. J.G. Dillard

Dr. N.S. Eiss

Dr. T.C. Ward

April, 1988

Blacksburg, Virginia

SURFACE CHARACTERISTICS OF THE POLYSULFONE-Al/Li BONDED SYSTEM INCLUDING THIN FILM STUDIES OF MOISTURE INTRUSION AND THE VISCOELASTIC RESPONSE OF THE INTERPHASE REGION

by

Chan U. Ko

Committee Chairman: James P. Wightman
Materials Engineering Science

CSL 12/6/88

(ABSTRACT)

An investigation of polysulfone-Al/Li alloy interaction involved single lap shear joints and wedge samples following an FPL etch, sulfuric acid anodization (SAA) and phosphoric acid anodization (PAA). The study of the Al/Li surfaces involved the determination of the elemental composition and morphological features of the pretreated adherend before bonding and following failure. When thermoplastic polysulfone (PSF) was either thermally pressed or primed onto the microporous surface, the PSF indeed penetrated into the porous oxide and thereby provided a mechanical means of adhesion. The wedge test results for the adherend pretreated by PAA and SAA were superior to those for the FPL etched adherend. The failure path for the FPL etched samples was at the adhesive/oxide interface whereas the failure path for the SAA and PAA samples was within the adhesive but with occasional divergence of the crack into the oxide. The porous oxides on Al/Li alloy formed after PAA and SAA treatment were shown to undergo dramatic changes in morphology on short term (<90 hrs) exposure to 71 C and

100 % R.H. environment. The mechanism of failure was due to moisture which caused slight hydration of the Al/Li oxide and subsequent debonding of the PSF from the oxide layer. Lithium was not concentrated at the surface in the PAA treated Al/Li alloy as shown by AES depth profiling. The effect of lithium on the durability of the bonded alloy is considered minimal. Along these lines, cyclic loading, use of primers, and infrared spectroscopy studies have been carried out.

The mode of moisture intrusion into the polysulfone-Al/Li oxide interphase region is discussed. Specifically, water molecules diffuse into the polysulfone rather than transporting along the interface. Moisture then attacks the oxide interface.

Thin polysulfone coatings on pretreated aluminum surfaces were characterized utilizing dynamic mechanical thermal analysis (DMTA), and dielectric thermal analysis (DETA) to detect changes in the molecular motions and structural transitions in the polysulfone-aluminum interphase. The order of the loss peak temperature of the polysulfone is, PSF coating on a porous Al > PSF coating on a smooth Al > neat PSF film. The activation energy of relaxation is also lower for neat PSF when compared to the thin film cast onto a smooth Al or a porous PAA Al substrate. The loss peak temperature shift and the higher activation energy associated with the coated films can be explained by the entropy being reduced when the chains are laid down in two dimensions. Thus studies of polymer properties in the interphase region will contribute to the understanding of the adhesive-adherend interaction.

ACKNOWLEDGEMENTS

I would like to express my sincere thanks and gratitude to Dr. J.P. Wightman for his constant guidance, suggestions, and enthusiasm throughout the fulfillment of this degree and the writing of this dissertation. I am also thankful that he provided the opportunities to attend meetings and meet scientists in the field. Enabling funds to attend the Adhesion Society meetings were generously provided by the Center for Adhesion Science at Virginia Tech. I like to thank Dr. H.F. Brinson, Dr. J.G. Dillard, Dr. N.S. Eiss, and Dr. T.C. Ward for serving on my committee and for the valuable suggestions, and Dr. K. Wefers of Alcoa for the helpful questions.

I would like to thank for keeping the surface analysis instruments running, for help in obtaining the TEM and EDX data. D. Lefebvre for help on the cyclic load testing, E. Balcells in Dr. Ward's group for his discussions in regard to viscoelastic studies and obtaining DETA data, and for proofreading this dissertation. I would also like to thank the people in the Physics machine shop (Fred, Melvin, and John) for their help with designing and building equipment for this research.

Finally, I would like to thank my wife , for her patience, understanding, and support throughout my graduate studies.

TABLE OF CONTENTS

LIST OF FIGURES

LIST OF TABLES

CHAPTER I

INTRODUCTION

Adhesion is defined as the state in which two surfaces are held together by interfacial forces of attraction, owing to the interactions of molecules, atoms, and ions in the two surfaces. These forces range in magnitude from the strong chemical bonds formed when two atoms share electrons, or when electric charges attract each other, to the comparatively weak attractive forces, known as van der Waals interactions, which are found whenever two substances are placed in intimate contact (1).

In describing the interactions between an adhesive and an adherend, it may not be sufficient to consider the bulk properties of the materials involved. Thus, Sharpe (2) has introduced the concept of a three dimensional 'interphase' to describe this zone between bulk adhesive and bulk adherend. This zone extends from some point in the adherend where the local properties begin to change from the bulk properties, through the interface, and into the adhesive where the local properties approach that of the bulk properties. This interphase region can extend from a few to a few hundred nanometers, depending on the actual adhesive-adherend system. The interphase region is schematically shown in Figure 1.

One of the most important requirements of a structurally bonded joint is the ability to retain its load-bearing capability for long periods under the wide

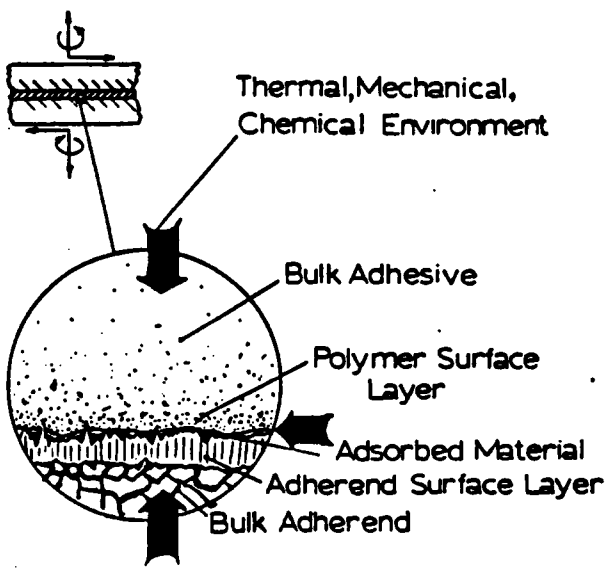

Figure 1. Schematic representation of the polymer-metal interphase (3).

variety of environmental conditions which are encountered during its service life. One of the most commonly encountered hostile environments is water and by far the most important challenge facing the adhesion community is that of long-term durability of adhesive joints exposed to environments where the activity of either water liquid or vapor is high (4-6).

Also, one of the key issues in adhesion science today is the role of the interphase region in influencing adhesion. This interphase region has to be characterized in terms of the physical and chemical structure as well as the mechanical properties. However, it is very difficult to measure in-situ properties of an ultra-thin region (<100nm).

The objective of this work is, first, to determine the performance of pretreated Al/Li 2090 adherend bonded with polysulfone and relate this to mechanical properties of the bonded joint. Emphasis is placed on the wedge test results of polysulfone bonded Al/Li samples subjected to a hostile environment and the use of surface analysis technique to investigate the Al/Li surfaces to study the failure mechanism of bonded joints. Secondly, to determine the mode of moisture intrusion into the polysulfone-aluminum interface by utilizing the aluminum oxide to aluminum hydroxide transformation. Specifically, the goal was to study whether the moisture is diffusing through the polysulfone adhesive or transporting along the polymer-oxide interface. This is the first instance in which this oxide-to-hydroxide transformation is used as an indicator for moisture intrusion into the aluminum oxide-

polymer interface. Thirdly, to determine the linear dynamic viscoelastic behavior of thin polysulfone coatings on pretreated aluminum surfaces utilizing dynamic mechanical thermal analysis (DMTA), and dielectric thermal analysis (DETA). Neat films of polysulfone and thin polysulfone films coated onto a smooth Al substrate and a porous Al substrate were compared. The goal here was to determine whether the polymer which penetrated the porous oxide has a different material property than the polymer in the bulk.

CHAPTER II

LITERATURE REVIEW

Prior to discussing the present research, a literature review on the intrinsic adhesion forces which act across the adhesive/adherend interface, thermodynamic interfacial contact, bond durability, surface pretreatments, conformation of polymer chains, and the polymer-metal interface will be presented and used in discussion of the present results.

A. Adhesion Mechanism

Various theories have been proposed to explain the mechanism by which polymers adhere to a metal substrate. The four main mechanisms of adhesion will be described briefly.

1. Adsorption Theory

In the chemical adhesion theory, the formation of specific primary bonds at the interface is assumed. That is ionic, covalent and metallic bonds may operate across the interface. Different types of primary bonds across an interface have been reported in the literature (7-10). For instance, Klein et al. (10) reported infrared evidence of covalent primary bonds between a polyurethane adhesive and epoxy-based primers, which gave the high joint strengths. Secondary bonds such as van der Waals forces act between the atoms in the two surfaces. The estimated bond energies for different types of bonding are given in Table 1. Secondary bond forces between two phases due to only dispersion forces have been calculated by Huntsberger

TABLE 1. Various types of bonds with estimates of the range of magnitude of their respective bond energies (11).

Bond Type	Bond Energy (kJ/mol)
Primary bonds	
Ionic	590-1050
Covalent	63-710
Metallic	113-347
Secondary bonds	
Hydrogen bonds (involving F)	42 maximum
Hydrogen bonds (excluding F)	10-26
Dipole-dipole	4-21
Dispersion (London) forces	0.08-42

(13) who reported that the force of attraction between infinite parallel plates is about 100 MPa at a separation distance of 1 nanometer. The experimental values were much lower than the theoretical value due to voids and defects, which caused failure at much lower than calculated loads.

Hydrogen bonds, the energy of which lies just above that of van der Waals bonds as shown in Table 1, appear to enhance adhesion. Kusaka and Suetaka (14) utilized attenuated total reflectance infrared spectroscopy to study the adhesion between a cyanoacrylate adhesive and an anodized aluminum substrate. A lowering of the C=O stretching frequency and a shift of the antisymmetric stretching vibration of the C-O-C group to a higher frequency was observed in the infrared spectrum of the cyanoacrylate when it was adsorbed onto the aluminum surface. These changes were interpreted as being due to the formation of interfacial hydrogen bonds between the carbonyl groups in the adhesive and polar groups on the aluminum oxide surface.

2. Mechanical Interlocking Theory

In the mechanical interlocking theory, the adhesive penetrates into the irregularities of the substrate surface and thus provide mechanical anchoring of the adhesive to the substrate. Although Tabor and Winterton (15), who studied the adhesion between two perfectly smooth mica surfaces clearly demonstrated that adhesion may be obtained with smooth surfaces thus making the mechanical interlocking theory not totally applicable. However, in the adhesion of rubber textiles, interlocking

indeed plays a role, as shown by Wake (16). Bikerman explains the adhesion of paper and cardboard also in terms of mechanical adhesion (17). Venables (18), and Arrowsmith and Clifford (19) have discussed the role of mechanical interlocking and chemical bond formation in adhesive bonding. Venables estimated from the dimensions and density of protrusions that the increase in the interfacial area available for chemical bonding was about 10 %, whereas peel adhesion increased tenfold when protrusions were present. Mechanical interlocking and whisker reinforcement of the epoxy adhesive therefore play a role in enhancing adhesive bond strengths.

Packham (20) also reported improvements in joint strength when a microfibrous surface topography is created. In his studies on the adhesion of polyethylene to metallic substrates, he found that high peel strengths were obtained when a very rough, microfibrous, oxide surface was produced on a copper substrate. When the fibers were damaged, which reduced the capability for mechanical interlocking without detectably having changed the chemical nature of the substrate, the joint strength dropped markedly.

3. Diffusion Theory

This adhesion mechanism is mainly for polymer-polymer interactions. The solubility parameter, δ_m, of a polymer can be expressed as:

$$\delta_m = ((H_v - RT) / V)^{1/2} \qquad [1]$$

where H_v is the molar heat of vaporization, R is the gas constant, T is the temperature (K) and V is the molar volume. The diffusion theory requires that the

macromolecules or chain segments of the polymer possess sufficient mobility and are mutually soluble.

These requirements are usually met in the autohesion of elastomers and in the solvent welding of compatible, amorphous plastics. In these examples, interdiffusion does significantly contribute to adhesion. However, where the solubility parameters of the materials are not similar, or one polymer is highly crosslinked, crystalline or below its glass transition temperature, then interdiffusion is an unlikely mechanism of adhesion.

Direct experimental evidence for interdiffusion in compatible polymers has been reported. Radiometric studies (21) have demonstrated the presence of macromolecular diffusion with a diffusion coefficient on the order of 10^{-11} to 10^{-14} cm^2/s, which according to Voyutskii (22) is completely adequate for the formation of a strong interface between polystyrene and poly-n-butyl acrylate after a contact time of only a few seconds. Wu et al. (23) studied the interfacial structure and diffusion kinetics of two compatible polymers, poly(methyl methacrylate) and poly(vinylidene fluoride), in a melt and reported that the interdiffusion rates of the two components are unequal, giving unequal diffusion coefficients, a net mass flow across the interface, and an asymmetric interfacial composition profile.

4. Electrostatic Theory

Deryaguin (24,25) treats the adhesive/substrate system as a capacitor which is charged due to the contact of the two different materials. Separation of the parts of the capacitor, as during interface rupture, leads to a

separation of charge and to a potential difference which increases until a discharge occurs. Adhesion is assumed to be due to the existence of these attractive forces across the electrical double layer. Except at very low pressures, this theory requires a variation of the measured work of adhesion with the pressure of the gas in which the adhesive fracture tests are conducted. Deryaguin has equated the measured work of adhesion, determined from peel tests, with the calculated electrical energy stored in a capacitor and reported good agreement between the two quantities. Also, there was a dependence of the peel energy on the gas pressure. However, Weidner (26) has repeated the experiment and found no difference in the peel strength of pressure-sensitive tapes under vacuum as opposed to atmospheric pressure. Further, the majority of the measured work of adhesion is dissipated through viscous and visco-elastic responses of the materials and this energy should not have been included in the value equated with the electrical energy. Also, any electrical phenomena observed during the joint fracture process probably arise from the failure event, rather than cause the adhesion between the materials. Therefore, it appears that for most adhesive/substrate systems, any electrical double layer which is generated does not contribute significantly to adhesion.

The different experimental conditions, as well as the complex character of the interphase region between the metal surface and the adhesive, prevent the development of a single theory of adhesion. Each of the theories explains only a part of the bonding phenomenon.

When an adhesive is brought into contact with an adherend, the first requirement of adhesion is good wetting which has both a thermodynamic and a kinetic component and is discussed next.

B. Interfacial Contact

1. Work of Adhesion Equation

The equilibrium contact angle (θ) of a liquid on a solid surface represents the balance of the attraction between molecules in the first few molecular layers of both phases and the extent of interaction between solid and liquid molecules in their free surfaces. Dupre (27) showed that the reversible work of separation (W_A) per unit area of solid and liquid is given by,

$$W_A = \gamma_{sv} + \gamma_{lv} - \gamma_{sl} \qquad [2]$$

where γ_{sv} is the surface free energy of the solid substrate, γ_{lv} is the surface free energy of the liquid adhesive, and γ_{sl} is the interfacial tension as shown in Figure 2. It was shown by Young (28) that the different tensions acting in the interfaces at the three phase contact line may be resolved by vectors in a direction parallel to the surface.

$$\gamma_{sl} - \gamma_{sv} + \gamma_{lv} \cos\theta = 0 \qquad [3]$$

This is the well known Young equation. However, it was Bangham and Razouk (29) who identified the need to write the surface tensions of liquid and solid in equilibrium with the saturated vapor to account for the adsorption of liquid vapor on the solid surface. The equilibrium spreading pressure is expressed as

$$\Pi_e = \gamma_s - \gamma_{sv} \qquad [4]$$

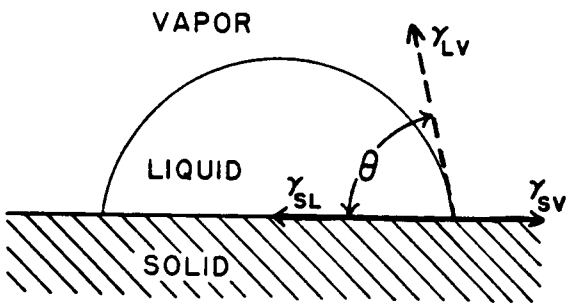

Figure 2. Schematic diagram of forces governing a contact angle (63).

Equations [2], [3] and [4] may be combined to give the Young-Dupre equation

$$W_A = \gamma_{lv} (1 + \cos \theta) + \Pi_e \qquad [5]$$

However, $\Pi_e \approx 0$ for liquids that form finite contact angles on organic solids (30).

Fowkes (31) proposed that the surface free energy of a pure phase may be represented by the sum of contributions arising from the different types of intermolecular forces. Fowkes (32) has suggested these forces include dispersion (d), polar (p), and hydrogen bonding (h), but Schultz et al. (33) have suggested that all polar interactions including hydrogen bonding interactions be considered as one term or

$$\gamma = \gamma^D + \gamma^P \qquad [6]$$

Kaelble and Uy (34) have proposed that the geometric mean of the dispersion force components is a reliable prediction of the interaction energies at the interface caused by dispersion forces. This assumption may be used to give a relation for the work of adhesion in a solid-liquid system as

$$W_A = 2(\gamma_s^D \gamma_a^D)^{1/2} + 2(\gamma_s^P \gamma_a^P)^{1/2} \qquad [7]$$

where γ_s represents the substrate and γ_a represents the adhesive.

The work of Donnet (35) demonstrates the effect of the surface treatment of aluminum on the surface energetics and work of adhesion to NBR (butadiene-acrylonitrile) and SBR (styrene-butadiene) elastomers. The surface free energy of a high energy substrate such as aluminum was determined by measuring the contact angle between the surface and two immiscible liquid phases (36).

Values of γ_s^p and γ_s^d for the differently pretreated aluminum surfaces are shown in Table 2. Calculated values of the work of adhesion of these surfaces to NBR and SBR are shown in Table 3. The measured adhesive strengths were found to be in the order: anodized Al > anodized sealed Al > phosphatized Al. The expected order for adhesive strength from Table 3 was, however, anodized > phosphatized Al > anodized sealed Al. The reason for this reversal was that the failure mode for phosphatized and anodized Al was a cohesive failure, whereas the anodized sealed Al exhibited interfacial failure. Hence, the thermodynamic work of adhesion is not useful for predicting the order of adhesive strengths of these systems because the mode of failure is not interfacial in each case.

2. Roughness Factor

Measured contact angles are sensitive to surface morphology and chemical composition and these factors may result in contact angle hysteresis (37). For example, in the case of an anodized Al substrate which results in a porous surface, the contact angle exhibits hysteresis and this porous surface was studied by Johnson and Dettre (38). The roughness ratio is given by Wenzel (37) and is written as

$$r = \cos\theta_r / \cos\theta_s \qquad [8]$$

where θ_r is the observed contact angle on a rough surface, and θ_s is the contact angle on a smooth surface. If θ_s is < 90 degrees on a smooth surface, then roughening the surface will result in θ_r being even smaller. This will increase the apparent surface free energy of the solid

TABLE 2. Surface characteristics of aluminum surfaces and elastomers (40).

Surface	γ_s^D (mJ/m²)	γ_s^P (mJ/m²)	γ_s (mJ/m²)
Phosphatized Al	150	1.6	151.6
Anodized Al	125	44	169
Anodized, sealed Al	41	15	56
SBR	29.5	0.7	30.2
NBR	26.5	9.5	36

TABLE 3. Thermodynamic work of adhesion of aluminum/elastomer systems (35).

Surface	Al/SBR W_A (mJ/m^2)	Al/NBR W_A (mJ/m^2)
Phosphatized Al	136	135
Anodized Al	194	229
Anodized, sealed Al	82	97

surface and consequently also increase the extent of wetting. However, if θ_s is > 90 degrees on a smooth surface, roughening the surface will increase the contact angle θ_r still further and therefore decrease the degree of wetting.

Hitchcock et al. (39) have reported that increasing the roughness of the substrate may only increase the degree of wetting if the liquid forms a low contact angle or if the surface is very rough. Therefore, roughness ratios can be used to empirically predict the wetting behavior of liquids on rough surfaces.

Table 4 lists the coefficients of roughness obtained for differently pretreated aluminum substrates (40).

C. Durability of Adhesive Bonds

1. Moisture Intrusion

Moisture intrusion into a bondline occurs by (i) diffusion through the adhesive, (ii) transport along the oxide-adhesive interface, a process called wicking, (iii) diffusion through the adherend, such as is the case for a composite, and (iv) capillary action through cracks and crazes in the adhesive. The last process is of special concern for bonded joints which have been aged rather than freshly prepared.

Once moisture enters the bondline, water may cause weakening by one or a combination of the following actions: (i) attacking the adhesive/adherend interface either by displacing the adhesive or by hydrating the metal or metal oxide surface of the adherend and (ii) inducing swelling stresses in the adhesive joints (41).

TABLE 4. Roughness factors (r_f) for various aluminum surfaces (12).

Solid Surface	r_f
Smooth glass plate (ref.)	1.0
Anodized Aluminum	1.47
Anodized, sealed Al	1.08
Phosphatized Al	1.01

In regard to the mode of moisture penetration, the strength loss of glass-reinforced plastic on exposure to water was described as a 'wicking' of water along the interface by capillary action from the cut ends. Indeed, if there is a gap between glass and resin at an open end, water will enter provided the glass surface is untreated and the contact angle of water against the glass is small. However, experiments with single glass filaments embedded in thin films of polyester resin showed that diffusion through the resin to the glass surface occurred (42). The diffusion coefficient of water in many materials including epoxy has been reported (43).

MacDonald (44), reported that although an epoxy adhesive absorbed 20 wt. % water at 90 °C, the tensile strength dropped only about 10 %. The same resin absorbed 70 % ethanol with a drop in strength of about 30 %. Aluminum joints formed with this adhesive dropped 50 % in strength at 20 % water absorption but ethanol had no effect on the bond strength. Since both water and ethanol lowered resin strength but only water lowered bond strength, it is clear that displacement of the adhesive from the interface occurred rather than the failure of a weakened bulk adhesive. The lowering of bond strength due to weakening of the adhesive may occur infrequently because the absorbed water will plasticize the adhesive which changes the nature of the failure from brittle to ductile, thereby changing the stress distribution and the failure mode.

Displacement of the adhesive by water is a more important mechanism where chemisorption bonds are broken

by hydrolysis or the adhesive itself hydrolyzed at or near the interface. Displacement of physically adsorbed adhesive should be a reversible process and the evidence for this process has been reported (45).

The concentration of water has been found to affect joint durability. Basically the higher the activity of the water present in the environment, then the greater is the degree of attack on the interfacial regions of the joint. Also, there often appears to be a minimum concentration of water below which no environmental failure occurs (45).

It is known that in the presence of moisture, stress is much more detrimental to an adhesive joint than either effect applied separately. Patrick et al. (46) worked with epoxy-aluminum bonds and a crack-extension technique and found that a crack initiated in the center of the resin, shifted its growth to the interface in the presence of water and proceeded at a load of only 20 % of the normal static breaking load. The failure was interfacial, a rare occurrence under dry conditions.

The explanation of the combined stress and moisture behavior can be regarded as having two direct effects. The tensile stress must weaken the resin to some extent, but it also probably increases the rate of diffusion of the moisture in the polymer adhesive by increasing the free volume.

2. Thermodynamic Considerations

The stability of a adhesive/substrate interface in moist environment may be understood from thermodynamic considerations reported by Gledhill and Kinloch (45).

Basically, in the presence of a liquid, the work of adhesion W_{A1} is given by:

$$W_{A1} = \gamma_{al} + \gamma_{sl} - \gamma_{as} \quad [9]$$

where γ_{al} and γ_{sl} are the interfacial free energies between the adhesive/liquid and substrate/liquid interfaces, respectively, γ_{as} is the interfacial free energy between the adhesive/solid, and W_{A1} in terms of dispersion and polar component using equation [6] can be expressed as

$$W_{A1} = 2[\gamma_{lv} - (\gamma_a^D \gamma_{lv}^D)^{1/2} - (\gamma_a^P \gamma_{lv}^P)^{1/2} - (\gamma_s^D \gamma_{lv}^D)^{1/2} - (\gamma_s^P \gamma_{lv}^P)^{1/2} + (\gamma_a^D \gamma_s^D)^{1/2} + (\gamma_a^P \gamma_s^P)^{1/2}] \quad [10]$$

where γ_{lv} is the surface free energy of the liquid. The work of adhesion, W_A, in a dry atmosphere was given in equation [7]. For an adhesive/substrate interface in dry air, the work of adhesion usually has a positive value, indicating thermodynamic stability of the interface. For an adhesive/substrate interface in a moist environment, the work of adhesion, W_{A1}, may have a lower positive value or a negative value indicating the interface is now unstable and will delaminate (47). Thus, calculation of W_A and W_{A1} may enable the environmental thermodynamic stability of the interface to be predicted.

The thermodynamic aspect of the separation of model adhesive assemblies in liquid media have been studied by Carre and Schultz (48). In the case of adhesive failure, the decrease of the adhesive strength can be quantitatively predicted from the surface characteristics of the solids and of the liquid. In the case of a cohesive failure, the contribution of both physical and

chemical interactions to the cohesion energy of the crosslinked elastomer have been considered and were in good agreement with those calculated using network models.

3. Kinetics of Water Entry (Diffusion)

Gledhill et al. (49) studied the durability of structural adhesive joints, employing an epoxy adhesive, and also measured the diffusion coefficient and solubility of water in the bulk epoxy adhesive under the same environmental conditions. The reported rate of interface debonding of these joints is controlled by the availability of water at the interface, which in turn is governed by diffusion of water through the adhesive. If water enters a joint by diffusion, then it is possible to calculate the distribution of water using standard diffusion equations (50).

Polymers at temperatures below Tg often exhibit non-Fickian sorption and diffusion behavior with penetrants that swell the polymer. Sorption occurring over a large concentration increment (internal sorption) results in a sigmoid curve as shown in Figure 3b. The two-stage type of sorption curve illustrated in Fig. 3c is observed in a certain concentration range when a polymer is allowed to sorb successive small increments of penetrant (internal sorption). These plots are different when compared with the Fickian-type curve normally observed for sorption with a diffusion coefficient dependent only on concentration as plotted in Fig. 3a.

With amorphous polymers, a transition from non-Fickian to Fickian behavior is often found to occur when the sorbed concentration reaches a value at which the

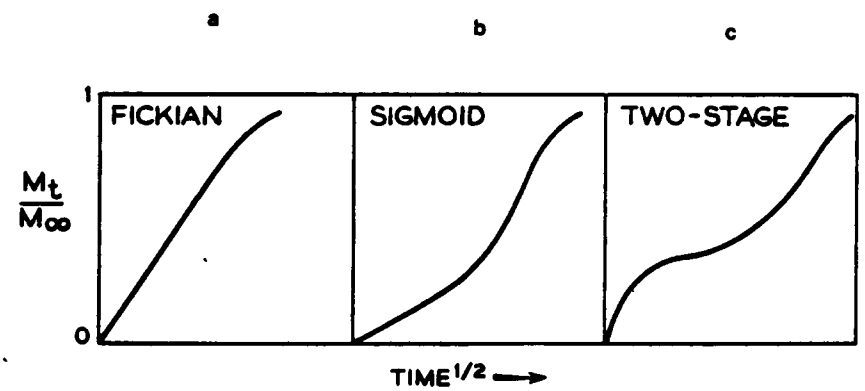

Figure 3. Ideal (Fickian) and anomalous sorption curves (63).

glass transition temperature of the mixture, Tg (mix), equals the temperature of the experiment (51).

Brewis et al. (52) examined the liquid water uptake by a series of epoxide adhesives based on diglycidyl ether of bisphenol A (DGEBA). The resulting mass uptake plot for an epoxide in liquid water at 45°C is shown in Figure 4. Linear uptake of this type is typical for Fickian diffusion in the rubbery region. Fickian and non-Fickian sorption have been compared by Fujita (53). In recent years quite a large number of uptake plots for water in adhesives or in composites have appeared in the literature (54) and frequently these plots show Fickian sorption behavior.

Nakamura et al. (55) found a quantitative relationship between wet shear strength of adhesion and moisture content. The reported diffusion coefficient of water is larger at the interface than in the bulk adhesives.

Comyn et al. (56,57), using phenolic adhesives to bond aluminum alloys, reported that the decrease in single lap strength is controlled by the rate at which water enters the adhesive layer. The effect of moisture on joint strength can be interpreted in terms of water, by virtue of its high permittivity, weakening ion-pairs at the interface.

The detailed dependencies of the diffusion and permeation parameters on the properties of the polymers are more complex than for solubility, owing to the kinetic nature of the transport process. Chemical modification of a polymer can have a pronounced effect on both diffusivity

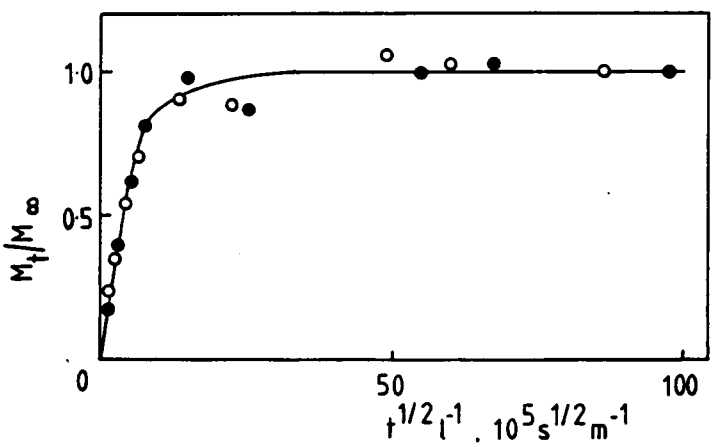

Figure 4. Uptake of liquid water at 45°C by DGEBA-DMP epoxides (52).

and permeability. The presence of double bonds in main polymer chains tends to increase the diffusion coefficient (58). The molecular weight of a polymer has been found to have little effect on the rates of diffusion and permeation (59,60). Diffusion coefficients generally decrease as the molecular weight or the volume of the penetrant molecule increases (51). Studies of the effect of crosslinking on the permeability of rubbers have shown that both the permeability and diffusion coefficients decrease with increasing degree of crosslinking (61). The rate of penetrant transport in an amorphous polymer below its glass transition temperature is markedly dependent on the degree of orientation of polymer chains and their direction relative to the direction of diffusive flow (62). The rate of penetration parallel to the orientation axis is less than the rate in a randomly oriented sample, which is in turn less than the rate perpendicular to the orientation axis (63).

D. Surface Pretreatments

During the 1970's and early 80's, the adhesion community realized that the surface plays an important role in the interaction of materials and put much emphasis on surface studies (64-68). Over the past few years, new techniques have been used for surface studies, surface analysis instrumentation has improved and the pretreated surfaces can now be characterized at a sub-microscopic level (< 10 nm) (69,70).

The purpose of the surface pretreatment can be considered threefold. First, to remove or prevent the

formation of any weak surface boundary layer on the substrate. If any weak layer is initially on the substrate and is not removed, then the locus of joint failure is likely to be through this region and a relatively low joint strength will be observed. Weak boundary layers include machine oils, weak oxide scale and low molecular weight species. Secondly, to maximize the degree of intimate molecular contact that is obtained between the adhesive and the substrate during the bonding process. Finally, to generate a specific surface topography on the substrate. This last purpose is important when mechanical interlocking is a major mechanism of intrinsic adhesion.

There are many pretreatments which result in a porous surface oxide or microroughness of aluminum surfaces (71-75). Studies have indicated that when the surfaces have a porous oxide or microroughness, strong bonded joints result due to the mechanical interlocking of the adhesive with the pretreated surfaces (18,76-78).

Anodization is one method of generating a porous oxide layer on a metal surface. The process of anodization produces a coating of metal oxide on a metal anode by the electrochemical oxidation (applied potential) of that anode in contact with an electrolyte. Anodization has been utilized in metal-to-metal adhesive bonding since the early 1960's. At that time sulfuric and chromic acid were the primary electrolytes (79,80). Chromic acid has been used in Europe for adhesive bonding during the past fifteen years (81). In the early 1970's, the Boeing Aircraft Company developed a process using phosphoric acid

as the electrolyte and this process became the surface preparation method of choice for adhesive bonding in the United States (82).

1. The Formation and Growth of Aluminum Oxide

The early studies of electrokinetics by Guntherschulze and Betz (83) in the 1930's indicated that the ionic current density (I) corresponding to the thickening of oxide films is roughly an exponential function of the field strength (H) as shown by the equation

$$I = A \exp (BH) \qquad [11]$$

where A and B are constants, and H is the potential drop across the oxide film divided by the film thickness. The form of equation [11] suggests that the field strength (H) changes the energy barrier of the rate-determining step for ionic current transport, as the ions migrate through the anodic film. In other words, the field lowers the activation energy of the rate limiting step in the growth of the oxide. The formation and growth of the anodic oxide have been explained in terms of field-assisted dissolution mechanisms (84).

According to field-assisted dissolution theory, pore initiation occurs at points in the barrier layer which are somewhat thinner, and where the current density is relatively high. The non-porous barrier layer is produced first in the anodization process. Pore initiation always occurs after the anodization current density drops to a value close to the steady-state current density, or after the barrier layer has grown to a steady-state thickness. Once the steady state structure is reached, oxide growth

continues by two simultaneous processes: (i) migration of Al^{3+}, and OH^- ions through the existing barrier layer to form new oxide at the interface with the underlying metal; and (ii) oxide dissolution at the bases of the pores due to the higher current density in these regions, i.e. field-assisted dissolution. The applied voltage and the electrolyte characteristics are the two key factors which determine the structure of the anodic layer on a metal substrate. The voltage assisted oxide dissolution characteristics of the electrolyte determines the thickness of the barrier layer that can be maintained for a particular voltage and so determines the related pore diameter and cell-wall thickness (85).

The formation and properties of oxide films formed on pure aluminum have been reviewed extensively in the literature by a number of authors (86-90). Harrington and Nelson (91) reported that the composition of anodic oxide films formed on aluminum in different electrolytes are mostly amorphous compounds. An excellent review of the oxides and hydroxides formed on aluminum has been published by Wefers (92) and is concerned mainly with crystalline oxide compounds.

E. Conformation of Polymer Chains

Since polysulfone either as a melt or in solution as a primer will be used in the present experiments, a brief review of the theory on the conformational properties of both ideal and real polymer chains is appropriate.

Those arrangements of the polymer chain differing by reason of rotations about single bonds are termed

conformations. In solution, a polymer molecule is a randomly coiled mass most of whose conformations occupy many times the volume of its segments alone. The size of the molecular coil is very much influenced by polymer-solvent interaction forces.

The size of the random coil can be expressed in terms of statistical parameters such as the root-mean-square distance between its ends, $(r^2)^{1/2}$, or its radius of gyration, the root-mean-square distance of the elements of the chain from its center of gravity, $(r_g^2)^{1/2}$. For linear polymers that are not appreciably extended beyond their most probable shape, the mean-square end-to-end distance and the square of the radius of gyration are simply related as $r^2 = 6\ r_g^2$. For extended chains $r^2 > 6\ r_g^2$. The use of the radius of gyration is sometimes preferred since it can be determined experimentally (93).

A simple model of a polymer chain consists of a series of n links of length l joined in a linear sequence with no restrictions on the angles between successive bonds. The probability that such an array has a given end-to-end distance r can be calculated by the classical random-flight method (94).

The distribution of end-to-end distances over the space coordinates (x,y,z) is given by the Gaussian distribution function. Therefore, if one end of the chain is taken at the origin, the probability of finding the other end in a unit volume near the origin is highest. This probability decreases continuously with increasing distance from the origin. On the other hand, the probability of finding a chain end within the volume of a

spherical shell between distances r and r+dr from the origin has a maximum.

The most important result of the calculation is that the end-to-end distance is proportional to the square root of the number of links:

$$(r^2)^{1/2} = l*n^{1/2} \qquad [12]$$

The random-flight model however seriously underestimates the true dimensions of real polymer molecules for two reasons. First, restrictions to completely free rotation, such as fixed valence angles, the correct weights for trans and gauche conformations, statistical deviations from ideal trans and gauche states, and other short-range interactions lead to larger dimensions than calculated above. Secondly, long-range interactions resulting from the inability of chain atoms far removed from one another to occupy the same space at the same time result in a similar effect.

1. Short Range Interactions

Flory (95) has calculated the effect of short range interactions on the dimensions of random-coil polymers. Several effects are involved. The restriction to fixed bond angle expands the chain by a factor of $[(1-\cos\theta)/(1+\cos\theta)]^{1/2}$, equal to 1.41 for carbon-carbon bonds. Restricted rotation, whether resulting from steric hindrances and resulting potential-energy barriers or from resonance leading to rigid planar conformations, increases dimensions still more.

The net results of these short-range interactions can be expressed as a characteristic ratio of the square of the actual chain dimensions in the absence of long-range

interactions (called the unperturbed dimensions and given the symbol r_o^2) and the square of the random-flight end-to-end distance, $n*l^2$.

2. Long Range Interactions and the Excluded Volume

Correction of polymer chain dimensions for short-range interactions still fails to eliminate conformations in which two widely separated chain segments occupy the same space. Each segment of a real chain exists within a volume from which all other segments are excluded. A statistical approach has allowed the calculation of the excluded volume and this leads to the result that the mean-square end-to-end distance is proportional to $n^{0.6}$ (96).

The effect of the long-range interactions on polymer chain dimensions is to cause a further expansion of the chain over its unperturbed dimensions, since more of the compact conformations, with small values of r^2, must be excluded. The actual dimensions of the real chain can be expected to exceed its unperturbed dimensions by an expansion factor α. Thus,

$$(r^2)^{1/2} = \alpha(r_o^2)^{1/2}. \qquad [13]$$

The values of α depends on the nature of the solvent. A solvent for which α is large is said to be a thermodynamically "good" solvent, where polymer-solvent contacts are highly favored, and the coils are relatively extended. If α is small, then it is a "poor" solvent and the coils are relatively contracted. Neutron-scattering experiments show that the above considerations apply to chain conformations in the melt and the glassy state as

well as in solution (97).

In regard to adhesion, Schultz and coworkers (98) have shown that the polar moiety in graft copolymers of ethylene and acrylic acid, can orient either into the bulk or into the interface, depending on the contacting medium. Expectedly, the bond strength of metal joints using the polymer in these distinct conformations as the adhesive differs greatly. Bogue et al. (99) reported a twofold difference in the peel strength of Al-styrene-butyl acrylate copolymers depending on the adhesive chain conformation.

F. Polymer-Metal Interface

There has been extensive research done to understand polymer-metal interactions (100-104). However, in addition to the usual problems of sensitivity and observability of a buried interface, polymer interfaces bring additional issues of surface and interface preparation, limited thermal stability of the materials, and structural disorder. All these factors represent significant obstacles to polymer-metal interface research (105-107). It is often the case that for a given polymer system, the structure and property of the bulk is substantially different from that of the surface (105,106,108-111). For instance, by melting polyethylene onto a high-energy aluminum surface, Schonhorn and Ryan (111) have shown evidence for extensive nucleation and the formation of a transcrystalline region in the polymer as illustrated in Figure 5 in which the depth of transcrystalline region is estimated to be about 25 μm.

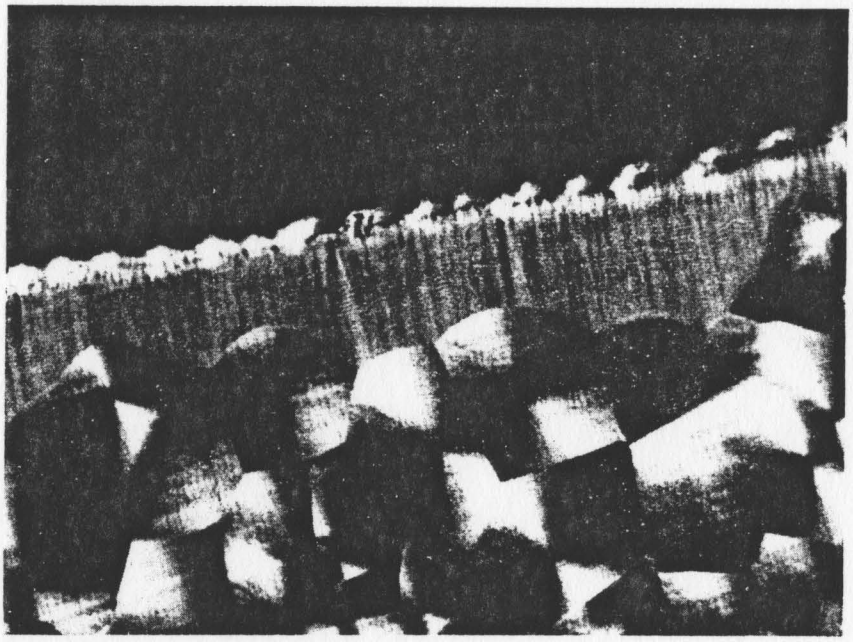

Figure 5. Transcrystalline region generated at the solid-liquid interface after cooling (111).

They also concluded that the occurrence of the normal weak boundary layer is a consequence of the morphology of the surface region of the polymer in contact with the aluminum material. Hahn (105) using a highly sensitive electrical resistance technique simultaneously measured the residual stresses developed in the interfacial bond and in the bulk regions of an epoxy adhesive during cure. Significant differences in residual stress between interfacial and bulk adhesive zones were demonstrated in an epoxy-aluminum system. Knollman (106) has shown by acoustic testing methods, that there is a linear variation in the shear modulus near the adhesive/adherend interface. The shear modulus of a common industrial adhesive decreases with increasing adhesive thickness when bonded to aluminum.

A technique which is capable, therefore, of monitoring differences in both structure and properties between the surface and the bulk of the polymer is obviously of considerable relevance in many fields of academic and technical importance.

The conventional method of analyzing polymer coatings is the infrared internal reflection method or ATR (Attenuated Total Reflectance) (112-115). With this technique, one can study coatings that are approximately one micron thick. The analysis depth is dependent on a number of factors including sample to crystal contact, refractive index, and wavelength. Using transmission and reflection infrared spectroscopy, Luongo and Schonhorn (115) found that the degree of crystallinity in the surface region was dependent on the nature of the substrate. That is, relatively small and randomly

oriented spherulites were observed in the surface region of thin polyethylene film nucleated on gold, a high energy surface. The surface region of a thin polyethylene film nucleated on polytetrafluoroethylene, a low energy substrate, was observed to contain considerably fewer spherulites. However, the spherulites were much larger in size, with orientation restricted, in general, to the plane of the film. For coatings on a polished mirror surface, this IR method is a useful technique. But where the deposited film is on a pretreated surface which is not a mirror finish surface, IR is often incapable of detecting such thin layers.

XPS (X-ray Photoelectron Spectroscopy) can reveal information on such thin layers. In the past few years, a number of studies have been reported using XPS to investigate the metal-polymer interface (116-119). Ho et al. (118) reported XPS evidence for a chemical reaction between aluminum and polyimide. This was particularly clear for an interface formed at elevated temperatures as shown by the core level spectra in Figure 6 obtained in a series of evaporation of aluminum on polyimide at 300 C.

Polymeric materials generally exhibit various molecular motions and relaxations. Such relaxation processes, which include the glass transition temperature, have significant effects on physical and mechanical behavior. Polymer molecules and segments at surfaces and interfaces also exhibit motions and relaxations. In air, such motions permit the surface to restructure to minimize the surface free energy.

The glass transition temperature, Tg, is a thermal

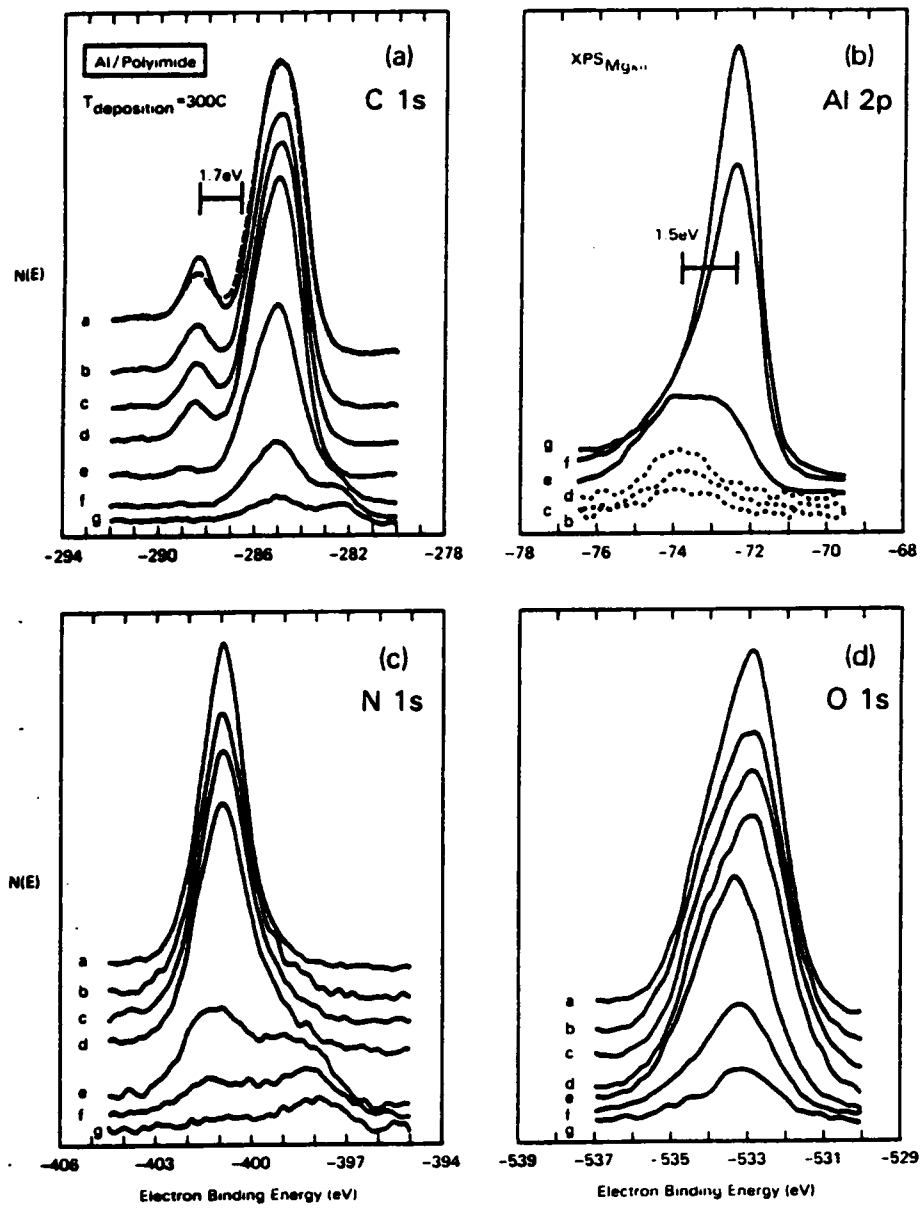

Figure 6. XPS spectra of (a) C 1s, (b) Al 2p, (c) N 1s, and (d) O 1s measured during in situ formation of the Al-polyimide interface as a function of Al coverage (118).

property that shows itself in the viscoelastic region and is important in determining the mechanical properties of polymers, mainly because of its relationship to the time-temperature equivalence of viscoelasticity. The glass transition itself can be determined from a change in the volume coefficient of expansion. That is, in the glassy state, large-scale molecular motions do not take place but atoms and small groups of atoms move against the local restraints of secondary bond forces. The glass transition corresponds to the onset of liquid-like motion of much longer segments of molecules, characteristic of the rubbery state. This motion requires more free volume than the short-range motions of atoms in the glassy state. The rise in the relative free volume with increasing temperature above Tg leads to the higher observed volume expansion coefficient in this region. Since the fully extended chain is the conformation of minimum energy, it tends to be assumed more frequently as the temperature is lowered. As the molecules extend out, the free volume decreases. In turn, flow becomes more difficult.

The fraction f of free volume may be defined as

$$f = f_g + (T-Tg)\ a \qquad T > Tg$$

$$f = f_g \qquad T < Tg \qquad [14]$$

The volume expansion coefficient a is that resulting from the increase in amplitude of molecular vibrations with temperature. The f_g is the fractional free volume at Tg. New free volume is created above Tg as the result of an increase a in the expansion coefficient. The f is constant for all temperatures below Tg.

Williams, Landel, and Ferry (120) reported that the

logarithm of viscosity (η) varies linearly with 1/f above Tg, so that

$$\log (\eta/ \eta_g) = 1/f - 1/f_g \qquad [15]$$

where η_g is the viscosity of the polymer at Tg. Substituting equation [14] into [15] leads to

$$\log (\eta/ \eta_g) = - a(T-Tg)/(b+T-Tg) \qquad [16]$$

which is the well known WLF equation. The constants a, and b can be determined by fitting literature data on the viscosity-temperature behavior of many glass-forming substances. The shift factor a_T is the ratio of the viscosity at T relative to that at Tg. The viscosity at T_g is about 10^{13} poise for many substances.

Equation [16] indicates that both the viscosity of the polymer and the activation energy (Δ Ea) for viscous flow

$$\Delta Ea = 2.3\ R\ d(\log \eta)/d(1/T) \qquad [17]$$

should become infinite at T = Tg-b = Tg-51.6. Thus by extrapolating downward from behavior well above Tg, one would predict that all molecular motion should become completely frozen at T < (Tg-51.6). What happens is that new mechanisms of deformation take over more or less sharply as Tg is approached (121,122). This method thus provisionally identifies a transition. If the experiment contains the additional dimension of frequency, such as in dynamic mechanical analysis (DMA), not only can the glass transition temperature be determined from the ratio (tan δ) of energy loss to energy gain, but the entire transition from the glassy through the viscoelastic to the rubbery state also can be derived within the time scale of a single experiment. Such an experiment, when carried out

under constant sample load, enables characterization of the time scale of viscoelastic behavior at short times for most polymers (123). It is then possible to obtain a molecular interpretation of certain properties of the polymer (124).

Dynamic mechanical tests have been used to study the viscoelastic response of the filled polymers. Droste and DeBenedetto (125) using thermo mechanical methods on epoxy filled with either glass beads or clay found that the Tg of the polymer increased with increasing filler concentration and with increasing specific surface area of the filler. The data were interpreted by assuming that interactions between filler particles and the polymer matrix reduce molecular mobility and flexibility of the polymer chains in the vicinity of the interfaces. Price et al. (126) studied a styrene cured polyester filled with potassium perchlorate powder 200 μm in diameter using NMR and thermo mechanical analysis. A range of Tg was found depending on the proportions of $KClO_4$ present. The results were attributed to the presence of two phases; one arising from the constrained polymer segments and the other to the neat polymer. It is interesting to note that the Tg changes occurred despite the 200 μm (small surface area) particle size of the filled system. Iisaki and Shibayama (127) using dynamic mechanical analysis and broad line NMR methods found a Tg shift to higher temperature with increasing filler volume fraction V_f (Fig. 7). The results were attributed to the filler which immobilizes the chain segments and causes a different distribution of local mobility around the junction point.

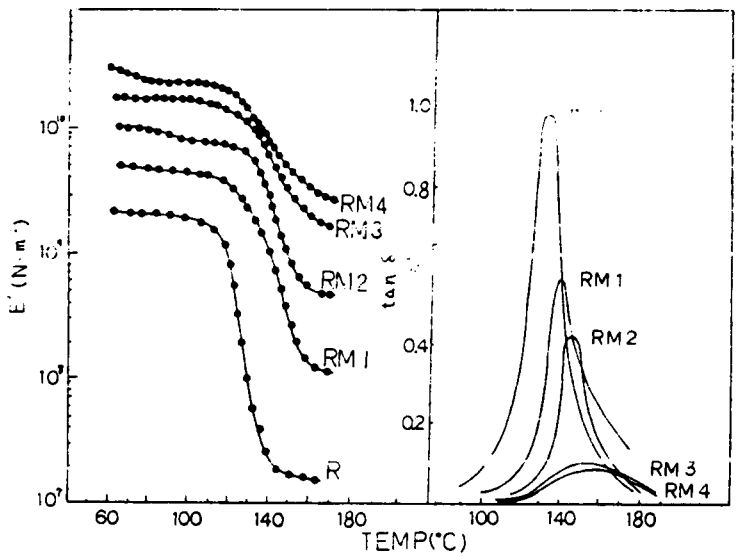

Composition

Sample	Composition, vol-%	
	Resin	Mica
R	100	0
RM1	93.8	6.2
RM2	83.6	16.4
RM3	71.4	28.6
RM4	51.1	48.9

Figure 7. Temperature dependence of storage modulus E' and tan δ (127).

In adhesive bond joints, Crowley and Jonath (128), using Rayleigh scattering and thermally induced dielectric relaxation techniques on aluminum joints bonded with an epoxy adhesive, reported restricted polymer mobility ranging as much as 10 μm from the aluminum surface. Lipatov and Sergeeva (129) studied the effective cross-linked density by swelling measurements of polyurethane coatings based on polyethers and polyesters in the free film and on an aluminum surface. They reported that cross-link densities differed depending upon whether the free film or the surface film was measured. The latter had the lower molecular weight between cross-links. They considered that the chemical reaction was different in each case due to the presence or absence of an interface.

These examples using various techniques point to a general phenomenon in which there is restricted polymer segment mobility within the volume of polymer in the interphase region.

In summary, adhesives are increasingly being used in many applications and in order to understand the adhesion phenomenon, one has to study not only the surface of the substrates but the interfacial contact of a polymer adhesive to the substrate. In terms of bond durability, the mode of moisture intrusion and the influence of moisture at the interface has to be considered. Finally, physical and/or chemical changes and material properties of the adhesive in the interphase region are important in adhesion.

CHAPTER III

CHARACTERIZATION OF SURFACE PRETREATMENTS ON Al/Li ALLOY AND RELATED MECHANICAL PROPERTIES OF POLYSULFONE ADHESIVE BONDS

In order to characterize the interaction of the Al/Li oxide layer with the thermoplastic adhesive, polysulfone, single lap shear and the wedge crack opening tests were utilized following Forest Products Laboratory (FPL) etch, sulfuric acid anodization (SAA) and phosphoric acid anodization (PAA) pretreatments. Phosphoric acid anodization produces an oxide film on aluminum that is both rougher and considerably thicker (200-400 nm) than that produced by the FPL etch process. The investigation of the pretreated Al/Li surfaces involved the determination of the elemental composition and morphological features of the base oxide before and after exposure to a hot-humid environment, and of the failure surfaces.

This chapter will first outline sample pretreatments, preparation of the samples, and subsequently the surface analyses utilizing spectroscopic and microscopic techniques. Also related studies such as dynamic loading, use of primers, and infrared spectroscopy studies will be discussed.

EXPERIMENTAL

A. Surface Pretreatments

Prior to adhesive bonding of the Al/Li alloy, the samples were pretreated by FPL etching, SAA, and PAA as described in Appendix A. The priming/bonding procedures are given in appendices B and C.

B. Specimen Preparation

1. Lap Shear Test

The lap shear panels were assembled in a jig with a 1.27 cm overlap. The lap shear sample bondline thickness was controlled with a 0.1 mm wire spacer. The platen press was heated to 290°C. The jig with a 0.25 mm thick polysulfone film was then placed in the press and left 3 minutes until temperature reached 290°C, then pressed at 172.3 MPa (25,000 psi) for 10 minutes. The excess polysulfone squeezed from the bond was removed before testing. The bonded joint was placed in the Instron static mechanical tester and the resulting lap shear strength was measured (130). The results represent an average from five samples.

2. Wedge Test

A wedge was driven carefully with an Instron into the joint for a fixed distance and the position of the crack tip was marked. The bonded joint was placed in 71°C and 100 % R.H. environment from which it was removed periodically for the measurement of the crack tip advance (131,132). The crack growth results represent an average of at least three samples. After about 140 hours of

exposure, the joint was taken out and the bond pulled apart completely. Areas of the strips where environmental crack growth had occurred were then cut out for subsequent analysis.

C. Characterization of Adherend and Failure Surfaces

1. Scanning Electron Microscopy (SEM)

SEM was done using a JEOL JFM 35 C electron microscope. Pretreated samples were punched as 1.0 cm disks and sputter coated with gold using a SPI Gold Sputter. This procedure results in a coating of about 10 nm. The samples were photographed from 600 to 2400 times magnification.

2. High Resolution SEM (HSEM)

With HSEM, instead of using a simple acceleration of the secondary electrons to the detector as in SEM, the secondary electrons in the HSEM travel a torical path through the lenses to the secondary electron detector, thus resulting in higher magnifications. Figure 8 (133) illustrates the difference between the SEM and HSEM.

HSEM pictures were obtained on a Philips EM-420T electron microscope. Thin Al/Li samples were used and coated with Pd-Pt about 2 nm thick. Properly deposited, this layer does not alter the morphology within the resolution of the microscope. The magnification ranged from 6400 to 50,000 times.

3. X-ray Photoelectron Spectroscopy (XPS)

In XPS, the sample is bombarded with x-rays of known energy, hv. As the x-rays are absorbed, electrons in the sample with binding energies (E_b) less than the x-ray

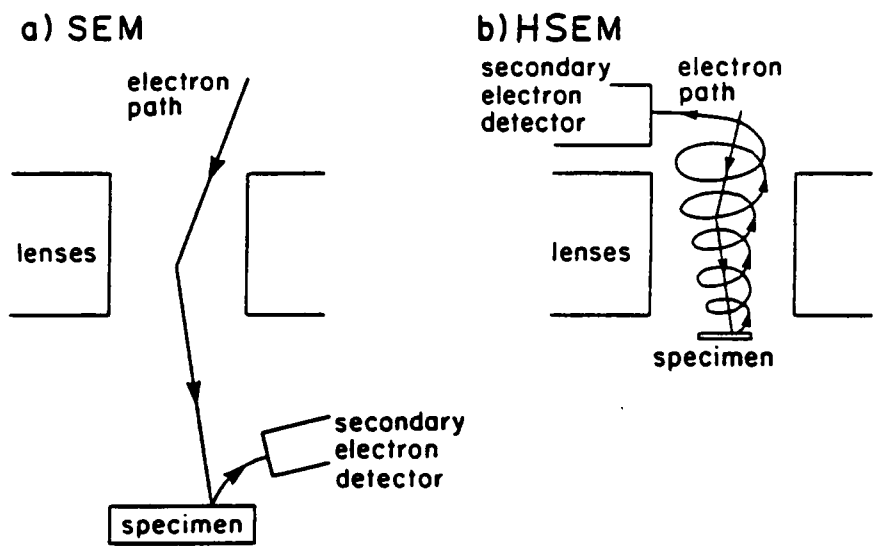

Figure 8. Secondary electron detection system for a) SEM and b) HSEM (133).

energy are excited to unoccupied states, and move within the sample. The creation of a hole after photoionization is followed by one of several processes shown in Figure 9. As these excited electrons move through the sample, they are scattered by and lose energy to other electrons. Those electrons which are photo-excited close enough to the surface escape without energy loss, and have kinetic energies, E_k. This photoejection process is summarized in equation [18]

$$E_b = h\nu - E_k + \phi \qquad [18]$$

where ϕ is the work function of the spectrometer. In XPS, Mg (1254 eV) or Al (1486 eV) x-ray targets are commonly used, hence, the outgoing electron is typically a core-level electron with a binding energy of between 0 and 1486 eV. The typical inelastic mean free path for electrons in this energy range is 5 nm (134).

a. Qualitative Analysis - XPS provides a quick, convenient, and non-destructive means of detecting the elements present on a sample. It can be seen from equation [18], that by analyzing the kinetic energy of the photoelectrons from a sample, one can obtain the binding energies and thus identify the elements present on a surface.

b. Chemical Shift - The most useful aspect of XPS lies in its ability to measure the binding energy and thereby determine the chemistry of the materials being investigated. It is possible, for example, to distinguish a metal from its oxides because the spectra will show shifts in binding energy that reflect the change in the atomic environment (135). For polymeric materials, Thomas

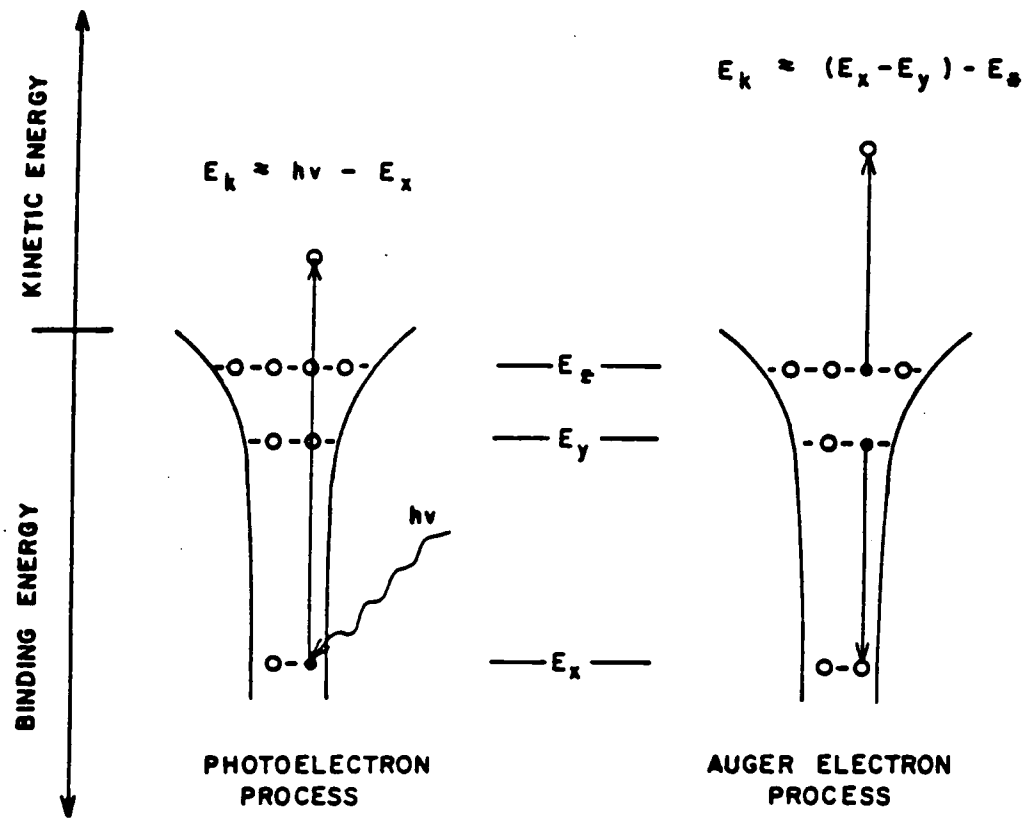

Figure 9. Schematic representation of the processes involved in x-ray photoelectron and Auger electron excitation processes (138).

(136) and Clark (137) have extensively studied the correlation of photopeak position to structure.

c. Quantitative Analysis - It is possible to determine the relative abundance of the constituents present on a surface to an accuracy of 10-20 % using only theoretical values for the photoelectron cross sections involved. With empirical standards this accuracy can be improved to better than 5 % in many cases.

Quantitative analysis is obtained from the areas under the major peak of each element. The number of photoelectrons N(E) emitted from a given core level and measured by an analyzer with a resolution dE is expressed by:

$$N(E)dE = \sigma T(E) \quad I_{h\nu} \quad (z) n(z) e^{-z/\lambda} \; dz dE \qquad [19]$$

where σ is the photoionization cross-section for a given core level of a given element, T(E) is the transmission of the electron energy analyzer, $I_{h\nu}$ (z) is the photon flux at a depth z in the sample, n(z) is the atomic density at depth z of the element of interest, and λ is the mean free path of the photoelectrons in the solid. Equation [19] can be simplified by noting that $I_{h\nu}$ (z) is constant over the depth from which electrons are measured and can be factored from the integral. If the sample composition is assumed uniform over the sampling depth, the equation can be integrated to obtain:

$$N(E)dE = \sigma T(E) I_{h\nu} \lambda \; n dE \qquad [20]$$

The quantities σ, T(E) and λ are constant for a given photoelectron line and a given analyzer (possible variations of λ with different materials are usually ignored) and can be combined into a sensitivity factor, S,

that can be calculated or measured using standards. The sensitivity factors (Si) for each element detected were the same as reported by Wagner (139). The photoionization cross-sections for a given core level of a given element are tabulated by Scofield (140). The atomic fraction of element i detected (AF_i) was determined by the following equation:

$$AF_i = (N(E_i)/S_i)/(\sum_i (N(E_i)/S_i)) \quad [21]$$

where N(Ei) is taken as the area of the given photopeak.

d. Ion Sputtering - XPS is often combined with ion sputtering, and the chemical information is then followed as a function of depth, yielding a chemical depth profile. For example, the change in an element from oxide to metal near an interface can be studied by examining the changes in peak shape and position at a series of depths as the interface is approached. Chemical depth profiles are very useful in the investigation of multi-layered structures (141).

The XPS studies were done using a Physical Electronics ESCA 5300 electron spectrometer with a magnesium anode (1.254 KeV). All samples were punched as 1.0 cm disks and scanned from 0 to 1100 eV. Major photopeaks were scanned repetitively to obtain the atomic fraction of elements on the sample surface.

4. Auger Electron Spectroscopy (AES)

In AES, the sample is bombarded by a focussed, monochromatic beam of electrons with an energy from 2 to 20 keV. The beam excites electrons near the surface. What is of interest in AES are those electrons produced by the Auger process in the excited atoms (see Fig. 9).

If an electron from a higher lying state, y, with binding energy Ey drops into the core vacancy, energy is available and equal to Ex-Ey. This energy can be emitted as a characteristic x-ray or transferred to another electron in the atom with binding energy Ez. If this latter event occurs, an excited electron (or Auger electron) is produced with a kinetic energy, Exyz,

$$Exyz = (Ex-Ey) - Ez \qquad [22]$$

It is noted that the Auger energy expressed by equation [22] is a function only of atomic energy levels, so that for each element in the periodic table there is an unique set of Auger energies, there being no two elements with the same set of atomic binding energies. Thus analysis of Auger energies leads to elemental identification (142).

a. Depth Profiling - By combining AES with inert gas ion sputtering, one can measure the elemental composition of the surface as material is milled away to expose underlying atomic layers. This procedure is especially useful for obtaining the thicknesses of thin overlayers. The sputtering rate for removal of material must be calibrated for each spectrometer for one standard material. The relative sputter yields for different materials are available in order to convert the sputtering rate of the standard to those of other samples (143). It is difficult, however, to obtain good values of sputtering rates for many materials, but if one is only interested in the differences in the thickness of overlayers, absolute sputtering rates are not needed.

It is noted that the sputter time is proportional to the amount of material removed, not to the actual

thickness as measured in an electron microscope. Thus, for example, if the sputtering rate is calibrated for a dense oxide, the apparent thickness obtained from the Auger depth profiles of a porous oxide will be less than the actual thickness. The difference between the two measurements will be an indication of the degree of porosity of the oxide (144).

The AES depth profile studies were done using a Perkin-Elmer PHI 610 electron spectrometer. Narrow scan surveys from 300 to 600 eV were performed on each sample. Samples were depth profiled by argon ion sputtering with a 4 kV ion beam, a 25 ma emission current and a 5.0 μa ion beam current with current density of 6.37 $\mu a/cm^2$. These conditions correspond to a sputtering rate of 50 nm/min for Ta_2O_5.

5. Energy Dispersive X-ray (EDX) Analysis

The EDX attachment tremendously enhances the analytical value of the SEM in material characterization by providing chemical analysis of the sample along with surface topography. Characteristic x-rays emitted under the effect of the electron beam provide information about the nature and amount of elements present in the volume excited by the primary beam. The EDX spectrum was obtained using a Tracor Northern TM 5500 analyzer which is attached to the Philips EM-420T scanning transmission electron microscope.

6. X-ray Diffraction

X-ray diffraction is induced by periodic fluctuations in electron density that occur over small distances (up to 2 nm). X-ray diffraction from crystals can be used to

determine the degree of crystallinity and obtain information regarding size, perfection and orientation of the crystals. Detailed reviews of x-ray scattering and its application can be found elsewhere (145,146).

A Diano 8300 x-ray generator equipped with an LSI-II computer was utilized for this study. The general operating conditions for the x-ray generator were 40 kV and a 20 mA beam current using CuKα anode. X-ray exposure time was approximately 30 minutes. A PAA Al/Li sample was exposed to a 71 $^{\circ}$C and 100 % R.H. environment for 100 hours. Samples before and after environmental exposure were analyzed.

D. Preferential Dissolution of Al/Li Alloy and the Oxide

This method uses a 5 wt % NaOH solution which dissolves the Al/Li alloy and its surface oxide readily, whereas it does not solvate the polysulfone used as an adhesive in this study. A neat polysulfone film placed in a 5 wt % NaOH solution showed no signs of dissolution when examined by SEM. The Li/Al and its oxide could thus be preferentially removed and HSEM photomicrographs were taken of the remaining polysulfone solid phase.

E. TEM of Ultramicrotome Sections.

Ultramicrotomy was used to produce thin sections of surface films on aluminum after different pretreatments and these cross sections have been examined by transmission electron microscopy (147). Cross sections of films produced by thermally pressing PSF onto PAA Al/Li surfaces were also prepared. After thin strips (2mm x 5

mm x 0.3 mm) were cut from the specimens, each strip was mounted in an embedding mold. The encapsulating resin formulations according to Luft (148) using the higher ratios of Mix A to Mix B gave the best cutting properties. Mix A consists of 31 ml Epon 812 resin and 50 ml of DDSA (dodecenyl succinic anhydride), while Mix B contains 25 ml of Epon 812 and 22 ml of NMA (nadic methylanhydride). A small quantity (0.15 ml) of the accelerator DMP-30 (dimethyl aminomethylphenol) was added for every 10 ml of the above mix prior to curing. Curing was carried out at 60 C for 48 hours.

A 2.5-2.9 mm diamond knife (E.I. DuPont deNemours) in a Reichert-Jung Ultracut-E microtome was used to obtain thin sections of the aluminum substrate and its attached PSF film. Before sectioning, the top of the specimen was trimmed with a razor blade to form a truncated pyramid in order to present a minimal thickness of aluminum and its embedding epoxy to the microtome knife. The sections were produced using a clearance angle of 4°and the cutting temperature was 23°C. The cutting speed and sectioning thickness were set at 0.5 mm/sec and 50 nm respectively. The sections were allowed to float on a pool of distilled water which is contained by the knife assembly. Sections were collected from the knife water bath on 400 mesh copper grids, dried and examined using a Philips EM-420T transmission electron microscope.

F. Polishing of Al/Li Samples

A small square (2.54 x 2.54 cm) of an Al/Li sample was polished on a grinding wheel first starting with a

fine sand paper wheel then using a finer sand paper wheel, and finally finishing with a fine cloth wheel with a 5 um polishing compound. This polishing procedure resulted in a mirror-like finish on which the polysulfone film was spin cast.

G. Spin Cast Films

In spin casting a thin polymer film, Al/Li polished samples were secured to a custom made spinning platform shown in Fig. 10 by means of double stick tape. The polished Al/Li substrates were flooded with a polymer solution of known concentration and spun at an average speed of 1500-1600 rpm for five seconds. The resulting film thickness for a 0.125 wt % solution of polysulfone in chloroform was found to be approximately 7-12 nm by ellipsometry. The ellipsometer used was a Gaertner L 116A.

H. Infrared Spectroscopy Studies

One of the mechanisms of adhesion is that of chemical bond formation. It is possible to evaluate surface chemical reactions occurring at an adhesive-oxide interface by infrared spectroscopy.

Infrared spectroscopy involves a determination of the electromagnetic radiation absorbed by a compound as a function of the wavelength of radiation transmitted through the entire sample thickness.

There are mainly three techniques for obtaining IR spectra of surfaces. The first is the attenuated total reflectance (ATR) technique, but this technique cannot be

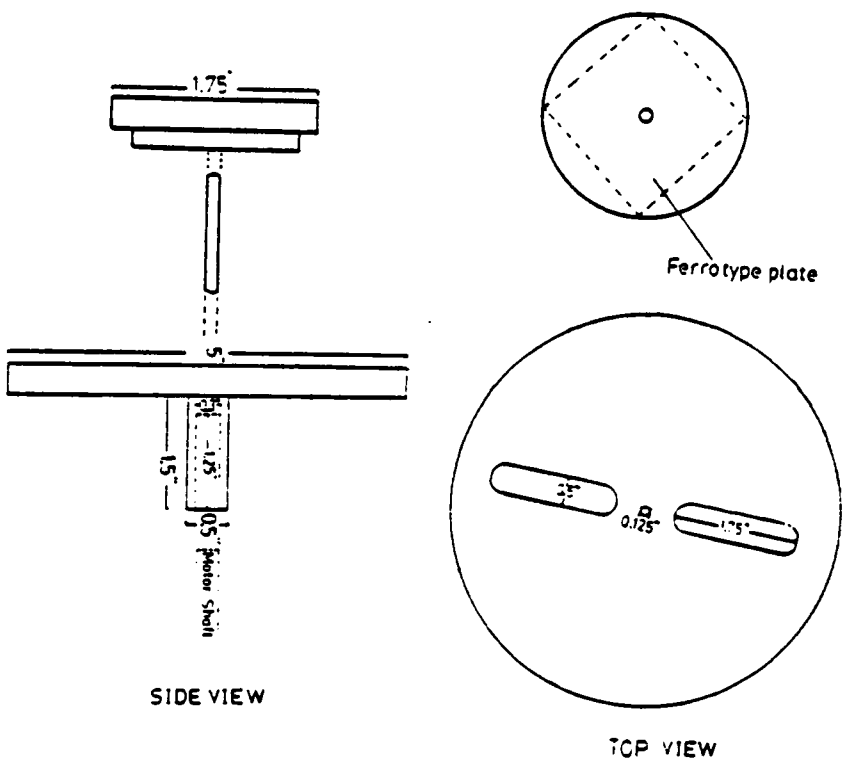

Figure 10. Schematic diagram of spin coating platform.

used on rigid, uneven surfaces since good contact between the ATR crystal and the surface cannot be obtained without using a contact liquid. The second technique obtains information when the infrared beam strikes a reflective sample surface at near-grazing incidence. At normal incidence, phase changes occur upon reflection that minimize the electric field (and any infrared absorption) at the surface. At grazing incidence, the effect of phase changes is lessened and a stronger electric field exists at the surface, enabling infrared absorption to occur. Spectra have been collected from films less than 10 nm thick on polished aluminum substrates (149,150), and on polymer substrates (151,152). The net electric field of the radiation at the surface is perpendicularly oriented to the surface. The dipole moments of the adsorbed molecules must have a perpendicular component to absorb incident radiation. Thus, grazing angle experiments can yield information about the orientation of molecules on an aluminum surface (153). The third technique is diffuse reflection (DRIFT), and it uses externally reflected light which is scattered by the sample, collimated and detected. This technique does not require a mirror finish surface and thus the technique is very useful for polymer-aluminum interaction studies (154,155).

1. Grazing Incidence Angle

Grazing angle reflectance FTIR (156) was used to study thin PSF coating on reflective ferrotype plates and polished Al/Li surfaces. The grazing angle reflectance experiment was carried out in a Nicolet 5DX spectrometer. The sample chamber was purged with nitrogen for 30 to 60

min before a spectrum from 4600 to 400 cm^{-1} was obtained.

2. Diffuse Reflectance Infrared Fourier Transform (DRIFT)

The DRIFT technique was used for all nonreflective surfaces. The background for the PAA bare surface was obtained with KBr powders. The instrument used was a Nicolet 5DX spectrophotometer with a Barnes diffuse reflectance accessory. All spectra were measured with a resolution of 2 cm^{-1} and scanned 200X.

I. Comparison of Mode I and Mode II Failures

Bonded wedge samples were placed in an Instron tensile test machine and failed in mode I (crack opening mode). The rate of Instron head movement was 2.12×10^{-2} mm/sec (0.05 in/sec) which is the same rate as used in the single lap shear test.

J. Cyclic Loaded Double Cantilever Beam Samples

The specimen used in 71°C and 100 % R.H. environment was the thick adherend double cantilever beam (DCB) specimen. The configuration of the test specimen is shown in Figure 11. Cyclic loading was conducted by first precracking each specimen to a displacement of 2.54 cm using an MTS machine. Specimens were cyclic loaded by a pin and clevis arrangement that was exposed to the 71° C and 100 % R.H. environment. The load cycle was 1 cpm. The load profile was sinusoidal for each cycle. Crack growth versus the number of cycles was recorded. The cyclic load test results represent measurement of two samples. Areas of the strips where cyclic and

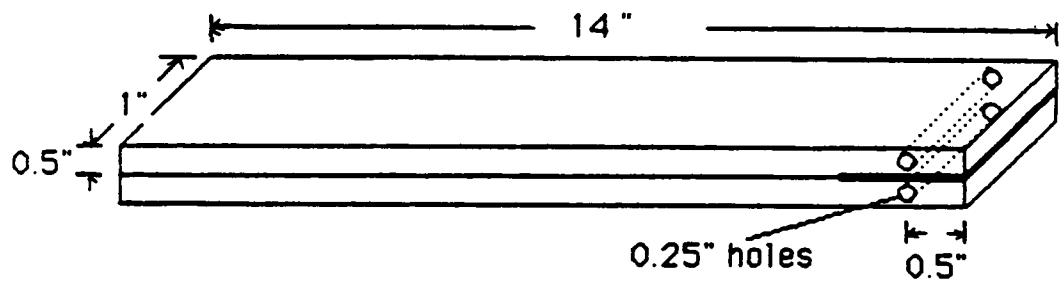

Figure 11. Thick adherend DCB specimens used for cyclic load durability test (196).

environmental crack growth had occurred were then cut out for subsequent analysis.

MATERIALS

A. Al/Li Alloy

Many advanced material systems are being developed to meet fuel efficiency and performance requirements of the aerospace industry. One area of potential gain is in reducing structural weight. Al/Li alloys can provide immediate weight savings through direct substitution for materials currently used without the need for costly new manufacturing techniques which would be required in the case of organic matrix composites (157,158).

Lithium, with a specific gravity of 0.534, is the lightest of all metallic elements. When alloyed with aluminum, it reduces the density and increases the modulus more than is possible with any other alloying elements. For example, adding 1 % Li reduces alloy weight by 3 % and increases rigidity by 6 % (159-161). The specific modulus (modulus of elasticity/weight) of an alloy with 2.8 wt. % lithium is 26 % higher than that of alloy 7075-T651 (159,162).

The Al/Li sample used in the study was Alcoa 2090 alloy having the following nominal weight percentages of minor elements: Li=2.2, Cu=2.7, Zr=0.12.

B. Poly(Arylene Ether Sulfones)

Polysulfone belongs to the class of materials known as engineering thermoplastics. They are tough rigid materials with good mechanical and thermal properties. They can be used continuously under load bearing conditions over a wide range of temperature perhaps up to

40-50 C below their glass transition temperature. It is possible to process the polysufone by conventional methods such as injection molding or extrusion techniques, into products having excellent hydrolytic, thermal and dimensional stability. The physical and mechanical properties of polysulfone can be found in the literature (163,164).

In 1967 Johnson (165) described the synthesis of a large number of high molecular weight poly(arylene ether sulfones) via condensation of bisphenates with activated aromatic dihalides. This work led to the synthesis of bisphenol-A and dichlorodiphenyl-sulfone, and currently marketed by Union Carbide as UDEL Polysulfone. In this reaction, the ether bond is formed via the displacement of the halide by the phenoxide. Thus although the bisphenol may contain the sulfone group, this group forms an essential part of the dihalide. The electron withdrawing nature of the sulfone group activates the dihalides, thus facilitating displacement. The synthesis route is shown in equation [23]. A detailed synthesis procedure is described elsewhere (166,167).

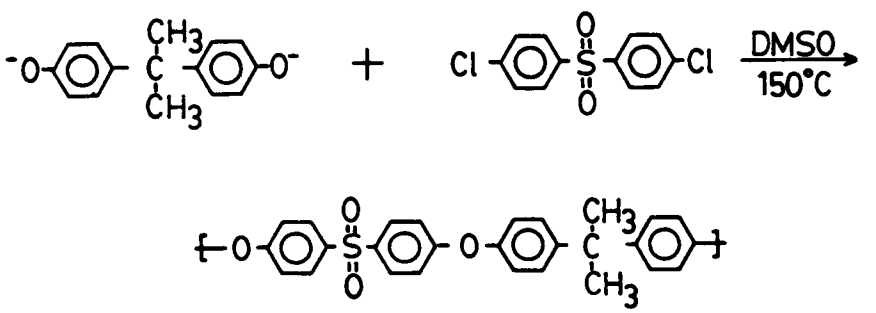

[23]

Thermoplastic polysulfone is utilized here as a model adhesive which unlike the crosslinked thermoset adhesives should have minimal chemical interaction with the Al/Li

oxide surface and is therefore ideal for studying the effect of porosity. Because polysulfone does not contain hardeners, filler and crosslinking agents, it is easier to analyze the failure surfaces by surface sensitive techniques. Another advantage of using a thermoplastic is that the adhesive can be dissolved away by using a solvent and the underlying substrate surface can be characterized. This report is the first instance in which the substrate surface was characterized after dissolution of the adhesive. The polysulfone was commercial grade UDEL-P1700 (Union Carbide) with a number average molecular weight of 26,000 g/mol, and a polydispersity of 2.0 (168).

RESULTS AND DISCUSSION

A. Lap Shear Test

The shear strengths of single overlap Al/Li joints are given in Table 5 for different surface pretreated samples. The phosphoric acid anodized (PAA) sample results in a shear strength of 25.0 MPa, the sulfuric acid anodized (SAA) sample results in a shear strength of 22.0 MPa, whereas the FPL etch pretreatment results in about 19.0 MPa for the shear strength.

One could state that the lap shear strength of the PAA sample is highest but the difference in lap shear strength between SAA and FPL etch pretreatment is not significant. In lap shear tests, because of the thin adherends, the tensile in-plane load causes considerable bending in the joint. Figure 12a shows the deformation of the lap shear joint when a load is applied. The bending results in shear-stress peaks near the ends of the overlap, which go to zero at the free surfaces. Also, the test specimen's adhesive shear stress is not constant, thus complicating the determination of a true shear strength (169,170). The shear stresses in the joint are shown in Fig. 12b. Thus, the lap shear test is not a good test to distinguish the effectiveness among surface pretreatments (171).

B. Wedge Test

In order to distinguish between surface pretreatments, one would do a wedge test. The durability from the crack opening wedge test is shown in Fig. 13. In

TABLE 5. Shear strength of single overlap Al/Li joints after different surface pretreatments.

Pretreatment	Lap shear strength (MPa)
FPL etch	19.0 +/- 1.0 (2770 psi)
SAA	22.0 +/- 1.0 (3140 psi)
PAA	25.0 +/- 1.0 (3670 psi)

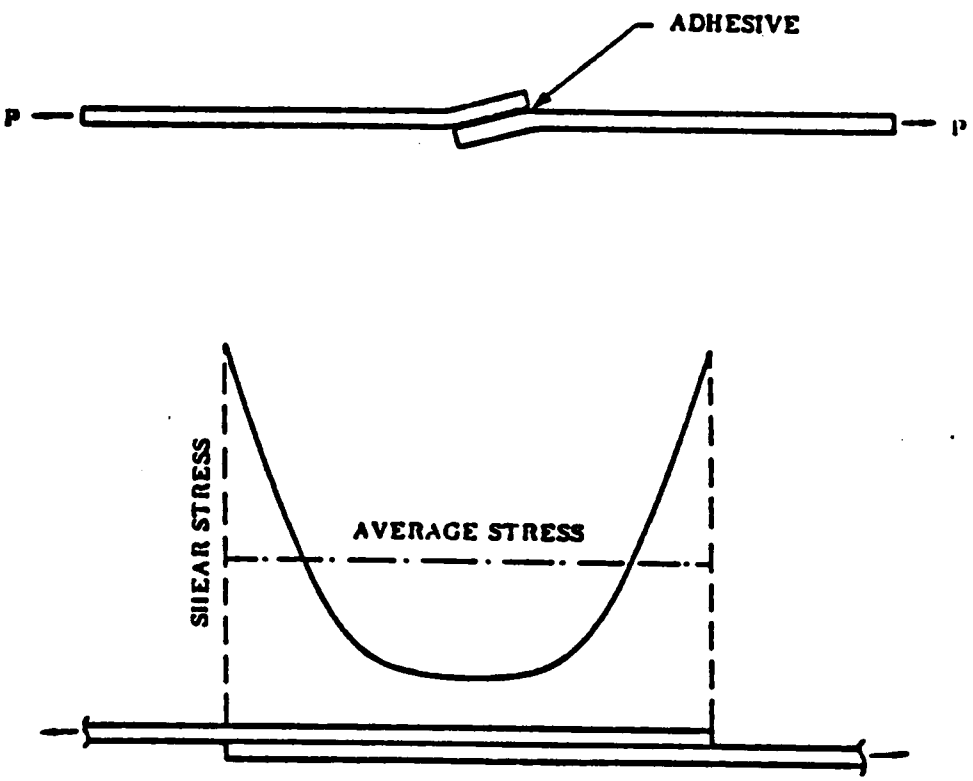

Figure 12. a) Deformation of a lap shear joint when load is applied, b) shear stress in a lap shear joint (169).

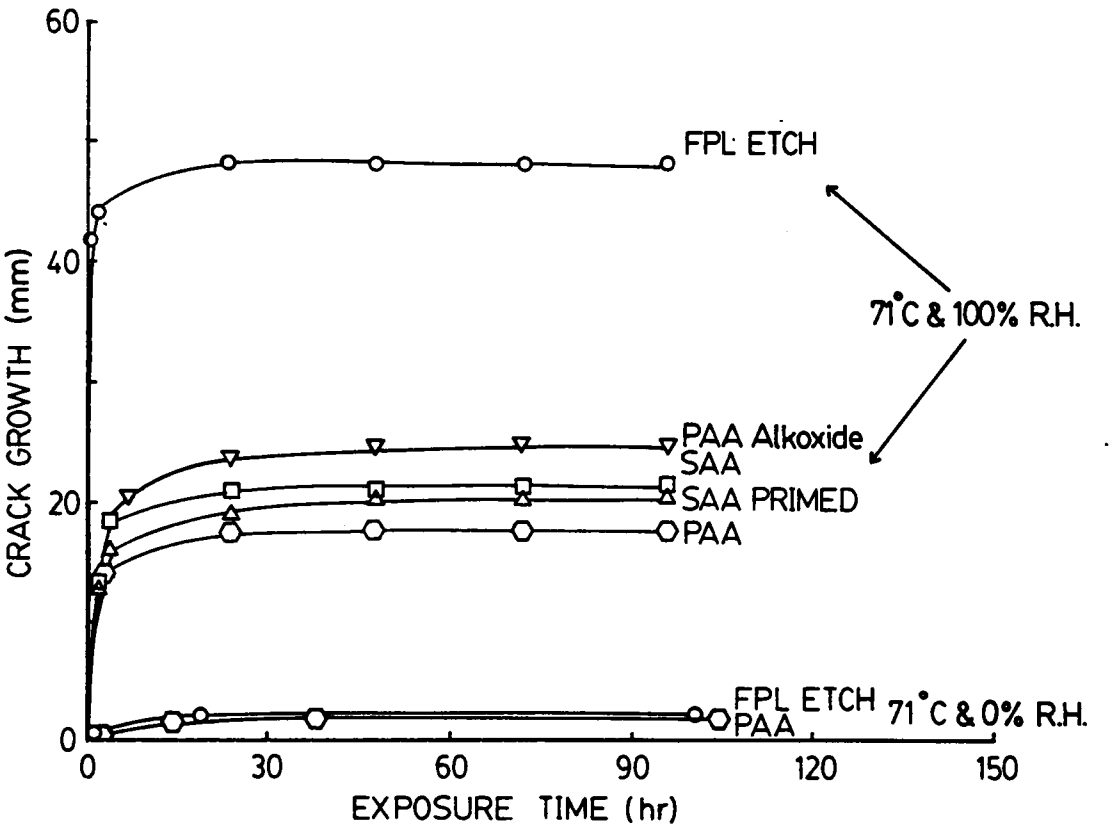

Figure 13. Crack growth versus time in a 71 C & 100 % R.H. environment and in a 71 C & 0 % R.H. environment.

the case for the FPL etch treatment, the crack length was 42 mm after being exposed to a hot-humid environment for only 30 minutes and the crack length finally leveled off to 48 mm after 24 hours of exposure. The SAA pretreatment improved the durability over the FPL pretreatment by a smaller crack length which was shown to be about one-half of the FPL value but still a significant length of 12 mm after 1/2 hour exposure in the hot-humid environment. The crack length leveled off to 20 mm after 24 hours of exposure. The PAA pretreatment improved bond durability over both the FPL etch and the SAA pretreatment. The crack length was 11.5 mm after 1/2 hour exposure and then leveled off to 17.5 mm after 24 hours of exposure in the environment.

The wedge test is important in that it gives durability information. Since differences between the surface pretreatments are clearly observed by the wedge test, then there must be a difference between the pretreatments and the paths of the crack propagation while the wedges were in the samples. The crack propagation of the failure depends on the stability of the oxide and on the polymer system used as an adhesive. Since the adhesive was the same polysulfone in this case, the stability of the oxide must be different to account for the durability differences observed by the wedge test. Here in order to study the Al/Li adherend surfaces prior to bonding and following fracture and to explain the difference between the two pretreatments, the resulting XPS and HSEM studies will be presented.

1. FPL Etched Sample

In Table 6, the binding energies (B.E.) in eV for each observed photopeak are tabulated along with the calculated values of the atomic fractions (A.F.) from the areas under the peaks combined with atomic sensitivity factors.

The O 1s photopeak assigned to the aluminum oxide at 531.7 eV also appears on the bare FPL etched surface. The S 2p peak on the bare etched surface is from the sulfur in sulfuric acid used in the FPL etch solution. The Al 2p peak signal is absent on the adhesive failure side (AFS). In addition, the oxygen atomic fraction is low when compared to the bare FPL etched surface. However, there is a high atomic fraction of both carbon and sulfur, which indicates that polysulfone used as the adhesive is attached to the AFS surface.

On the metal failure side (MFS), the S peak is not present. However, if the metal is exposed, then the sulfur from sulfuric acid used in the FPL solution should be exposed to the top layer. The reason why sulfur in sulfuric acid used in the FPL solution is not detected will be explained later in this section. The atomic fraction of carbon is low but the Al and O atomic fractions are high, indicating bare aluminum oxide. Therefore, the failure mode was interfacial failure. The absence of an Al 2p photopeak on the AFS side is additional confirmation of interfacial failure.

Supporting evidence for interfacial failure from the HSEM photomicrograph given in Fig. 14c for the AFS surface at 50,000 X magnification shows the polymer structure which was pulled out of the FPL oxide layer. The MFS (Fig

TABLE 6. XPS analysis of FPL etched Al/Li surfaces.

Photopeak	FPL Etch		FPL Etch MFS		FPL Etch AFS	
	B.E.(eV)	A.F.	B.E.(eV)	A.F.	B.E.(eV)	A.F.
C 1s	284.6	0.28	284.6	0.19	284.6	0.79
O 1s	531.7	0.51	531.6	0.63	531.9	0.18
Al 2p	74.1	0.19	73.9	0.17	----	NSP*
S 2p	168.4	0.01	----	NSP	167.8	0.03

*NSP = No Significant Peak (< 0.005 A.F.)

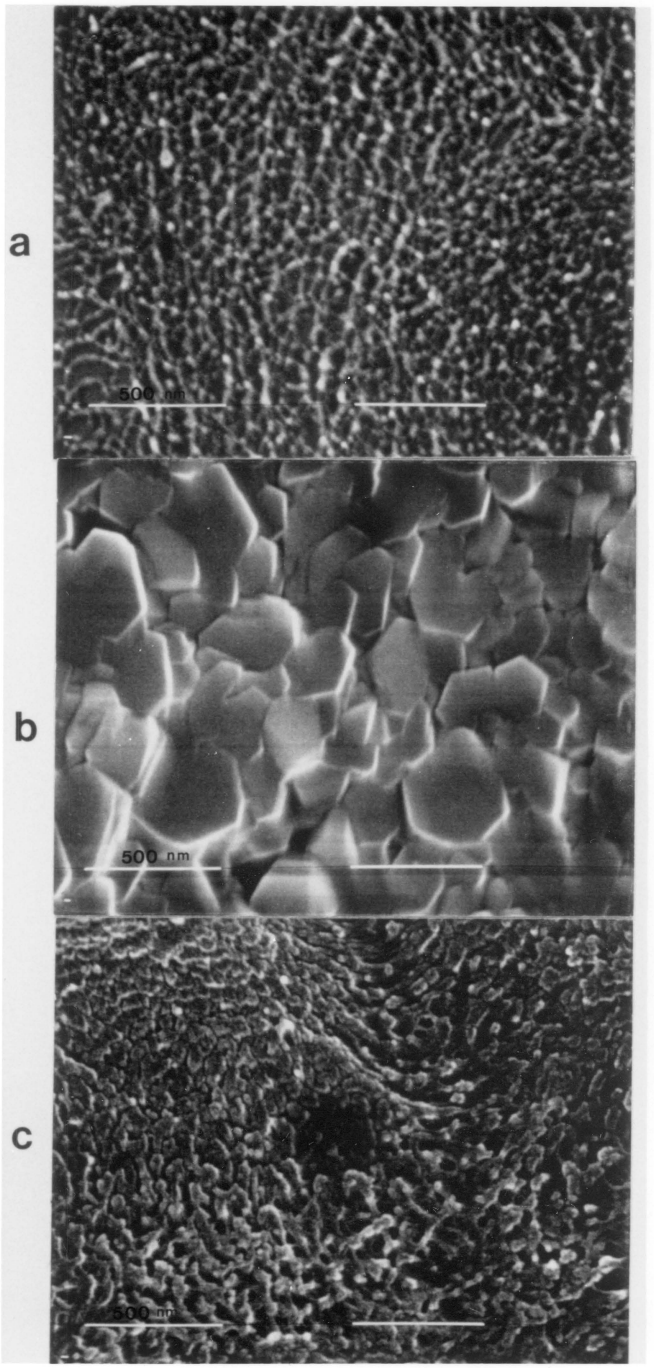

Figure 14. Surfaces of FPL etched samples, a) unbonded adherend, b) metal failure surface, and c) adhesive failure surface.

14b) at 50,000 X magnification shows the 'cornflake' structure as described by Venables (75). This cornflake structure is hydroxide formed by the reactions,

$Al_2O_3 + H_2O \longrightarrow 2\ AlOOH$,

$AlOOH + H_2O \longrightarrow Al(OH)_3$. [24]

The cornflakes are about 200 nm in diameter. Venables (75) have observed similar hydroxide structures (about 160 nm) for the Al 2024 alloy. The aluminum oxide became hydrated while the sample was in the 71 C and 100 % R.H. environment and its thickness increased. The reason why sulfur in the sulfuric acid used in the FPL solution is not detected is because the sulfate goes into solution in condensing vapor.

The MFS and AFS structures were representative of the whole sample indicating it was a clear interfacial rather than a mixed mode failure. These topographical results are in qualitative agreement with the XPS results reported above.

2. SAA Pretreated Samples Before and After Environmental Exposure

In Table 7, the binding energies (B.E) and the atomic fractions (A.F.) are given for SAA before and after exposure to 71 C and 100 % R.H. environment.

The O 1s photopeak assigned to the aluminum oxide at 531.5 eV appears on both the SAA Al/Li sample before and after environmental exposure. The Al 2p photopeak is present at 74.3 eV on both surfaces. The S 2p peak observed at 169.4 eV on the SAA bare surface before environmental exposure is from the sulfuric acid. The sulfur peak was not detected after environmental exposure.

TABLE 7. XPS analysis of SAA Al/Li surfaces before and after exposure to 71°C & 100 % R.H. environment.

Photopeak	SAA before environment exposure		SAA after environment exposure	
	B.E.(eV)	A.F.	B.E.(eV)	A.F.
C 1s	284.6	0.16	284.6	0.19
O 1s	531.5	0.56	531.3	0.62
Al 2p	74.3	0.24	73.8	0.20
S 2p	169.4	0.03	----	NSP
O/Al		2.3		3.1
S/Al		0.12		----

This is again possibly due to hydroxide formation during the elevated temperature-high humidity exposure. Indeed the atomic fraction of oxygen increased. However, the atomic fraction of both Al and S decreased. These results also support the conversion process of oxide to hydroxide.

HSEM photomicrographs are given in Fig. 15a for the SAA sample before environmental exposure. At 50,000 X magnification, the sample shows a "sponge" like pore structure with a pore diameter of about 30 nm. The photomicrograph of the SAA sample which has been exposed to the 71°C and 100 % R.H. environment for 90 hours is shown in Figure 15b. At 25,000 X magnification, the porous structure is no longer present and is converted to a "flake-like" structure and the average flake size is about 300-400 nm.

3. SAA Wedge Sample

In Table 8, the binding energies and atomic fractions are listed for the SAA sample after the wedge test. On the failure surface #1, the atomic fractions of both oxygen and aluminum are low compared to the bare SAA surface. However, there is a significant increase in the atomic fraction of carbon when compared to the unbonded SAA, and the sulfur peak binding energy is at 167.7 eV which is 1.7 eV lower than the S from the sulfuric acid. This lower binding energy photopeak is then due to sulfur in the polysulfone adhesive. The XPS results indicate that there is some polymer and some aluminum hydroxide on failure surface #1. The O 1s peak of neat polysulfone can be curve fitted into two same size peaks. One at 533.2 eV and another at 531.9 eV. Failure surface #2 shows a low

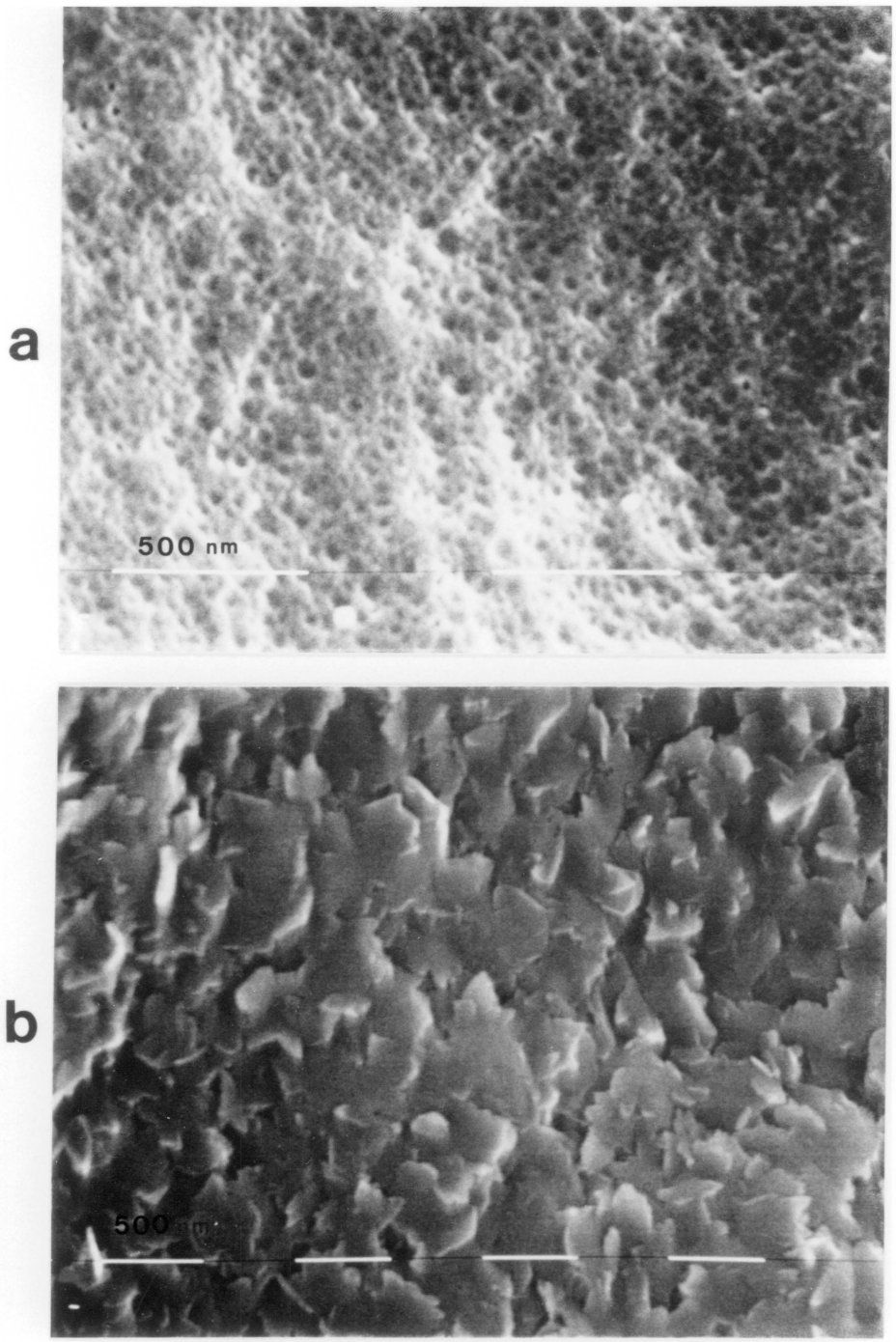

Figure 15. Surfaces of SAA samples, a) before exposure to environment, 50,000 X and b) after exposure to environment, 25,000 X.

TABLE 8. XPS analysis of SAA Al/Li surfaces

Photopeak	SAA (1)		SAA (2)	
	B.E.(eV)	A.F.	B.E.(eV)	A.F
C 1s	284.6	0.68	284.6	0.82
O 1s	533.0	0.27	533.2	0.15
			531.9	
Al 2p	75.4	0.03	----	NSP
S 2p	167.7	0.02	167.6	0.03

oxygen atomic fraction and no Al 2p peak, but the atomic fraction of carbon is high, even higher than failure surface #1, and the S peak from the polysulfone is present. Both the atomic fractions of carbon and sulfur are greater than on failure surface #1, indicating that failure surface #2 has more polymer present than failure surface #1. Therefore, this fracture was mainly cohesive failure with occasional divergence of the crack into the oxide.

In order to confirm the failure mode assignments, the HSEM photomicrographs in Fig. 16 are used. Failure surface #1 at 2,400 X magnification shows the 'flake' structure along with dark regions which are smooth polymer structures. At 25,000 X magnification, the hydroxide structure can be clearly seen with average size of 500 nm. Failure surface #2 was mostly smooth polymer structure, and the SEM photomicrograph at 100 X magnification shows both the polymer and the hydroxide surfaces but a greater proportion of the polymer adhesive structure. The one HSEM photomicrograph taken at 50,000 X magnification shows the polymer structure but the remaining sample had a smooth cleaved polymer structure and a very small proportion of aluminum hydroxide. Therefore, the HSEM photomicrographs confirm that the failure mode is mainly cohesive with the crack occasionally diverging to the oxide.

The aluminum (oxide) concentration on both of the failure surfaces was comparatively low when comparing the effects of the FPL etched and SAA pretreated samples. The extent of failure within the oxide appeared to have

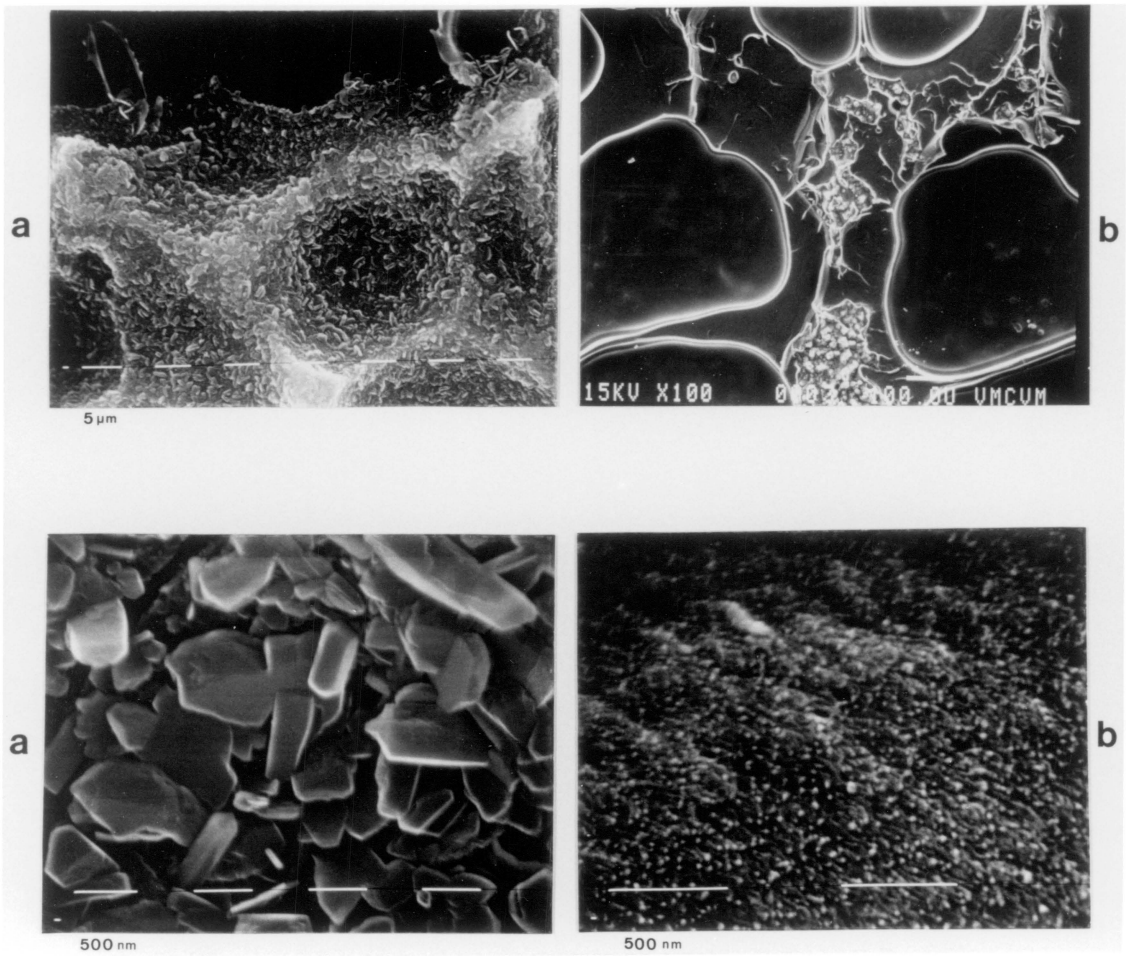

Figure 10. Surface of SAA samples, a) samples of failure side 1 and b) failure side 2.

decreased when compared to the FPL etched sample while the degree of the cohesive fracture of adhesive which is very close to the interface had increased. These observations are in agreement with the improved durability exhibited by the joints prepared using SAA pretreatment indicated by the wedge test results (see Fig. 13).

4. PAA Pretreated Samples Before and After Environmental Exposure

In Table 9, the binding energies and atomic fractions are listed for a PAA sample before and after exposure to the 71 C and 100 % R.H. environment. The O 1s photopeak assigned to the aluminum oxide at 531.3 eV appears on the PAA sample both before and after exposure (531.5 eV) to the hot-humid environment. The Al 2p photopeak is present on both surfaces before (74.2 eV) and after environmental exposure (74.0 eV). The P 2p photopeak at 133.9 eV on the PAA surface before environmental exposure is from the phosphoric acid. However, on the PAA bare surface after environmental exposure, the phosphorous peak is not present. The reason why the phosphorous peak is not detected is due to dissolution of the phosphate rather than being covered by the aluminum hydroxide crystals. This is consistent with a PAA sample studied by Davis et al. (172) in which the phosphate originally present is detected throughout the boehmite layer of the hydrated surface using Auger depth profiling. The atomic fraction of oxygen increased after exposure to the hot-humid environment while the atomic fraction of aluminum decreased after exposure to the environment. Also the O/Al ratio increased from 2.04 to 3.35 after environmental

TABLE 9. XPS analysis and curve fit results of PAA Al/Li surfaces before and after exposure to 71 C & 100 % R.H. environment.

Before Environmental Exposure

			Curve Fit		
Photopeak	B.E.(eV)	A.F.	B.E.(eV)	FWHM(eV)	Fractional Contribution
C 1s	284.6	0.23	286.2	1.6	0.18
			284.6	1.7	0.53
			283.2	1.8	0.21
O 1s	531.3	0.49	532.3	1.5	0.27
			531.3	1.5	0.42
			530.4	1.5	0.31
Al 2p	74.2	0.24	74.9	1.5	0.35
			74.0	1.4	0.48
			73.1	1.2	0.17
P 2p	133.9	0.03			
O/Al		2.04			

After Environmental Exposure

C 1s	284.6	0.27	286.2	1.5	0.13
			284.7	1.5	0.61
			283.8	1.5	0.19
O 1s	531.5	0.57	532.2	1.4	0.32
			531.5	1.2	0.48
			530.7	1.2	0.21
Al 2p	74.0	0.17	74.5	1.2	0.22
			74.0	1.3	0.58
			73.6	1.2	0.20
P 2p	----	NSP			
O/Al		3.35			

exposure. This confirms the formation of aluminum hydroxide on the bare pretreated surface when exposed to the hot-humid environment.

All of the above peaks were asymmetric, indicating that these elements exist in more than one bonding state. Curve fits of these photopeaks were done on the spectra obtained from the Perkin Elmer PHI spectrometer. Peak assignments were made using binding energies taken from the literature values (173). The curve fitting procedure was difficult in this experiment because the peak assignment of aluminum oxide and one of the peak of polysulfone was very similar. Therefore, curve fit data has to be analyzed with HSEM photomicrographs of failure surfaces to obtain correct failure mode.

The O 1s photopeak of PAA samples before and after environmental exposure is separated into three peaks as shown in Figure 17a and 17b, respectively. The atomic fractional contribution calculated from the curve fits are given in Table 9. When comparing atomic fractions before and after exposure to the hot-humid environment, the peak assigned to Al_2O_3 (530.4, 530.7 eV) is reduced and the peak assigned to $Al(OH)_3$ (532.3, 532.2 eV) is increased. The peak at 531.3 and 531.5 eV is from other oxides such as pseudo-boehmite and remains constant. The above curve fitting analysis is therefore consistent with the aluminum hydroxide formation reaction given in equation [24] in which Al_2O_3 is being converted to $Al(OH)_3$.

Stereo HSEM photomicrographs of a PAA sample before environmental exposure are shown in Fig. 18a. The 50,000 X magnification shows the fully developed whisker-like

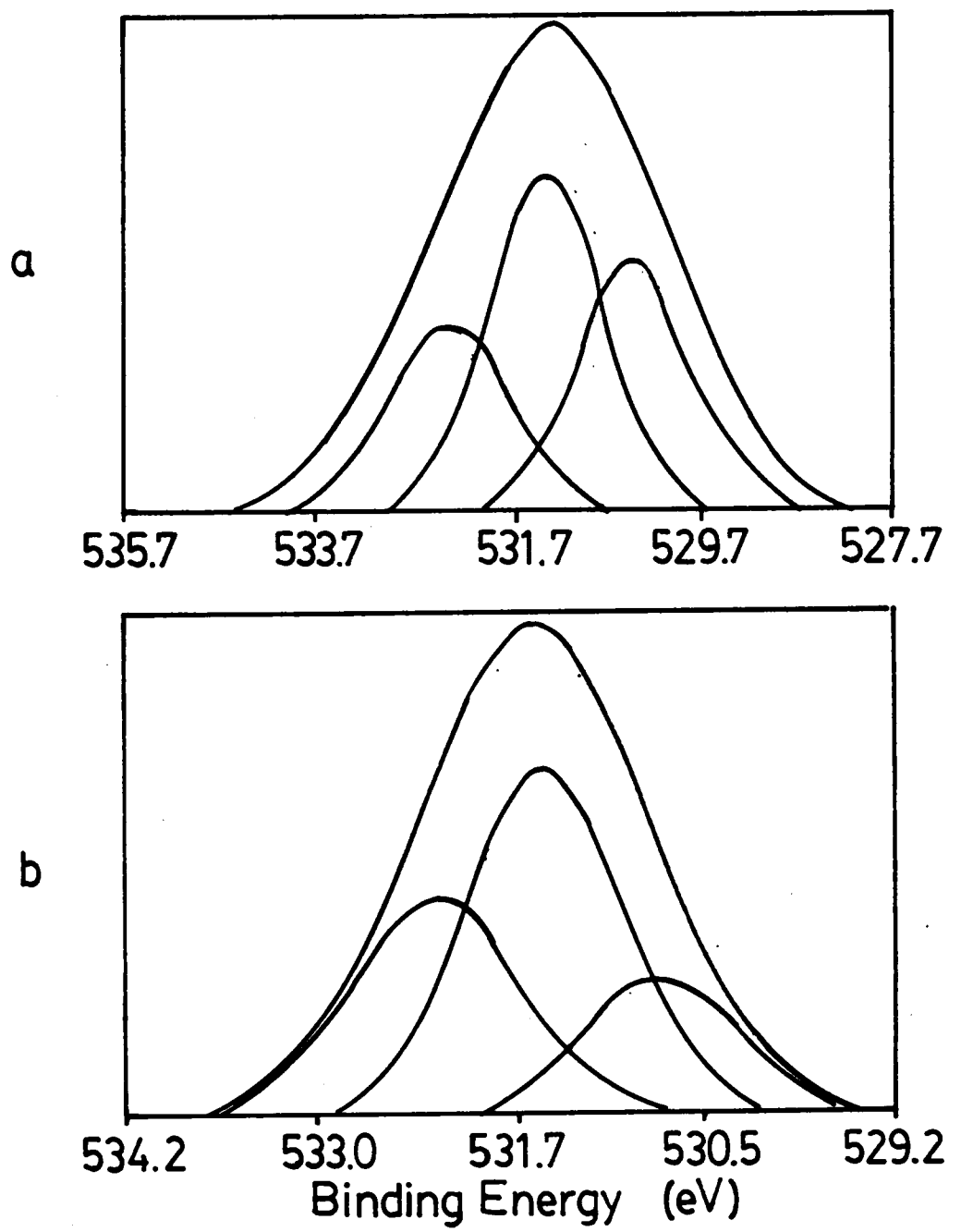

Figure 17. Curve fit O 1s photopeak of PAA samples, a) before exposure to environment, b) after exposure to 71 C & 100 % R.H. environment.

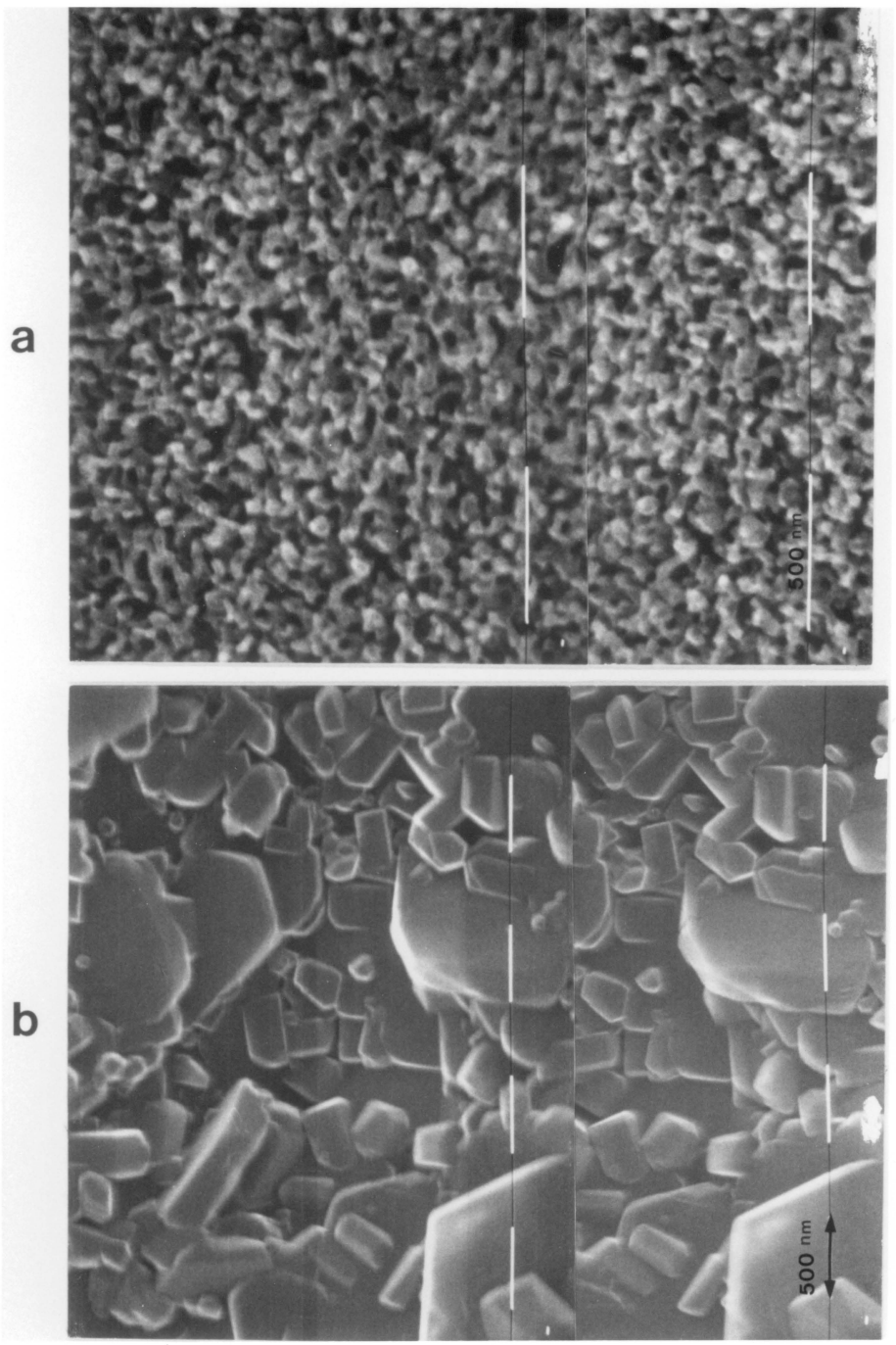

Figure 18. Stereo HSEM photomicrographs of PAA samples, a) before exposure to environment, 50,000 X and b) after exposure to environment, 25,000 X.

protrusion of the PAA oxide with a diameter of 100 nm into which primers and adhesives may penetrate and provide mechanical interlocking to a polymer and therefore exhibit a strong bond.

The PAA surface which was exposed to the 71°C and 100 % R.H. environment for 90 hours is shown in Fig. 18b. Stereo HSEM photomicrographs at 25,000 X magnification reveal that the hydroxide ranges in size from 100 nm to 1 um and lies flat on the substrate. Therefore, as the PAA aluminum oxide is hydrated to the hydroxide, failure may occur at the hydroxide/metal or hydroxide/adhesive interface.

The x-ray diffraction results are shown in Figures 19a and 19b for the PAA Al/Li samples before and after environmental exposure. No sign of crystallinity is observed for the PAA Al/Li sample before environmental exposure (Fig. 19a). However, for the PAA Al/Li sample after environmental exposure, very distinct crystalline peaks are observed as seen in Fig. 19b. This is due to bayerite in the crystalline sample (assigned to 2θ values of 18.7 and 38.6 peaks). This result is in agreement with the results reported by other workers (75,174).

5. PAA Wedge Sample

In Table 10, the binding energies and atomic fractions along with curve fit values are listed for the PAA failure surfaces #1 and #2. For the unbonded PAA Al/Li surface, the O 1s photopeak assigned to the aluminum oxide was at 531.3 eV and P from phosphoric acid was at 133.9 eV (see Table 9). No S photopeak is present. On the failure surface #1, the atomic fraction of oxygen is

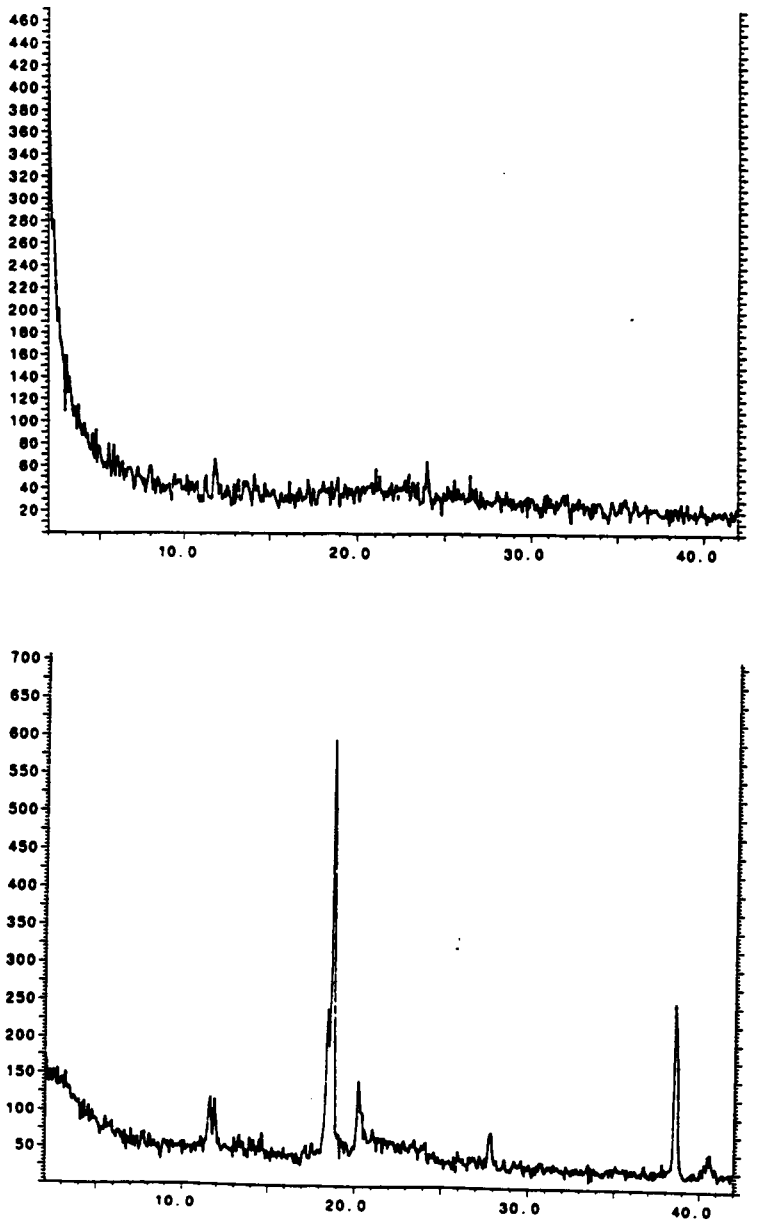

Figure 19. X-ray diffraction peaks of PAA Al/Li samples, a) before exposure to environment and b) after exposure to 71°C & 100 % R.H. environment.

TABLE 10. XPS analysis and curve fit results of bonded and failed PAA Al/Li surfaces.

PAA Failure Side #1

			Curve Fit		
Photopeak	B.E.(eV)	A.F.	B.E(eV)	FWHM(eV)	Fractional Contribution
C 1s	284.6	0.80	286.1	1.5	0.20
			284.6	1.5	0.69
			283.5	1.5	0.11
O 1s	533.1	0.17	533.2	1.7	0.57
	531.8		531.6	1.7	0.44
S 2p	167.7	0.03	168.7	1.4	0.42
			167.6	1.3	0.58
Al 2p	----	NSP			

PAA Failure Side #2

C 1s	284.6	0.50	286.3	1.5	0.31
			284.6	1.5	0.54
			283.3	1.5	0.10
O 1s	533.4	0.38	533.2	1.4	0.80
			531.6	1.7	0.20
S 2p	167.6	0.02	168.8	1.6	0.47
			167.5	1.3	0.53
Al 2p	75.9	0.10	----	----	----

low compared to unbonded PAA, and aluminum is not detected. However, there is a significant increase in the atomic fraction of carbon when compared to the unbonded PAA, and the sulfur photopeak is present at a binding energy of 167.7 eV. The sulfur peak at 167.7 eV is due to sulfur in the polysulfone adhesive. This indicates that there is some residual polymer and some aluminum hydroxide present on failure surface #1. On the failure surface #2, the atomic fractions of both oxygen and aluminum are low. Again, the atomic fraction of carbon is increased from the unbonded PAA, and the sulfur peak is present. Both the atomic fractions of carbon and sulfur are lower than on the failure surface #1, indicating that failure surface #2 has less adhesive present than on failure surface #1.

When comparing PAA failure surfaces #1 and #2, binding energies of the C 1s photopeak were assigned as follows. The carbon peak at the highest binding energy is typical of carbon bonded to oxygen. The next peak down in binding energy generally occurs at 1.5-1.7 eV from the first peak and is due to the carbon bonded to hydrogen. The next peak down in binding energy which occurs at 2.5-3.0 eV from the first peak is due to carbon bonded to a phenyl ring.

For the oxygen photopeaks, the highest binding energy peak is generally due to oxygen in aluminum hydroxide $Al(OH)_3$. The next peak down in binding energy which occurs 0.6-0.8 eV from the first peak is due to oxygen in the C-O-C group. The next peak down in binding energy which occurs 1.0-1.7 eV from the first peak is due to oxygen in the sulfone (O=S=O) bond. On failure surface

#1, all the oxygen peaks are due to polysulfone that is, the C-O-C and O=S=O groups; however, on failure surface #2, the atomic fraction of oxygen due to the O=S=O and C-O-C peaks is decreased and the peak assigned to $Al(OH)_3$ is present, which is consistent in that it indicates that the failure surface #1 has more polymer, and failure surface #2 has some aluminum hydroxide present.

In addition to the XPS results, the HSEM photomicrographs in Figures 20 and 21 were taken. The unbonded PAA surface which showed the porous oxide was given in Fig. 18a. Failure surface #1 in Fig. 20a at 150 X reveals cohesive failure of the polymer with the crack diverging into the oxide layer. At 9,600 X magnification of the hydroxide, the hydroxide flakes can be clearly seen with an average size of 2.0 μm. At 50,000 X magnification of the polymer surface, the fractured or cleaved polymer surface can be seen. Since the polymer surface does not reveal the opposite surface of the oxide or hydroxide, it can be concluded that it is indeed a fractured polymer surface.

The failure surface #2 at 150 X in Fig. 21a shows a similar structure as the failure surface #1. However, the stereo photomicrograph at 9,600 X magnification shows the hydroxide that stands on top of the base metal with an average size of 3.0 um. The hydroxide flake form is quite different from the flake form of the failure surface #1 (see Fig. 20b), but is similar to that found on pretreated PAA exposed to the same hot-humid environment for 90 hours. The photomicrographs taken of the polymer side of failure surface #2 in Figure 21c show the polymer whiskers

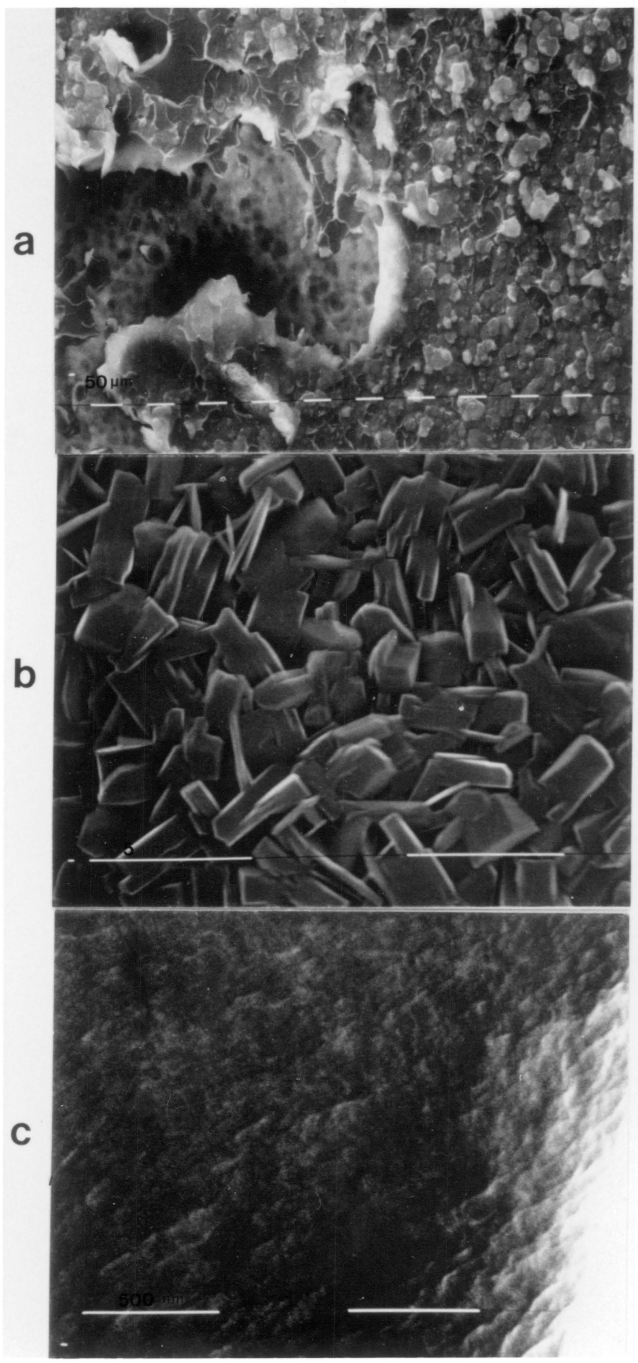

Figure 20. HSEM photomicrographs of PAA samples of failure side #1, a) 150 X, b) 9,600 X, c) 50,000 X.

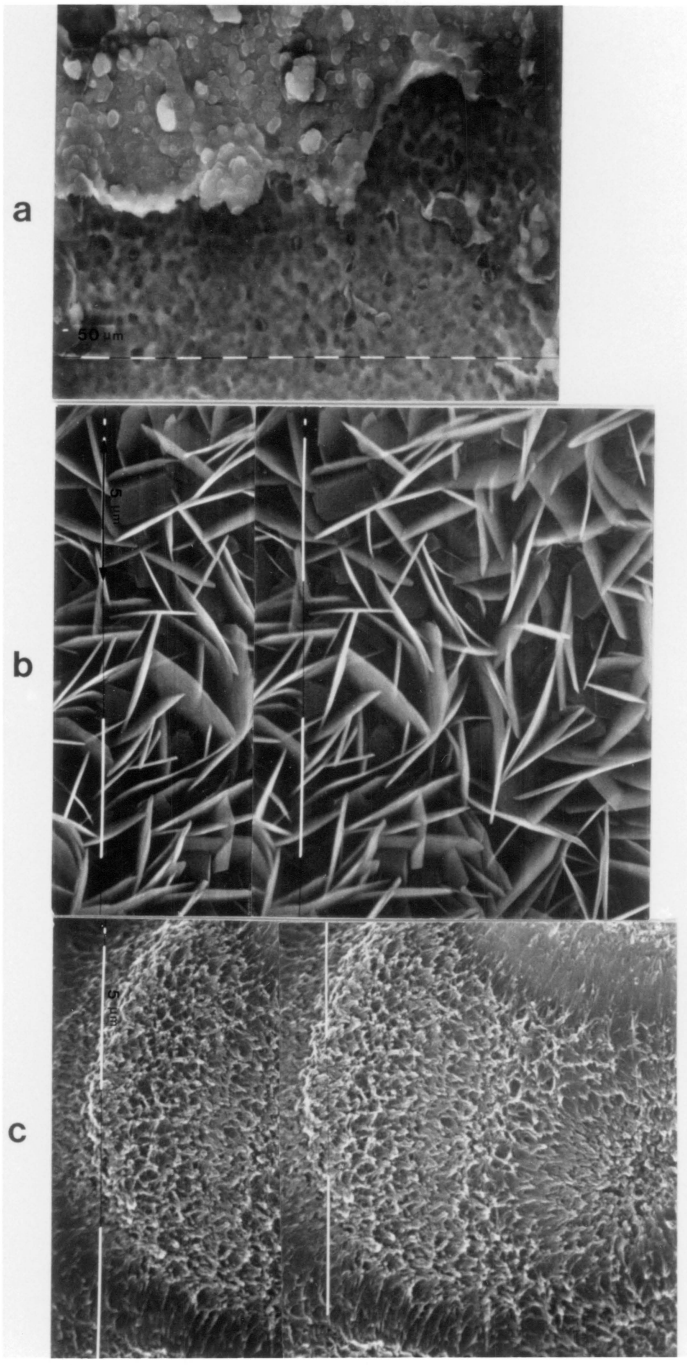

Figure 21. Stereo photomicrographs of PAA sample of failure side #2, a) 150 X, b) 9,600 X, c) 9,600 X.

on the opposite side of the PAA oxide with whisker size of 100 nm. This may be the case where there was interfacial failure in which the polymer was simply pulled out of the pores as the wedge crack advanced. However, as discussed above, failure occurred partially within the oxide layer. The hydroxide formed on failure surface #2 differs physically from the hydroxide on failure surface #1.

The EDX analysis is given in Figure 22a for the hydroxide formation on failure surface #2 of the PAA Al/Li wedge sample. Hydroxide formed on the PAA bare surface that was exposed to the 71°C and 100 % R.H. environment is shown in Fig. 22b. Both of these surfaces give signals due to Al and Cu. Copper is from the Al/Li alloy which contains 2.9 % Cu as an alloying element. So it is concluded that the different morphologies of these hydroxides are not due to metal sulfates. Perhaps the difference is due to differences in crystallinity. The reason why EDX picks up Cu whereas XPS does not is that the analysis depth of EDX is 1-2 μm, much less than XPS which is only 5-10 nm, thus it does not probe the underlying metal.

The failure mode for PAA Al/Li sample was mainly cohesive failure with the crack occasionally diverging to the oxide and the base adherend. Therefore, for the PAA pretreated samples, the durability was superior when compared to the FPL etched adherends.

C. Wedge Test in 71°C & 0 % R.H. Environment

Wedge samples were tested in 71° C and 0 % R.H. environment to observe if high temperature without the

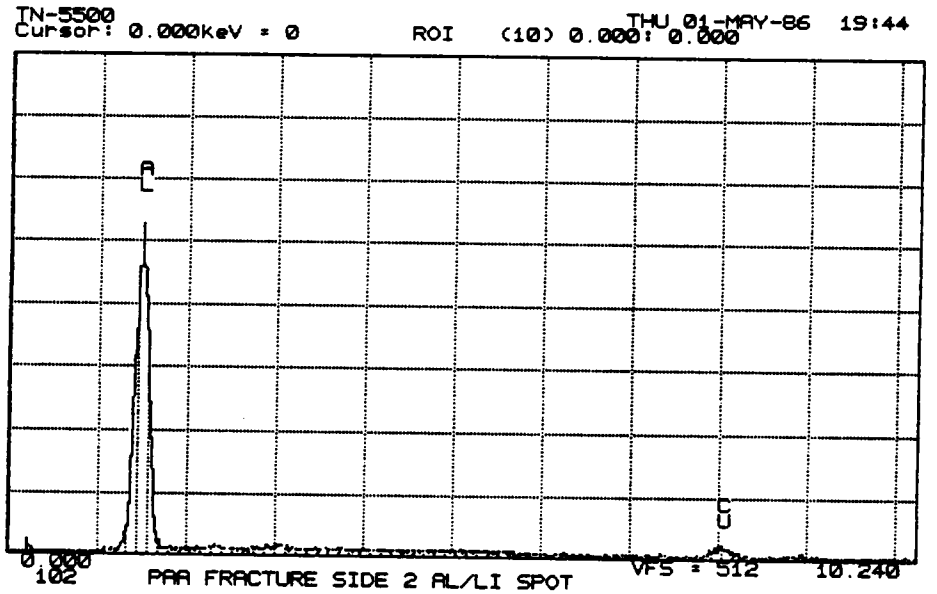

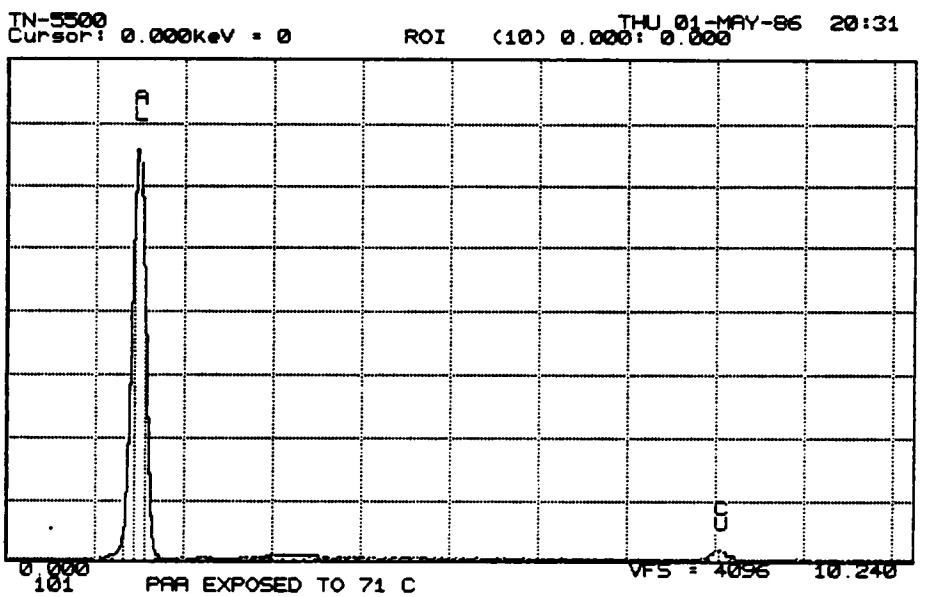

Figure 22. EDX result of a) failure surface #2 of the PAA Al/Li wedge sample (see Fig. 21b), b) PAA bare surface after exposure to the 71°C & 100 % R.H. environment (see Fig. 18b).

humidity would influence crack propagation.

In this experiment, for the two surface pretreatments (FPL etch and PAA), there was no difference in the bond durability from the crack opening wedge test as shown by the two curves at the bottom of Fig. 13. The crack in FPL etched Al/Li grew to only 0.875 mm after being exposed to the 71 C and 0 % R.H. environment for 30 min and the crack growth finally leveled off at 2.22 mm after 24 hours of exposure. The results are in sharp contrast to the same test done at 100 % R.H. (top curve in Fig. 13). For the PAA pretreatment, the crack grew to 0.375 mm after 30 min exposure in the 71°C and 0 % R.H. environment. The crack growth leveled off to 2.0 mm after 24 hours of exposure, again in contrast to the 100 % R.H. case.

In Table 11, the binding energies and atomic fractions are listed for the FPL etch failure surfaces #1 and #2. On failure surface #1, the atomic percent of oxygen is low and aluminum is not detected. However, there is a significant increase in the atomic percent of carbon when compared to the unbonded PAA, and the sulfur photopeak is present at a binding energy of 167.8 eV. For the oxygen photopeaks, the high binding energy peak (533.0 eV) is due to oxygen in the C-O-C group of the polysulfone adhesive. The low binding energy peak (531.6 eV) is due to oxygen in the sulfone (O=S=O) bond. The XPS results indicate that polysulfone used as the adhesive is attached to failure surface #1.

On the failure surface #2, the atomic percent of oxygen is low but Al is detected. Again, the atomic percent of carbon is increased from the unbonded PAA, and

TABLE 11. XPS analysis of FPL etched Al/Li surfaces in 71°C and 0 % R.H. environment.

Photopeak	Failure Surface #1		Failure Surface #2	
	B.E.(eV)	A.F.	B.E.(eV)	A.F.
C 1s	284.6	0.81	284.6	0.69
O 1s	533.1	0.16	533.0	0.24
	531.7		531.6	
Al 2p	----	NSP	74.1	0.03
S 2p	167.7	0.03	167.8	0.03

the sulfur peak is present as well. The atomic percent of carbon is lower than on the failure surface #1, indicating that failure surface #2 has some aluminum oxide present as well as the adhesive. Therefore, the failure mode for the FPL etched Al/Li sample was mainly cohesive failure with the crack occasionally diverging into the surface oxide layer. HSEM was utilized for studying the failure surface topography and basically the interpretation of the photomicrographs was consistent with the XPS results.

In Table 12, the binding energies and atomic percentages are listed for the PAA failure surfaces #1 and #2. On failure surface #1, the atomic percent of oxygen is low and aluminum is not detected. However, there is a significant increase in the atomic percent of carbon when compared to the unbonded PAA, and the sulfur photopeak is present at a binding energy of 167.7 eV. The sulfur peak at 167.7 eV is due to sulfur in the polysulfone adhesive. This indicates that there is only polysulfone on failure surface #1.

On the failure surface #2, again the atomic percent of oxygen is low and aluminum is not detected. A high atomic percent of carbon is detected as well as sulfur at 167.7 eV. Therefore, this failure surface contains only polysulfone as did failure surface #1. Thus, it was a cohesive failure. Again, the HSEM photomicrographs of the failed surfaces were consistent with the XPS results.

This test also shows that residual moisture left from the surface preparation step cannot cause formation of the hydrated oxide, but rather moisture penetrating from the surrounding environment.

TABLE 12. XPS analysis of PAA Al/Li surfaces in 71°C and 0 % R.H. environment

Photopeak	Failure Surface #1		Failure Surface #2	
	B.E.(eV)	A.F.	B.E.(eV)	A.F.
C 1s	284.6	0.8	284.6	0.78
O 1s	533.2	0.17	533.2	0.19
	531.9		531.8	
Al 2p	----	NSP	----	NSP
S 2p	167.7	0.03	167.7	0.03

In terms of thermodynamic wetting equation, the work of adhesion in a dry and a moist environment was given in the LITERATURE REVIEW section as equations [7] and [10] which are repeated here assuming $\Pi_e \approx 0$.

$$W_A = 2(\gamma_s^D \gamma_a^D)^{1/2} + 2(\gamma_s^P \gamma_a^P)^{1/2} \quad [7]$$

$$W_{A1} = 2[\gamma_{lv} - (\gamma_a^D \gamma_{lv}^D)^{1/2} - (\gamma_a^P \gamma_{lv}^P)^{1/2} - (\gamma_s^D \gamma_{lv}^D)^{1/2} - (\gamma_s^P \gamma_{lv}^P)^{1/2} + (\gamma_a^D \gamma_s^D)^{1/2} + (\gamma_a^P \gamma_s^P)^{1/2}] \quad [10]$$

Gamma values for polysulfone, anodized aluminum, and water (40,41,175) are listed in Table 13. The work of adhesion between polysulfone and anodized aluminum in a dry condition is calculated to be 139.0 mJ/m^2. The work of adhesion in a moist environment is calculated to be 10.0 mJ/m^2, indicating that the bond may be thermodynamically stable in moist environment, and as discussed earlier, interfacial failure is not observed for the PAA Al/Li bonded samples in a hot-moist environment. Loss of strength may be due to other processes such as hydration of aluminum oxides. Since thermodynamics describes the behavior of the joint at equilibrium, a joint which is predicted to fail in a liquid because W_{A1} is low or negative will not fail instantaneously because the liquid must first penetrate the adhesive to reach the interfacial region. The bond might therefore be expected progressively to weaken as ingression of liquid into the joint occurs. The failure mode of the joint might also change as moisture hydrates the oxide layer.

Thus, moisture lowers the work of adhesion calculated by the thermodynamic work of adhesion, but in considering the behavior of adhesive joints under hostile

TABLE 13. Surface free energies of anodized aluminum adherend, polysulfone adhesive, and water (40,41,175).

	γ^p	γ^d	$\gamma(mJ/m^2)$
PSF	26.1	3.6	29.7
Anodized Al	125	44.0	169
H_2O	22	50.2	72.2

environments, other factors besides thermodynamic considerations are important. These include the mechanical interlocking contribution, the kinetics of penetration of liquids into joints, stability of the adhesive and the oxide layer in the moist environment, and the effects of stress on the crack tip under environmental attack.

For the Al/Li-PSF bond, the mechanism of failure is due to moisture which causes the hydration and subsequent debonding of PSF from the hydrated oxide layer.

The evolution of hydration process has been analyzed by Davis et al. (172) using a ellipsometry technique which is very sensitive to surface changes such as those that are associated with the oxide to hydroxide conversion. The first step involves hydration of the surface $AlPO_4$ layer. This process may occur during storage, but the state of hydration at any given time will depend upon the prior history of the sample. In this regard, they noted that the incubation time for hydration of PAA oxides can vary significantly depending upon drying conditions after anodization. Incubation time is defined as the time interval before the specimen began to hydrate. Physically, this is where the oxide porosity begins to fill in and the surface begins to roughen considerably. The second step is the formation of AlOOH, the cornflake structure. This apparently involves slow dissolution of the hydrated phosphate and nearly simultaneous hydration of the oxide with the rate-controlling process that of phosphate dissolution.

The third step of hydration involves the nucleation

and growth of the bayerite phase, Al_2O_3. The bayerite nucleates on the platelets of the boehmite phase leading to a duplex layer of bayerite on top of boehmite (176).

These results, obtained with the aid of surface behavior diagrams (172), indicate that the phosphate content of a PAA oxide plays a significant role in determining the stability of the surface in a moist environment. The conclusion that the dissolution of the phosphate is rate controlling up to the point where the surface layer is transformed to boehmite appears particularly significant. The result suggests that the presence of the phosphate is partly responsible for the greater stability of PAA oxide relative to FPL oxides.

The wedge test result using a thermoplastic adhesive is different than the wedge test of thermoset epoxy material. Venables (6) using epoxy to bond aluminum samples reported that the failure of the bond was caused directly by the conversion of oxide to hydroxide. Once the hydroxide forms, it separates from the adherend, that is, the cornflake hydroxide debonds from the aluminum metal giving rise to bond failure. The newly exposed aluminum metal surface then hydrates further as the crack opens up. The proposed failure model is shown schematically in Fig. 23.

However, the hydration studies were done without the adhesive applied to the aluminum substrate. The thermoplastic adhesive's advantage lies in the fact that the PSF adhesive can be dissolved away by chloroform and the underlying surface can be studied. In the presence of adhesive, the oxide does not readily convert to the

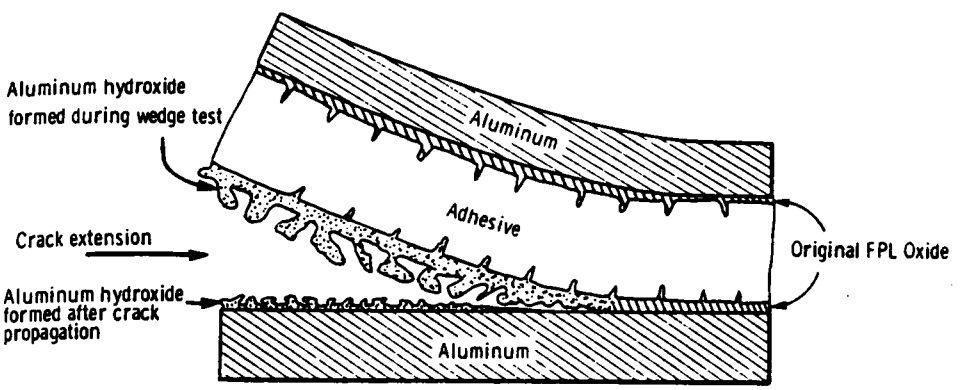

Figure 23. Schematic drawing of the mechanism deduced for crack propagation during wedge testing. In the humid environment, the original FPL oxide is converted to a hydroxide which adheres poorly to the Al substrate (6).

cornflake hydroxide but the oxide's pores are filled and the surface begins to roughen. This is shown in Figs. 24a and 24b for the Al 7075 samples bonded with polysulfone where a region just ahead of crack tip and a region just behind the crack tip are analyzed by HSEM. As shown in Fig. 24a the region just ahead of crack tip after environmental exposure shows a porous surface. The region just behind crack tip as shown in Fig. 24b shows a somewhat hydrated surface with some pores being filled.

Therefore, for the FPL etched case, once placed in hot moist environment, although remnants of the oxide remain, the protrusions no longer exists just ahead of the crack tip, leaving a relatively smooth surface. The polysulfone adhesive is displaced, interfacial failure between PSF and aluminum oxide occurs, then the exposed aluminum oxide is further hydrated to the cornflake structure. This proposed model is shown schematically in Fig. 25a. Note that the failure is at the polysulfone-oxide rather than at the hydroxide-metal interface reported by Venables.

For the PAA case, where the mechanical interlocking contribution is greater than the FPL case due to a deeper porous oxide layer, the oxide is more stable against the moisture due to increased thickness, as well as due to the presence of phosphate, which is known to increase durability of aluminum bonds (75). The crack growth is initially cohesive but as porous oxide begins to fill in by moisture intrusion, some PSF is displaced and the crack diverged to the oxide, but because of the mechanical interlocking contribution, the crack moves back to the

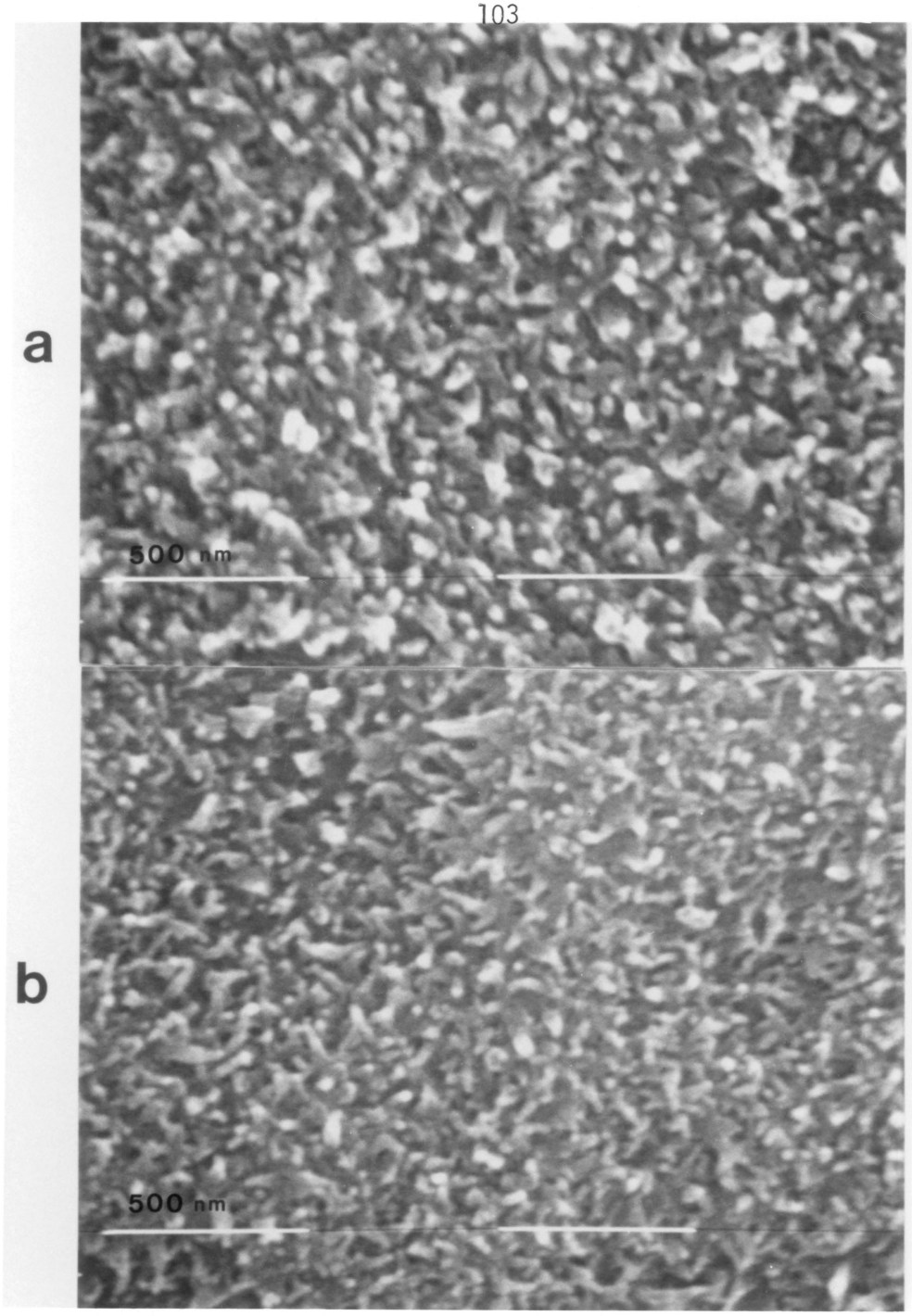

Figure 24. HSEM photomicrographs of PAA Al 7075 after wedge test and after polysulfone has been dissolved away with chloroform, a) just ahead of the crack tip, 50,000 X and b) just behind the crack tip, 50,000 X.

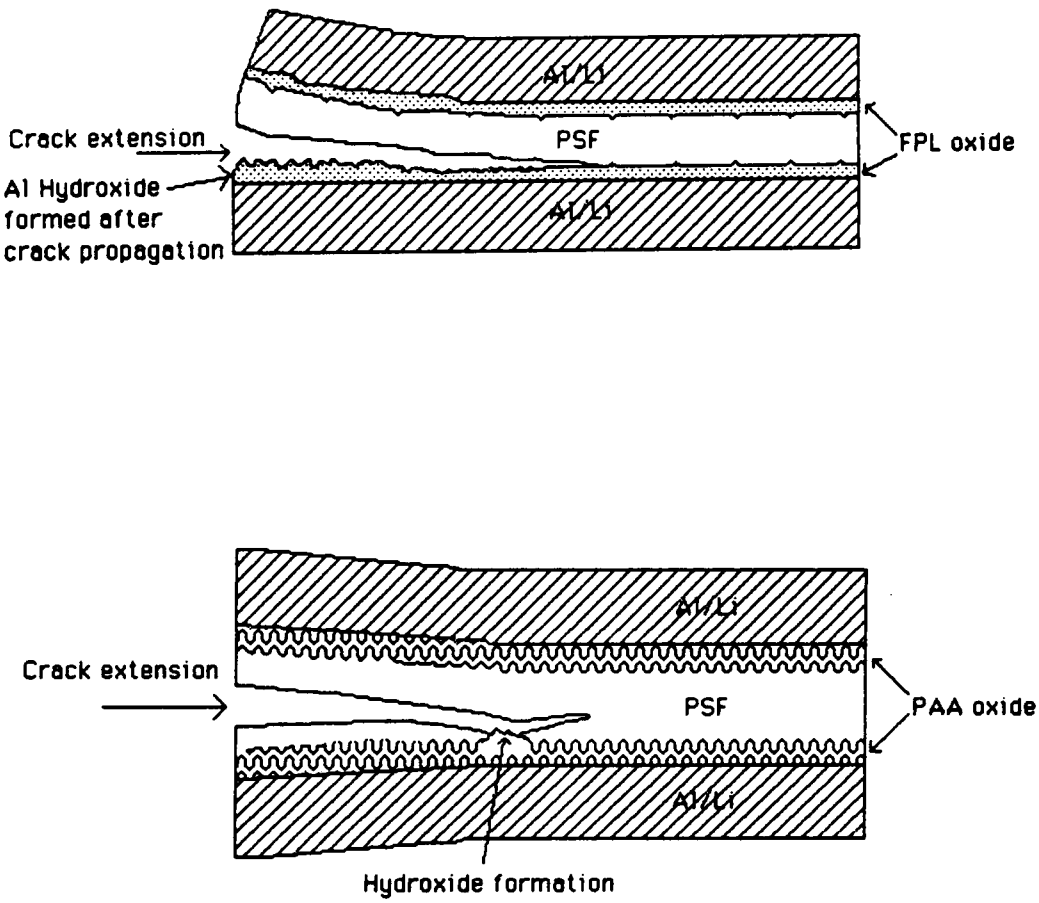

Figure 25. Schematic drawing of the mechanism deduced for crack propagation during wedge testing of PSF-Al/Li bond, a) FPL etch and b) PAA pretreatment.

adhesive, i.e. being cohesive failure. Again the exposed aluminum oxide is further hydrated to the cornflake structure. The final failure mode is cohesive failure with occasional divergence of the crack into the PSF-oxide interface. The new proposed mechanism is shown schematically in Fig. 25b.

D. Comparison Of Surface Preparation Methods By Fracture Energies

The fracture energies for the wedge samples can be calculated by using the expression

$$G_I = P^2\ 2\ [3(a+0.6\ h)^2 + h^2]/6bEI \qquad [25]$$

given by Mostovoy et al. (177) for the uniform double cantilever beam specimen. In the equation, G_I is the model fracture energy, P is the applied load, b is the specimen width, h is the beam height, a is the crack length from P to crack tip, E is the Young's modulus of aluminum, I is the beam moment of inertia which is $bh^3/12$ and 0.6 h is the correction factor for rotation about crack tip (determined experimentally for a monolithic specimen).

The limitation of the above equation is that the measurement of P is necessary. By measuring displacement at the load point, however, it is not necessary to measure P, and G_I can be calculated by using the following expression (178,179).

$$G_I = y^2Eh^3[3(a+0.6h)^2+h^2]/16[(a+0.6h)^3+ah^2]^2 \qquad [26]$$

where y is the displacement at the load point (wedge thickness). The results for initial crack length and crack growth during exposure to the hot-humid environment

for 1/2 hour are given in Table 14 together with the corresponding values of the fracture energy. The results show that PAA has the highest fracture energy, whereas the FPL etched sample has the lowest fracture energy. This result agrees qualitatively with the wedge test results in that the PAA and SAA durabilities were superior to the FPL etched samples.

E. Penetration of Polysulfone

1. Preferential Dissolution of Al/Li Alloy and Oxide

In order to determine if the polysulfone molecules could penetrate into a pore of the PAA sample, the end-to-end distance of polysulfone molecule was calculated using equation [12] and considering short range interactions. Taking the molecular weight of PSF as 26,000 g/mol, and n=26,000/442, l 2.23 nm, $(r^2)^{1/2}$ is calculated as 24.0 nm.

This calculated end-to-end distance indicates that the polysulfone chains are able to penetrate into the pores of anodized Al/Li (100-200 nm in diameter) substrate and provide mechanical interlock with the porous oxide layer. Recall earlier discussion in the LITERATURE REVIEW section where Venables et al. reported 10 fold increase in peel adhesion due to porous oxide whereas the increase in the interfacial area for bonding was only about 10 % (18). Therefore mechanical interlocking is important in enhancing adhesive bond strengths.

The penetration of the polysulfone into the micropores produced by anodization of the adherend is gauged by preferentially dissolving away the Al/Li alloy

TABLE 14. Wedge crack test results showing crack lengths and corresponding fracture energies.

Surface Treatment	a (mm)	G_1 (J/m^2)
FPL etch	52	9.9×10^{-2}
SAA	33	4.14×10^{-3}
PAA	22	18.1×10^{-3}

a = crack length from load point to the crack tip after 1/2 hour in 71 C and 100 % R.H. environment. This includes initial crack length.

and the oxide leaving the polymer structure for subsequent examination in the electron microscope. The stereo HSEM photomicrograph shown in Figure 26 reveals that the polysulfone had indeed penetrated into the porous oxide when thermally pressed at 290°C. The size of the polymer "cylinders" which penetrated into the micropores is 100-200 nm in diameter which corresponds to the pore size of the PAA pretreated sample. XPS results on the polysulfone film confirmed that the structure observed is indeed polysulfone and not aluminum oxide.

The HSEM photomicrograph in Figure 27a shows the 3 wt. % polysulfone primer had also penetrated into the oxide layer when solvent cast in chloroform again with a size of 100-200 nm. A sample of neat polysulfone was not affected by the 5 % NaOH used to dissolve Al/Li alloy and its oxide layer as shown in the rather featureless photomicrograph in Figure 27b. The topography of a neat PSF film before 5 % NaOH solution exposure was same as the topography after exposure.

2. TEM of Microtomed PAA Al/Li Samples

The TEM photomicrographs shown in Figures 28 and 29 reveal certain features apparent on all the ultramicrotomed sections examined. The lower half of the micrograph in Fig. 28 shows a section through the aluminum oxide substrate. The upper half of the micrograph shows a section of PSF which was thermally pressed onto the oxide, although in many cases this was observed detached from the specimen. The section consisted of bands of porous film of varying thickness. This was probably due to the difficulty in maintaining the fracture along the same

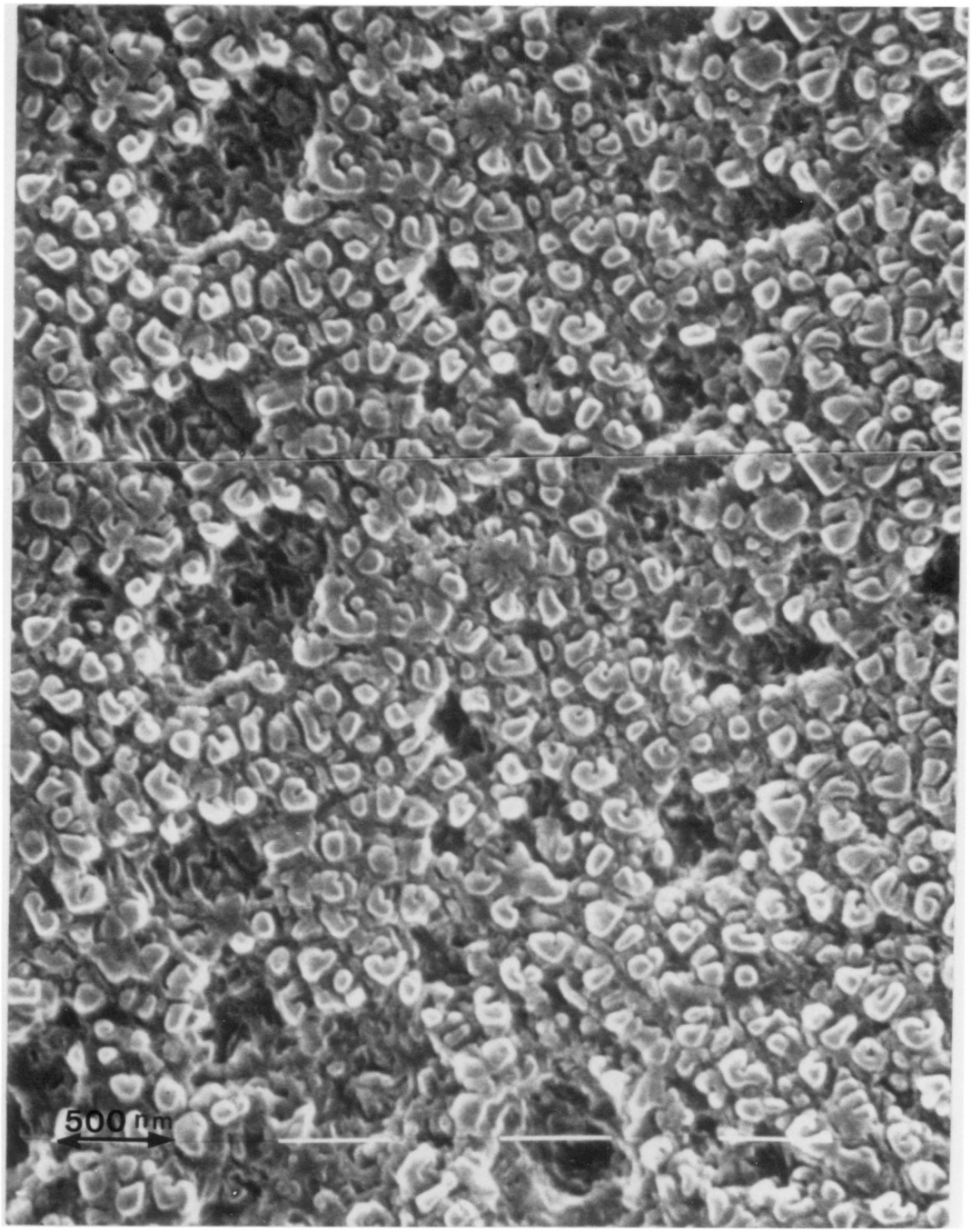

Figure 26. Stereo HSEM photomicrographs of the polysulfone surface after removing Al/Li alloy and its oxide layer.

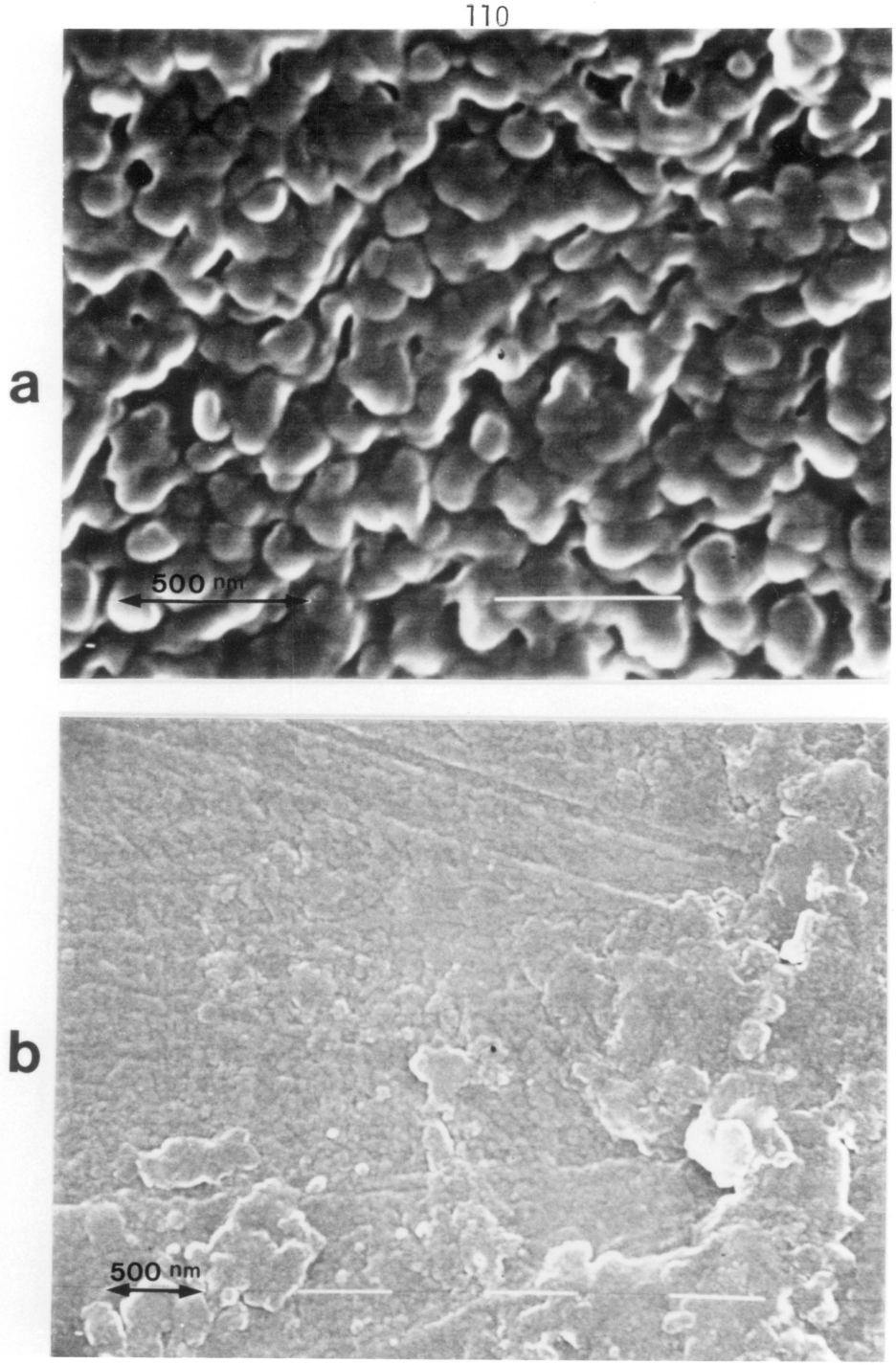

Figure 27. HSEM photomicrographs of polysulfone, a) polysulfone primed surface after removing Al/Li alloy and its oxide and b) polysulfone after exposure to the 5 % NaOH solution.

Figure 28. Transmission electron micrograph of ultramicrotomed section cut transversely through PAA Al/Li oxide-polysulfone interface, 29,000 X.

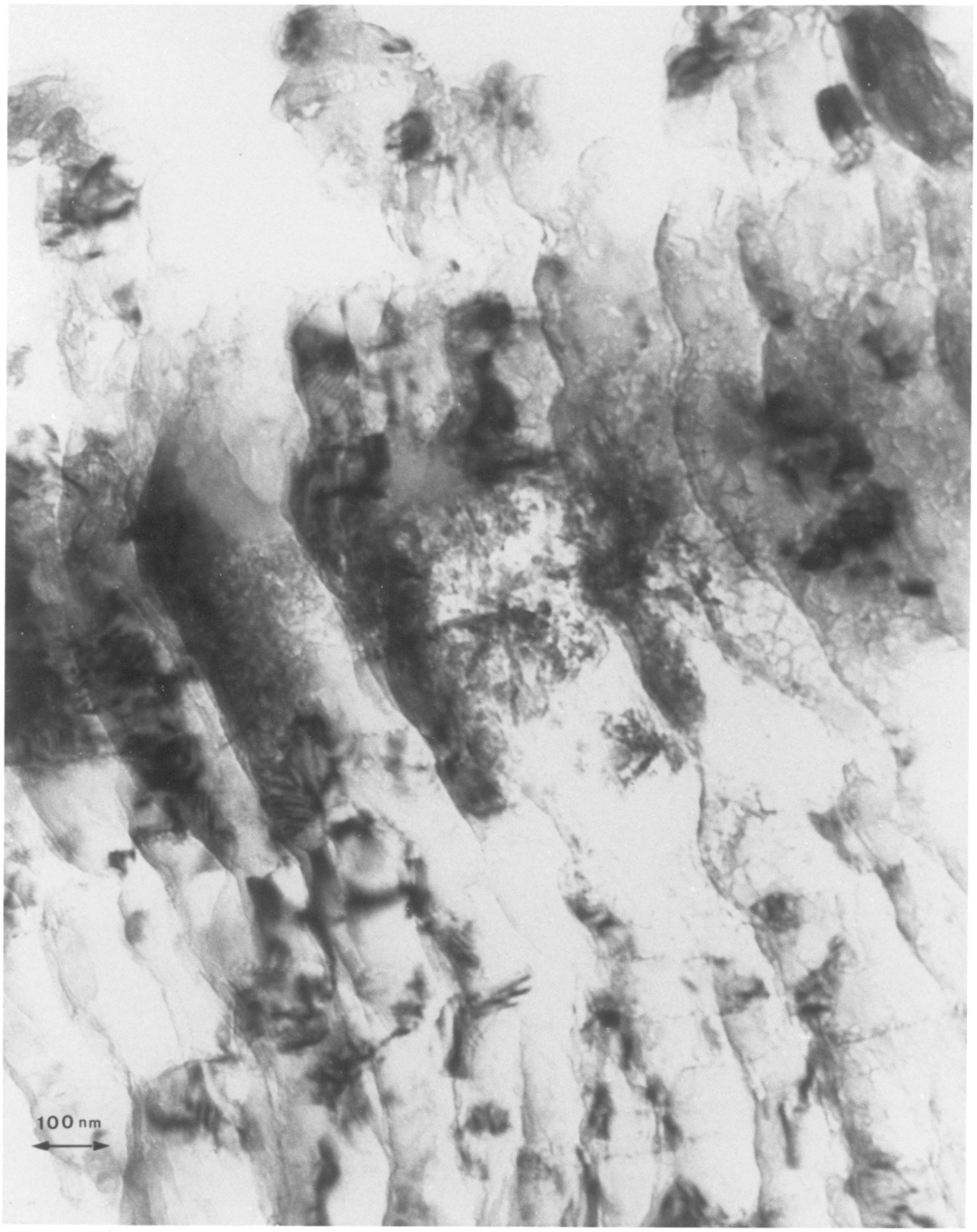

Figure 29. Transmission electron micrograph of ultramicrotomed section cut transversely through PAA Al/Li oxide-polysulfone interface, 100,000 X.

plane of pores during slicing. As the fracture jumped from one plane to another, successive cuts often caused the sections to break up. This TEM photomicrograph at 29,000 X shows the morphology of the columns and a more fine structure on the top which is bonded to the oxide.

The TEM photomicrograph of the cross cut from a bond in Fig. 29 at 100,000 X reveals that the polysulfone had penetrated into the porous oxide when thermally pressed at 290 C. This was confirmed by EDX where the sulfur from polysulfone was detected.

F. Primed Samples

Primers are sometimes applied to the prepared surfaces for the following reasons, i) a coating of primers applied immediately to a freshly prepared surface serves to protect it until the bonding operation is carried out, ii) the primer may function as a corrosion or hydration inhibitor, iii) the primer may be a coupling agent capable of forming chemical bonds with the adherend surface on the one hand and the adhesive on the other. This does not necessary add to bond strength when dry but it prevents displacement of adhesive by water.

Since the SAA pretreatment improved the durability of the Al/Li bond when compared to the FPL etched samples, the SAA samples were primed with 3.0 wt. % polysulfone dissolved in chloroform to observe if priming the sample would further improve the durability. When the sample was primed, the primer could migrate into the holes of the oxide layer until it reaches the barrier layer (180).

1. Wedge Test of SAA Primed Samples

The binding energies and atomic fractions for the primed SAA sample as well as the failure surfaces after wedge test are given in Table 15. For the unbonded SAA primed Al/Li surface, the O 1s photopeaks at 533.2 and 531.9 eV are assigned to polysulfone. The 533.2 eV peak arises from the O=S bond, where the 531.9 eV peak arises from the O-⬡ bond. Also the Al 2p photopeak is not present, the S photopeak is from the polysulfone and the atomic fraction of carbon is high compared to the unprimed samples, indicating a significant concentration of adhesive. The XPS results indicate that priming polysulfone to the SAA treated sample covers the entire surface with polysulfone and no aluminum oxide is exposed on the surface.

On both failure surfaces #1 and #2, the atomic fraction of oxygen is increased when compared to the unbonded but primed surface, indicating that there is some oxide present. Since there are still high atomic fractions of carbon and sulfur present, this indicates that there is substantial amount of polysulfone also present on the surfaces. The failure which occurred was a mixed mode similar to the SAA pretreated samples (see Table 8).

HSEM studies have been done on the failure surfaces and the photomicrographs are given in Fig. 30. The unbonded HSEM photomicrograph could not be taken due to charging of the sample. Failure surface #1 at 150 X magnification (Fig. 30a) indeed shows both the aluminum hydroxide formed and the fractured polymer surfaces. At 25,000 X magnification, the hydroxide can be clearly seen

TABLE 15. XPS analysis of SAA primed and two failed Al/Li surfaces.

Photopeak	SAA Primed		SAA Primed (1)		SAA Primed (2)	
	B.E.(eV)	A.F.	B.E.(eV)	A.F.	B.E.(eV)	A.F.
C 1s	284.6	0.83	284.6	0.71	284.6	0.74
O 1s	533.2	0.13	533.1	0.23	533.1	0.22
	531.9					
Al 2p	----	NSP	75.5	0.03	75.7	0.02
S 2p	167.7	0.03	167.8	0.02	167.7	0.02

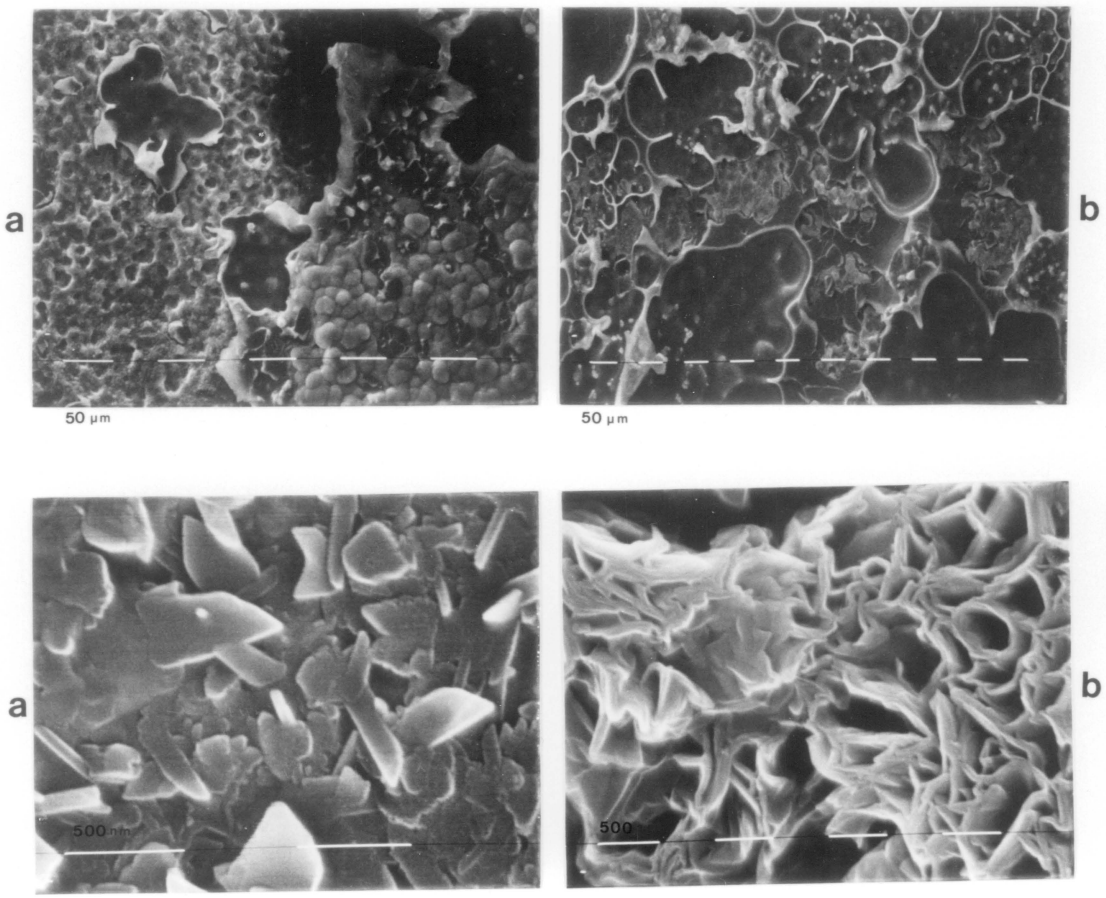

Figure 39. Surfaces of SAA primed samples, a) failure side 1 and b) failure side 2.

with an average size of 400 nm. Failure surface #2 at 200 X magnification shows the same structure as failure surface #1, the 50,000 X magnification photomicrograph shows the flakes that are associated with hydrated oxide.

Therefore, priming the freshly pretreated adherend surfaces for protection prior to bonding may be necessary if the treated surfaces are to be bonded at a later time. However, in this study, since the bond was made immediately following the pretreatment, the priming did not further improve the durability.

2. PAA Aluminum Alkoxide Surfaces Before and After Environmental Exposure

Several different types of compounds have been investigated to increase the durability of bonded joints. Davis et al. (181) chose nitrilotris (methylene) phosphonic acid (NTMP) to apply to FPL etched 2024 aluminum alloy, Boerio et al. (103) characterized the organosilane coupling agent, γ-aminopropyltriethoxysilane (γ-APS) on polished 2024 aluminum alloy mirrors. Pike (182) studied aluminum alkoxide on PAA and FPL etched 2024 aluminum alloy. The latter inhibitor, aluminum alkoxide, when measured by the wedge crack tests, showed a 4 to 10 fold improvement in crack resistance compared to organic primer controls (183). The results were dependent on adhesive type and surface treatment when tested at elevated temperature and high humidity. The same aluminum alkoxide was utilized in the present work as an inorganic primer and is discussed below.

In Table 16, the binding energies and atomic fractions are listed for the PAA aluminum alkoxide primed

TABLE 16. XPS analysis of PAA Al/alkoxide surfaces before and after exposure to 71°C & 100 % R.H. environment.

Photopeak	PAA Al/alk before environmental exposure		PAA Al/alk after environmental exposure	
	B.E(eV)	A.F.	B.E.(eV)	A.F.
C 1s	284.6	0.23	284.6	0.24
O 1s	531.5	0.55	531.7	0.60
Al 2p	74.1	0.22	74.0	0.16
S 2p	----	NSP	----	NSP
P 2p	----	NSP	----	NSP
O/Al		2.49		3.88

sample before and after exposure to the 71 °C and 100 % R.H. environment for 173 hours. The O 1s photopeak assigned to aluminum oxide appears on the PAA aluminum alkoxide sample both before (531.5 eV) and after (531.7 eV) exposure in the hot-humid environment. The Al 2p photopeak is present on both surfaces before (74.1 eV) and after (74.0 eV) environmental exposure. The P 2p photopeak seen on the PAA bare surface without the primer was from phosphoric acid (Table 9). However, after application of 6 coats of the alkoxide on the PAA surface, the phosphorous peak is not present. Also, the phosphorous peak is not present on the PAA aluminum alkoxide sample after exposure to the environment. The reason why the phosphorous peak is not detected is presumably due to the complete covering by the alkoxide of the PAA pretreated surface for the before environmental exposure case. After environmental exposure case, the aluminum hydroxide covers the top surface thus preventing the P peak from being detected by XPS. The atomic fraction of oxygen increased after exposure to the hot-humid environment while the atomic fraction of aluminum decreased after exposure to the environment. This result indicates that some hydration has occurred on PAA aluminum alkoxide pretreated surface when exposed to the hot-humid environment.

HSEM photomicrographs of a PAA aluminum alkoxide sample before environmental exposure are shown in Figures 31a and 31b. The 3,200 X photomicrograph (Fig. 31a) of PAA aluminum alkoxide before environmental exposure shows a surface fully covered by the alkoxide inorganic primer.

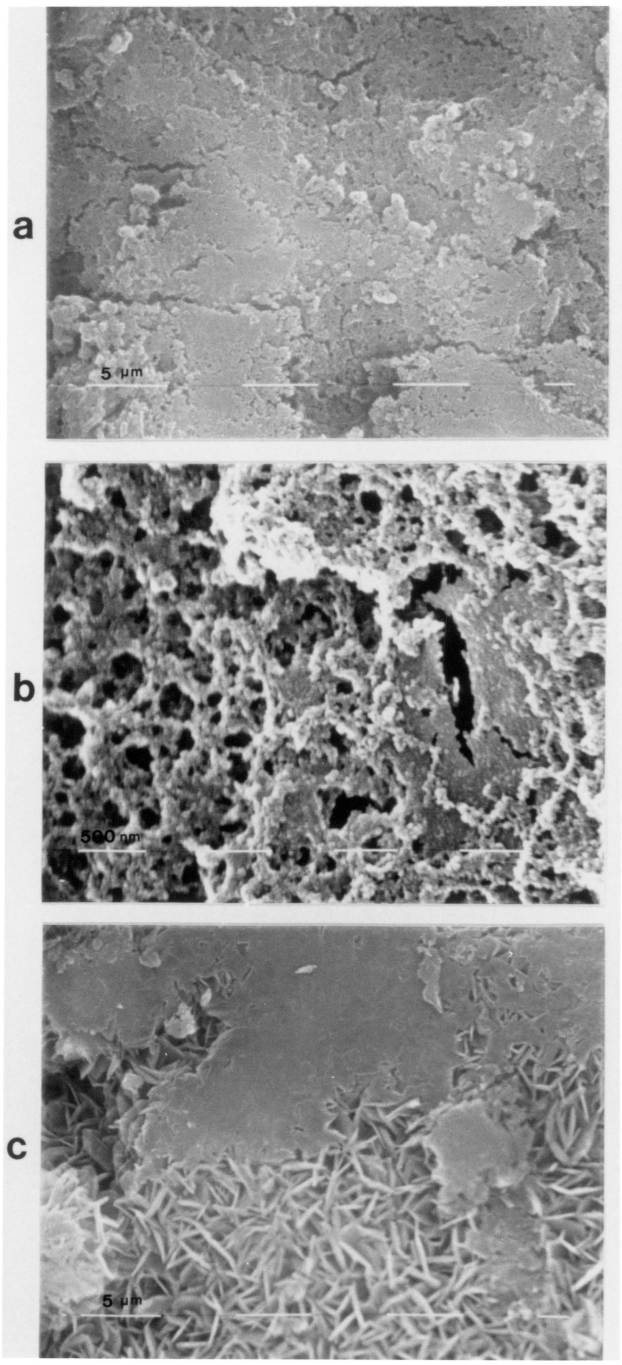

Figure 31. HSEM photomicrographs of PAA aluminum alkoxide primed Al/Li surfaces a) before environment, 3,200 X, b) before environment, 25,000 X, c) after environment, 3,200 X.

No bare aluminum oxide could be seen with the HSEM. The 25,000 X photomicrograph (Fig. 31b) of PAA aluminum alkoxide before environmental exposure is the morphology of the alkoxide primer which shows some loose aggregates of alkoxide on top of the smooth alkoxide surface.

The PAA aluminum alkoxide surface which was exposed to the 71°C and 100 % R.H. environment for 173 hours is shown in Fig. 31c. The HSEM photomicrograph at 3,200 X magnification reveals both an alkoxide surface and a hydroxide surface. Therefore, the alkoxide protected some of the PAA treated surface, but on some spots, the alkoxide did not prevent hydration from occurring. The reason why some areas appear protected and others are not protected is discussed in the next section.

3. PAA Aluminum Alkoxide Primed Wedge Test Samples

The results of the wedge crack opening test of Al/Li joints are given in Figure 13 for the alkoxide primed samples. The PAA aluminum alkoxide primed treatment did not improve bond durability over the PAA treatment. The crack grew to 8 mm after 1/2 hour exposure and then leveled off to 23.3 mm after 24 hours of exposure to the hot and humid environment.

In Table 17, the binding energies and atomic fractions are listed for surfaces #1 and #2 of PAA aluminum alkoxide primed, bonded and then failed samples. For the unbonded PAA aluminum alkoxide surface, the O 1s photopeak assigned to aluminum oxide is at 531.5 eV and Al is at 74.1 eV. No S photopeak is present. On failure surface #1, the atomic fractions of carbon, oxygen and aluminum were virtually unchanged from the PAA aluminum

TABLE 17. XPS analysis of bonded and failed PAA Al/alkoxide primed surfaces.

Photopeak	Failure surface #1		Failure surface #2	
	B.E.(eV)	A.F.	B.E.(eV)	A.F.
C 1s	284.6	0.27	284.6	0.23
O 1s	531.6	0.58	531.7	0.60
Al 2p	74.0	0.15	74.0	0.17
S 2p	----	NSP	----	NSP

alkoxide surface. The binding energies of those elements did not shift. On failure surface #2, again the atomic fractions of carbon, oxygen and aluminum were the same as for the PAA aluminum alkoxide surface and there were no shifts in binding energies for these elements.

As shown, the failure surfaces have identical chemical composition as the PAA aluminum alkoxide before environmental exposure as well as the PAA bare oxide surface. This makes assignment of the failure mode difficult because the failure could occur within the oxide, within the alkoxide or between the oxide/alkoxide interface, and all these failure cases would give the same chemical information by XPS. Therefore by XPS results alone, an unambiguous failure mode assignment could not be made.

In order to make the failure mode assignment, the HSEM photomicrographs shown in Figures 32 (a, b, and c) were used. The unbonded PAA aluminum alkoxide surface which showed a smooth surface with some loose aggregates was shown in Figures 31a and 31b. Failure surface #1 in Fig. 32a at 3,200 X reveals the aluminum hydroxide crystals (500-2000 nm) with a smooth surface on the bottom side of the aluminum hydroxide formation. The smooth aluminum alkoxide inorganic primer is clearly observed in Fig. 32b at 6,400 X magnification. Since the smooth aluminum alkoxide surface is not disturbed by the bonding and the failure process, it can be concluded that the failure occurred within the PAA oxide layer but very close to the aluminum alkoxide primer layer.

Failure surface #2 at 3,200 X in Fig. 32c shows all

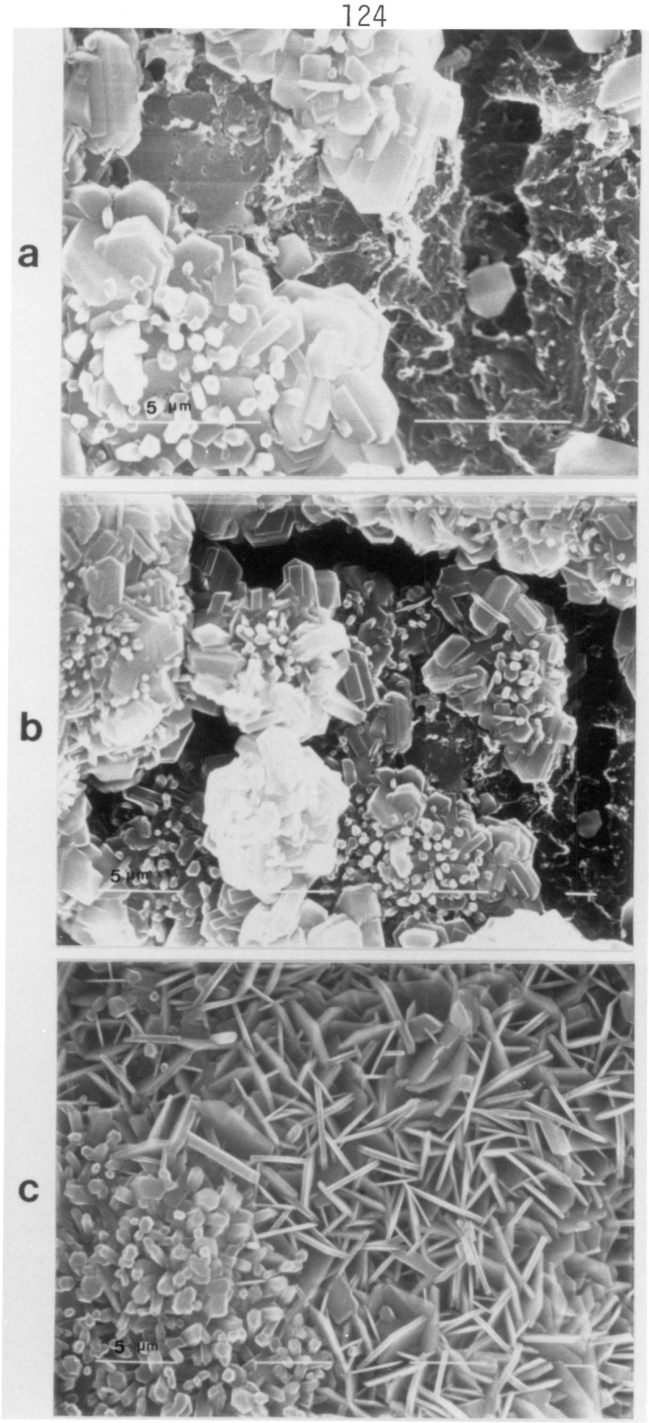

Figure 32. HSEM photomicrographs of PAA aluminum alkoxide primed Al/Li wedge samples a) failure surface #1, 3,200 X, b) failure surface #1, 6,400 X, c) failure surface #2, 3,200 X.

hydration products. The hydroxide flakes show some crystal-like structures and plate-like structures with an average size of about 4 μm.

Therefore, this failure mode was within the aluminum oxide. The oxide layer was covered by the aluminum alkoxide, but in some regions the alkoxide did not prevent hydration. The oxide of Al/Li alloy was found to be five times as thick when compared to other Al alloy oxides (see next section). Therefore more than 6 coats of alkoxide may be needed to cover the thicker oxide layer and prevent hydration.

Another reason why the alkoxide did not improve durability may be due to the fact that the thermoplastic polysulfone may not interact chemically with the primer and therefore not form chemical bonds. This is important because other researchers have reported improved durability with the use of aluminum alkoxide primer to bond aluminum (183), and titanium (171) alloys with epoxy adhesive. They have speculated that the explanation for this increased durability with use of aluminum alkoxide was that metal alkoxide cross-links to the oxide by reacting rapidly with surface hydroxyl groups and thereby leading to polymerization. This primer is in turn chemically reacted to the epoxy adhesive. The exact nature of the interaction between epoxy resin adhesive and the amorphous alumina surface remains to be solved, but the initial results indicated that some type of chemical interaction between adhesive and alkoxide plays a predominant role in total bond performance (182). This conclusion is drawn from the wedge tests of the samples

after the primer was applied. Mechanical interlocking would not be expected to contribute in this case since the alkoxide primed surfaces are smooth (182).

In summary, the aluminum alkoxide did not improve the durability of PAA pretreated Al/Li samples when bonded with the thermoplastic adhesive, polysulfone.

G. Effect of Li on Surface Preparation By PAA (AES Depth Profile)

Kinloch and co-workers (184,185) reported that the presence of magnesium on the surface is detrimental to the durability of adhesively bonded aluminum alloys in moist environments. In order to study a possible similar effect of lithium on the durability of Al/Li alloy, depth profiling was done with AES in which Al, Li and O signals were followed as a function of sputtering time. The peak to peak amplitudes of the Auger electron signals for O, Al and Li are plotted as a function of sputtering time in Figure 33a. Lithium is not surface concentrated as shown by the AES depth profile. XPS results for a degreased Al/Li sample given in Table 18 show the presence of a high concentration of lithium (Li/Al = 0.54). Note that the Li/Al ratio for the bulk alloy is 0.02. However when the alloy is anodized or FPL etched, the lithium signal is not detected by XPS suggesting lithium does not surface migrate once surface pretreatment removes lithium from the surface.

Therefore, the effect of lithium on the durability of the bonded alloy may be minimal. This was proved when a comparison of the bonding of Al 7075 with Al/Li was made

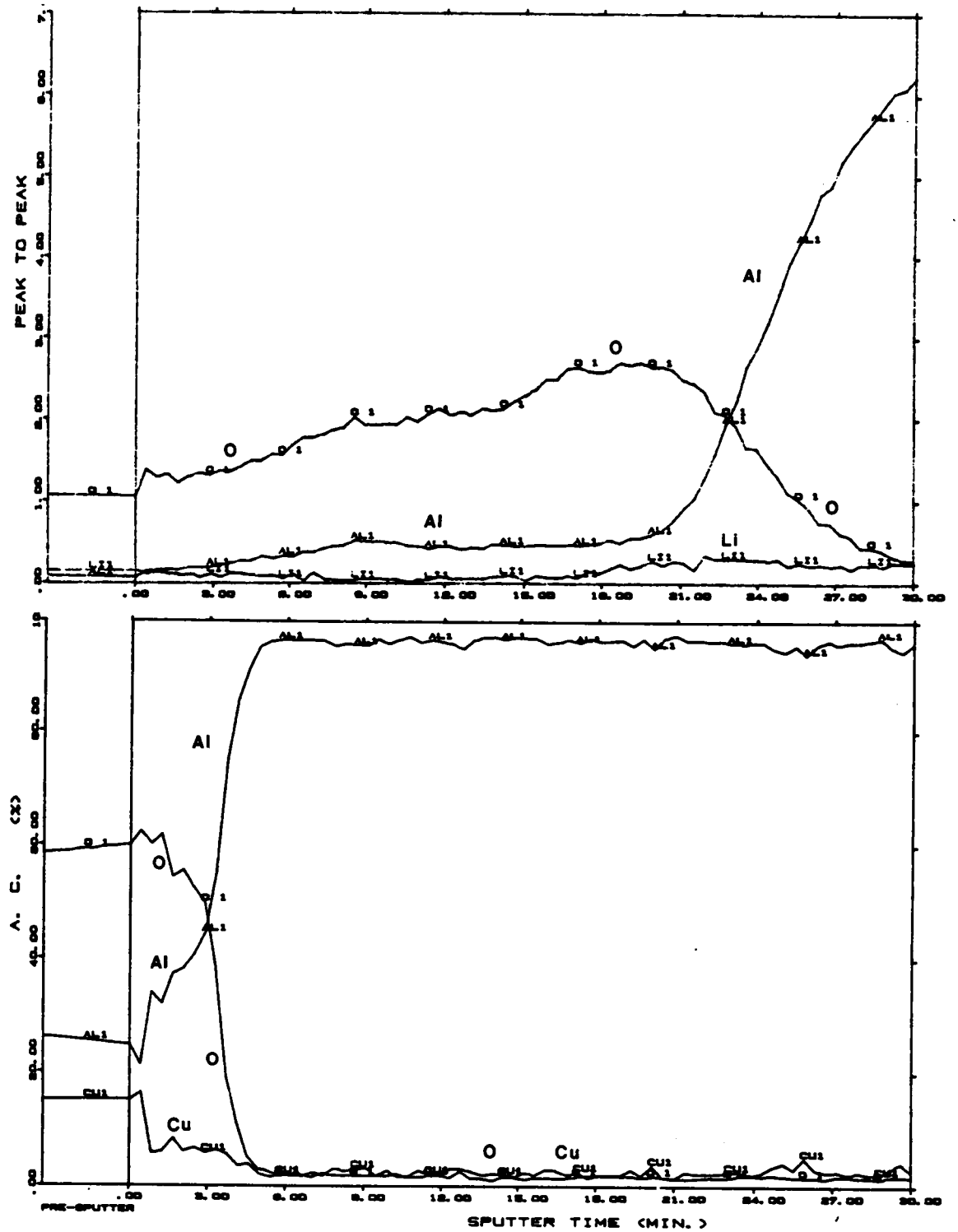

Figure 33. AES depth profile of a) PAA Al/Li sample and b) PAA Al 2024 sample.

TABLE 18. XPS analysis of degreased Al/Li alloy

Photopeak	B.E. (eV)	A.F.
C 1s	284.6	0.29
O 1s	530.9	0.54
Al 2p	74.6	0.11
S 2p	----	NSP
P 2p	----	NSP
Li 1s	55.6	0.06
Li/Al		0.54

using same polysulfone. Similar results were obtained for both adherends. For example, the crack extension results and the analysis of the failure surfaces were similar for Al 7075 (not reported) as for Al/Li for two surface pretreatments (FPL etch and PAA). However, the PAA pretreated Al/Li sample has an oxide layer which takes 23 min to sputter through. In order to compare the oxide thickness of the Al/Li alloy with a 2024 aluminum alloy after a standard PAA pretreatment, depth profiling of Al 2024 alloy was also done. The peak to peak amplitudes of the Auger electron signals for Al, Cu, and O are plotted as a function of sputtering time in Figure 33b. The PAA pretreated Al 2024 sample has an oxide layer which takes 3 min to sputter through. Although direct comparison cannot be made between the two oxide thicknesses because of possible differences in sputtering efficiency (144), the standard PAA treatment of the Al/Li alloy seems to leave a thicker oxide layer than on the Al 2024 alloy. The SEM photomicrograph shown in Figure 34a is for a PAA Al/Li sample which was bent in liquid nitrogen. This method proved useful since the oxide thickness was directly observable without cross-section cuts. The fracture surface oxide average thickness is estimated to be 1.75 um. The SEM photomicrograph shown in Fig. 34b for the PAA Al 2024 shows the oxide thickness to be 0.45 μm. This was the case where both of the above samples were anodized at 6.5 mA/cm^2 volts for 20 minutes in phosphoric acid. This difference in oxide thickness confirms the Auger depth profiling study. The thicker oxide would form the larger hydroxide flakes (400-500 nm) seen on the Al/Li alloy

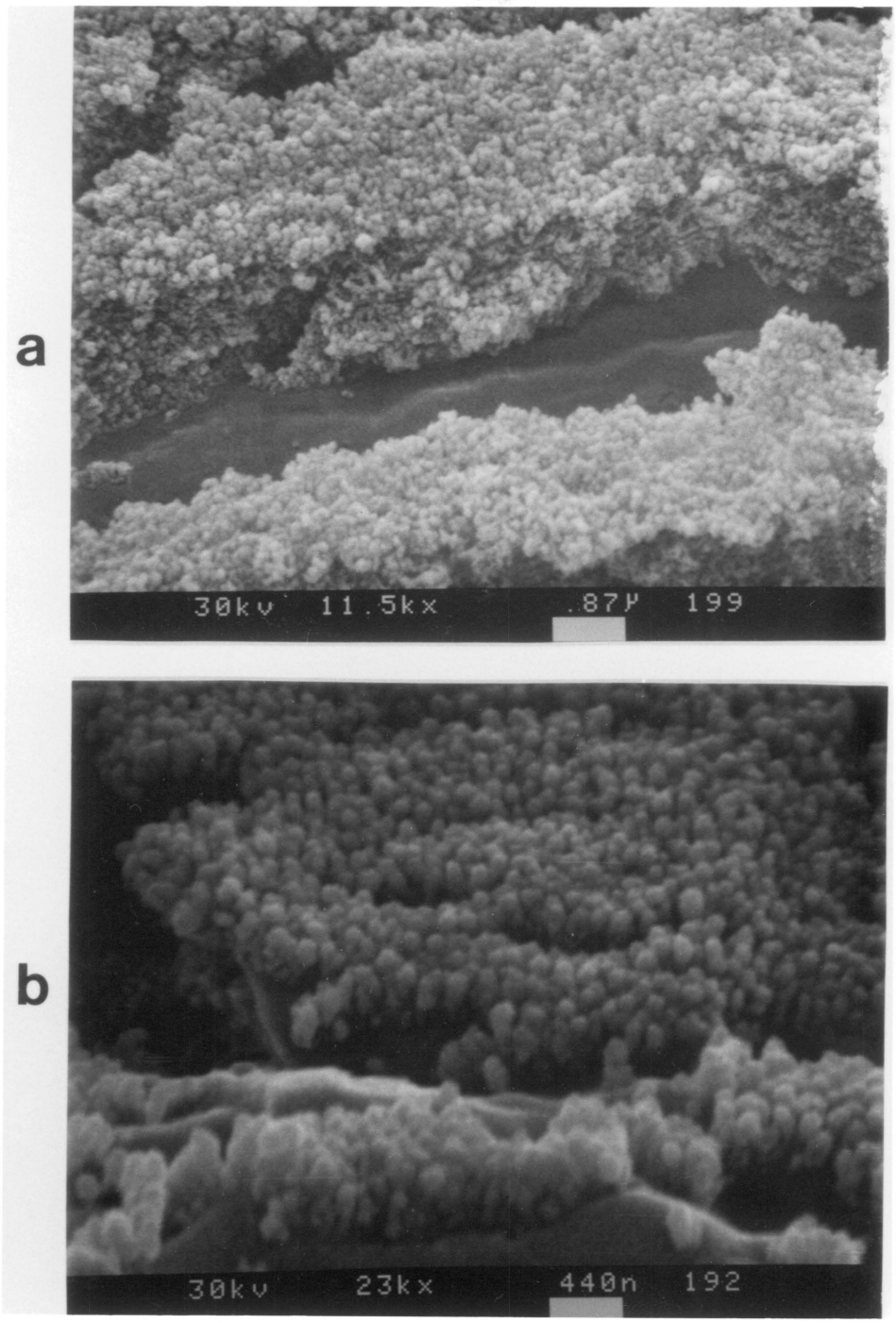

Figure 34. SEM photomicrographs of 20 min PAA a) Al/Li alloy and b) Al 2024 alloy bent in liquid nitrogen.

treated by the PAA process than that reported for the Al 2024 alloy (200 nm) (186).

In regard to oxidation reactions of Al/Li alloys, the oxidation rates of Al/Li alloys are one to two orders of magnitude greater than those of other high strength aluminum alloys in a comparable temperature range (187). Because lithium oxidizes preferentially, oxidation products rich in lithium form, and the metal region near the surface is depleted of the Li (188). This behavior is due to the fact that the oxidation potential of Li, 3.045 V, is the highest of all metals, and its diffusivity is high when compared to other common alloying elements used in aluminum alloys (189). The fact that the metal region near the surface is depleted of lithium after surface pretreatment is consistent with the XPS results which detected no lithium after surface pretreatment.

H. Comparison of Mode I and Mode II Failures

Adhesively bonded joints often fail from the propagation of cracks within the adhesive or at the interface between the adhesive and an adherend. The principles of fracture mechanics have been applied to adhesively bonded structures in recent years, but a number of complications arise on comparison with the fracture of a homogeneous material. The discussion below compares failure surfaces between mode I and mode II failures. The three basic modes of failure are shown in Fig. 35 (131). Since the lap shear test is both mode I and mode II failure, it will be simply referred to as mixed mode failure.

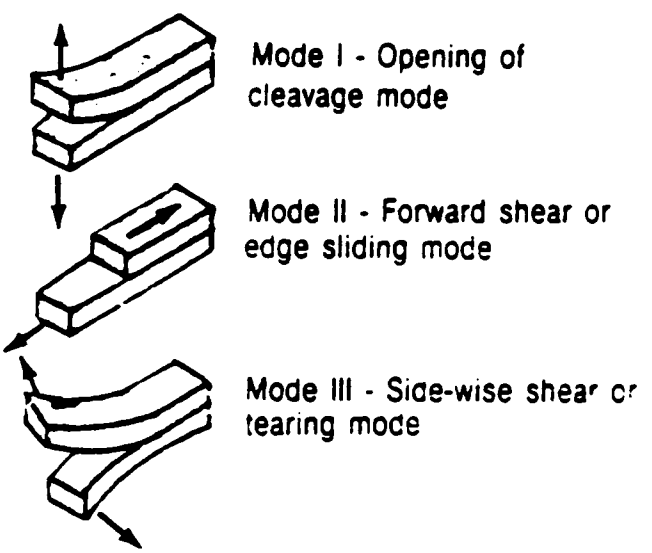

Figure 35. Basic loading modes (131).

The HSEM photomicrographs of the PAA Al/Li using polysulfone bonded sample without environmental exposure pulled in tension (mode I) in Figure 36 for failure surface #1 at 25,000 X and failure surface #2 at 1,600 X magnification show ductile failure where PSF has simply failed cohesively. Also on failure surface #1, one can clearly see the polysulfone adhering to the aluminum oxide. The XPS results confirm that the failure was indeed a cohesive failure and the binding energies and atomic fractions of elements detected are listed in Table 19. The observed peaks are all assigned to polysulfone.

For a lap shear (mixed mode) sample without environmental exposure, failure surfaces show morphologically similar structures to the mode I fracture surfaces as shown in Figure 37. However, there was more tearing of PSF in the shear direction. The XPS results listed in Table 20 are similar to those of in Table 19 for mode I failure.

Most previous work on adhesively bonded joints (190,191) deals with mode I fracture and with negligibly thin adhesive layers. Exceptions are the papers of Anandarajah and Vardy (192) and Mai (193) who considered both mode I and mode II fracture and Chow et al. (194) who considered adhesive layers of finite thickness, but again dealt with mode I only. However, no work has been reported on comparing the surface chemical composition and surface morphology for mode I and mixed mode fracture surfaces. The present study therefore indicates that when the bonded joints are failed before environmental exposure, either in Mode I or mixed mode, the failure

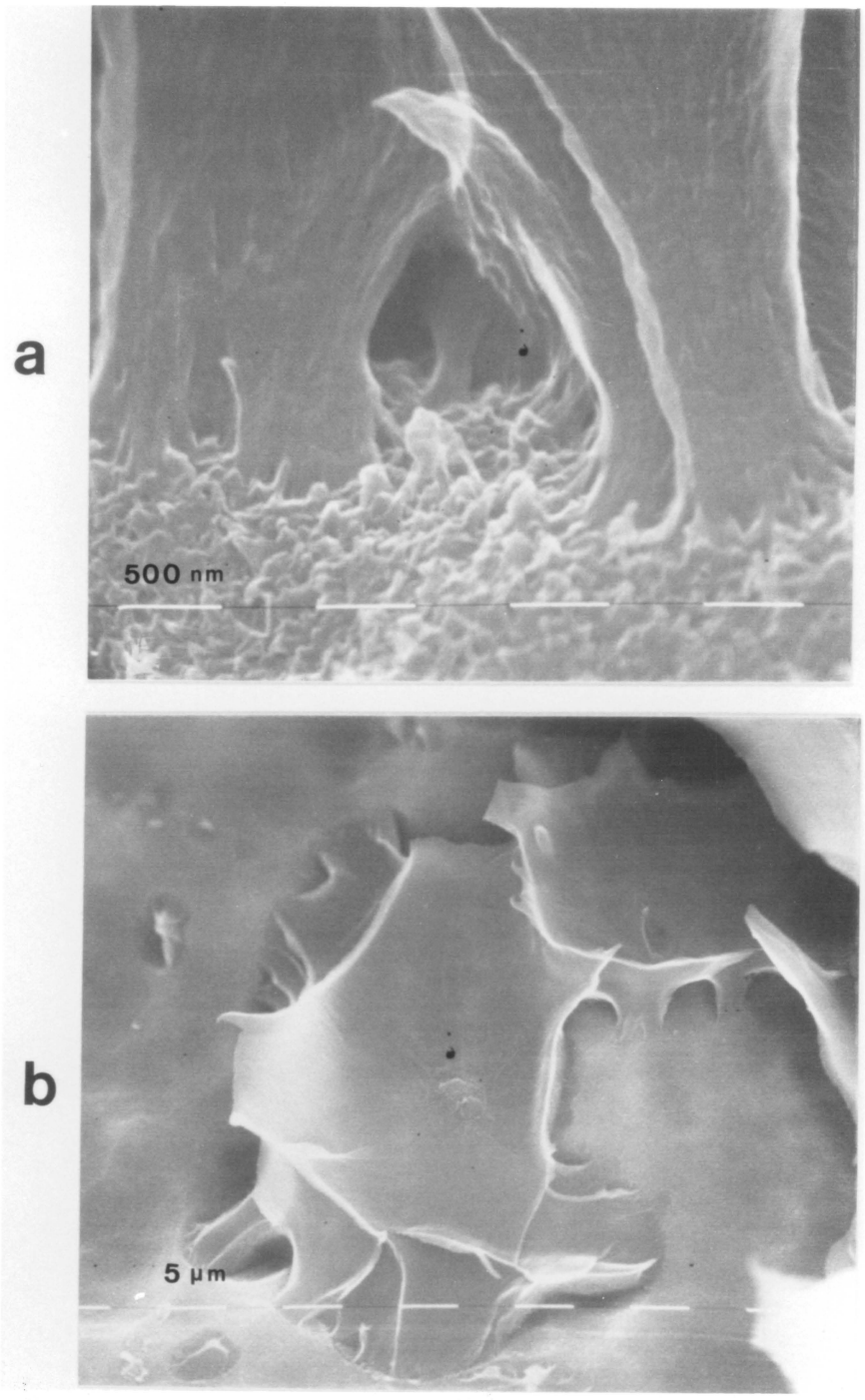

Figure 36. HSEM photomicrographs of PAA wedge before environment a) failure side #1, 25,000 X and b) failure side #2, 1,600 X.

TABLE 19. XPS analysis of PAA mode I failure surfaces before environmental exposure.

	PAA mode I failed before env. side #1		PAA mode I failed before env. side #2	
Photopeak	B.E.(eV)	A.F.	B.E.(eV)	A.F.
C 1s	284.6	0.81	284.6	0.78
O 1s	532.5	0.16	532.6	0.18
	531.1		531.0	
Al 2p	----	NSP	----	NSP
S 2p	168.0	0.03	168.1	0.03
P 2p	----	NSP	----	NSP

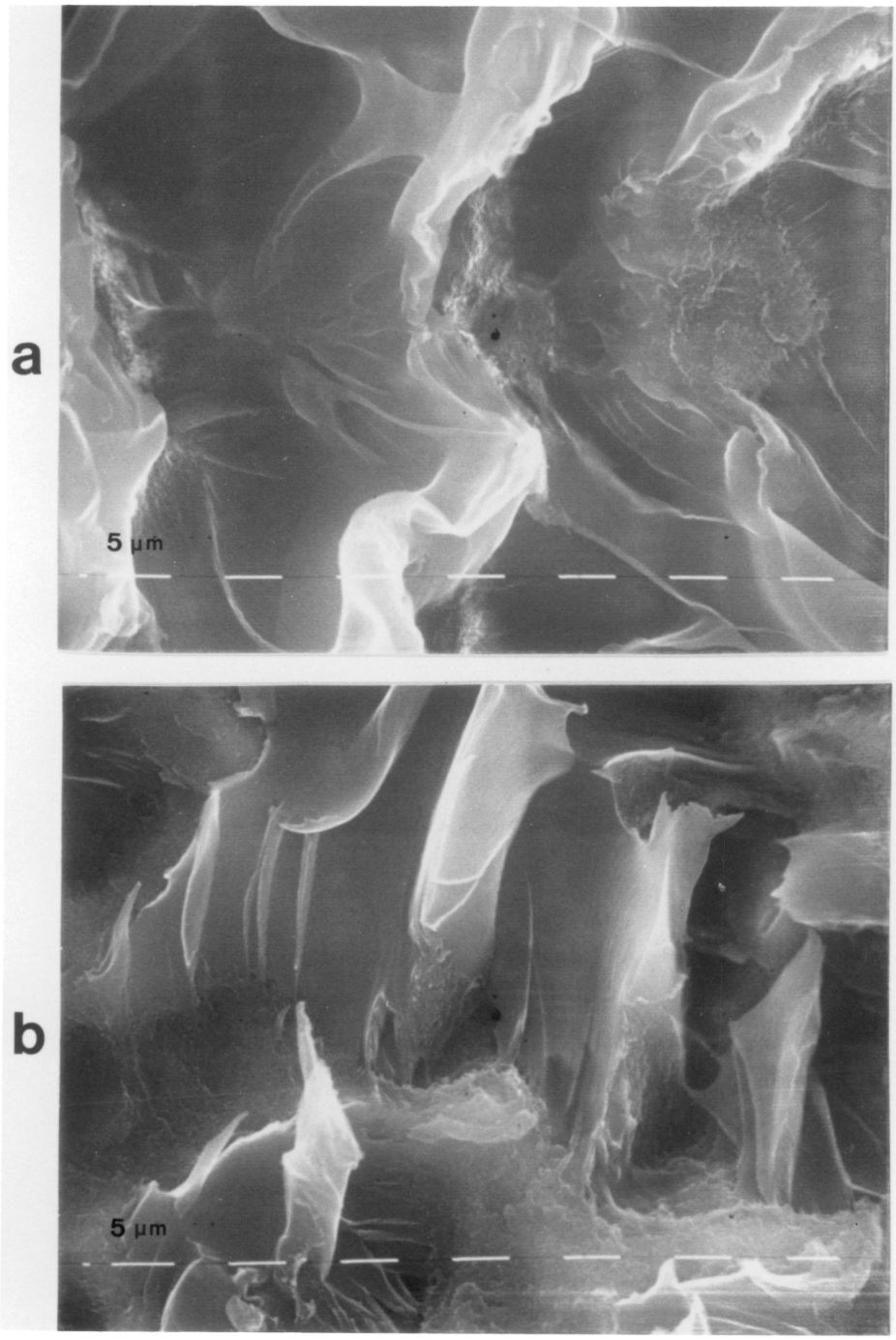

Figure 37. HSEM photomicrographs of PAA lap shear sample before environmental exposure a) failure side #1, 1,600 X and b) failure side #2, 1,600 X.

TABLE 20. XPS analysis of PAA mixed mode (I and II) failure surfaces before environmental exposure.

	PAA mixed mode failed before env. side #1		PAA mixed mode failed before env. side #2	
Photopeak	B.E.(eV)	A.F.	B.E.(eV)	A.F.
C 1s	284.6	0.82	284.6	0.83
O 1s	532.3	0.14	532.4	0.13
	531.2		531.1	
Al 2p	----	NSP	----	NSP
S 2p	168.0	0.04	168.0	0.04
P 2p	----	NSP	----	NSP

surfaces show no differences either in chemical composition or morphological structures.

I. Cyclic Loaded Samples

The majority of testing of adhesively bonded samples has been confined to static load but by including dynamic load, the stressed durability testing provides significant additional information on the performances of aircraft structures and highway bridges, which undergo dynamic loading during usage. The cyclic loaded samples were studied in the present work and the results are discussed below.

In Table 21, the binding energies and atomic fractions are listed for failure surfaces #1 and #2 for cyclic loaded sample. On failure surface #1, the atomic fraction of carbon is moderately high, the S 2p peak from PSF is at a binding energy of 167.7 eV, the O 1s peak is at 532.5 eV and the Al 2p peak is at 74.8 eV. On failure surface #2, again the atomic fraction of carbon is moderately high and the binding energies for the S, O and Al photopeaks were the same as for failure surface #1. The presence of the sulfur peak and the relatively high content of carbon indicate that there is polysulfone present on both surfaces, but since there was an Al photopeak present on both fracture surfaces, the crack diverged into the oxide. Therefore, mixed mode failure had occurred.

The HSEM photomicrographs shown in Fig. 38 clearly supports the mixed mode failure assignment. The failure surface #1 in Fig. 38a at 12,500 X reveals the mixed mode

TABLE 21. XPS analysis of PAA Al/Li cyclic loaded wedge sample.

	PAA Al/Li cyclic loaded wedge side #1		PAA Al/Li cyclic loaded wedge side #2	
Photopeak	B.E.(eV)	A.F.	B.E.(eV)	A.F.
C 1s	284.6	0.53	284.6	0.66
O 1s	532.5	0.37	532.6	0.20
Al 2p	74.8	0.08	74.8	0.12
S 2p	167.7	0.02	167.8	0.02
P 2p	----	NSP	----	NSP

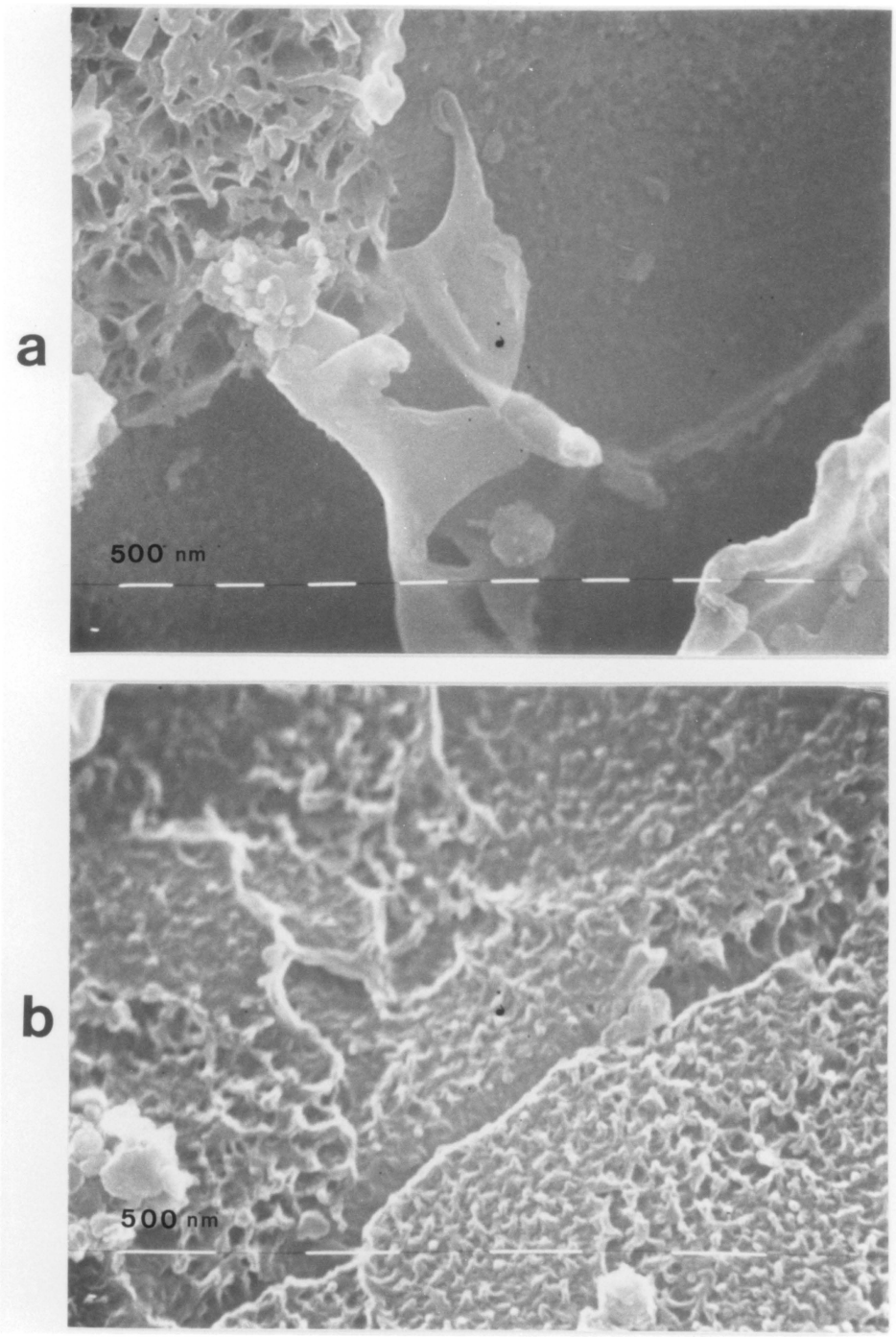

Figure 30. HSEM photomicrographs of cyclic loaded PAA Al/Li thick adherend sample a) failure side #1, 12,500 X and b) failure side #2, 25,000 X.

failure with some patches of PSF seen and also some bare aluminum oxide surface. Failure surface #2 in Fig. 38b at 25,000 X shows the polymer structure which was pulled out of the PAA oxide layer, but in other regions there was ductile failure of PSF. Therefore, the HSEM micrographs confirm the XPS results that mixed mode fracture occurred.

The two failure surface structures were representative of the whole sample, indicating clear mixed mode failure and these morphological results are in qualitative agreement with the XPS results reported above.

The displacement at the tip of the cyclic loaded sample was 1.5 mm whereas the static loaded sample displacement was 3.0 mm. That is, there was less load at the tip of the crack on the cyclic loaded sample. Thus for the cyclic loaded samples, even with less load at the crack tip, not only did the crack propagate faster but the mode of fracture shifted to mixed mode failure from cohesive failure in the static loaded samples. These findings agree with those of Mays and Tilly (195), who reported that for all fatigue failures, the failure mode changed to interfacial from mixed mode failure for steel-epoxy bonds, but who also pointed out that the failure mode shifted as a function of testing temperature. Marceau et al. (196) also performed cyclic stress testing of aluminum-epoxy system and reported that the cyclic loading produces fracture much faster than does static loading. Therefore, as expected, the cyclic loading is more damaging than the static loading in 71 $^{\circ}$C and 100 % R.H. environment.

J. Infrared Spectroscopy Studies

1. Polished Al/Li Samples

In order to study the interaction between the polysulfone and the Al/Li adherend surface, polished Al/Li samples with a spin cast sample of polysulfone were probed using specular reflectance FTIR in combination with ellipsometry. The FTIR spectrum (1700-800 cm^{-1}) of a 7-10 nm thick polysulfone spin cast on polished Al/Li surface is shown in Fig. 39. Table 22 lists various spectral assignments (197,198). The cast film thickness was too thick for orientation studies of molecules and the film was not uniform enough to warrant further analysis.

In the above work, 0.125 % polysulfone was spin cast onto polished Al/Li mirror in order to utilize specular reflectance FTIR which requires a mirror finish surface. However, this polished mirror surface is not the actual surface on which the polysulfone will interact in an adhesively bonded joint. The DRIFT technique also does not require a mirror finish surface. Therefore using the DRIFT technique, polysulfone can be studied in contact with the actual surface used for bonding such as FPL etched or PAA pretreated surfaces.

In the present investigation, in order to characterize the interaction between the polysulfone and the Al/Li oxide layer, PAA Al/Li samples before and after environmental exposure, and PAA Al/Li samples spin coated with 3 % as well as 0.125 % polysulfone solution were analyzed by the DRIFT technique.

2. PAA Samples

The IR spectrum of the PAA bare surface in Figure 40a

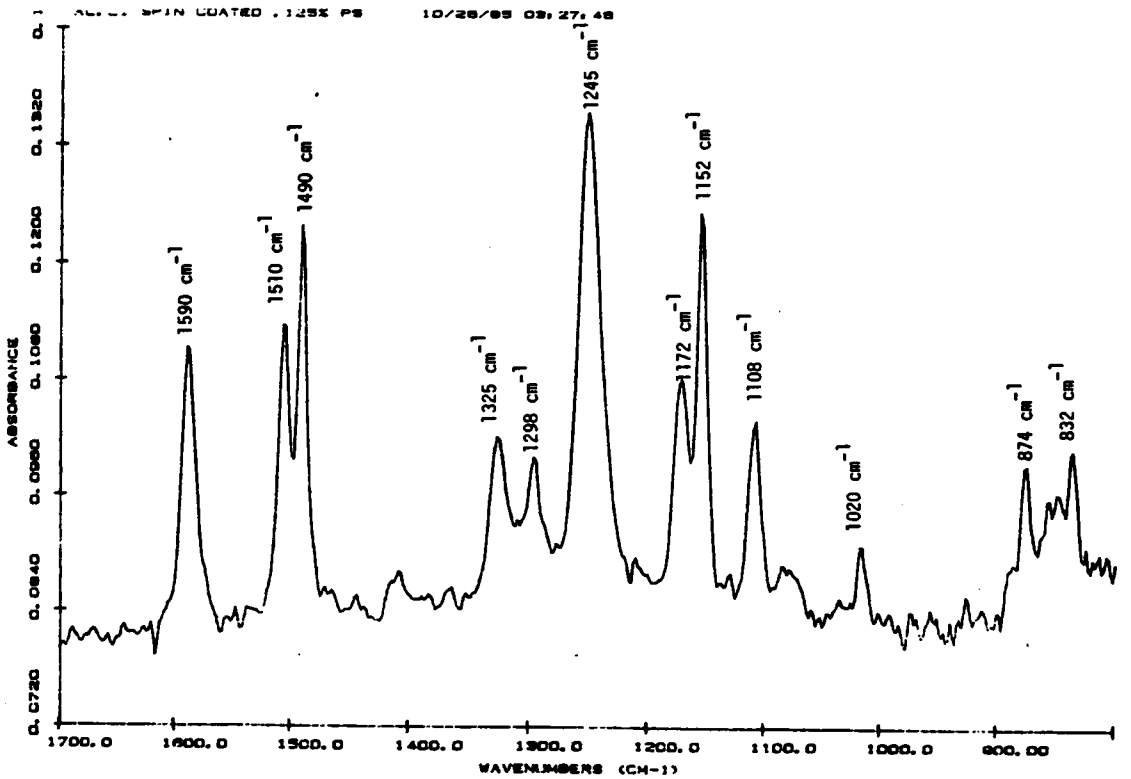

Figure 39. Specular reflectance FTIR spectrum of polysulfone spin cast on polished Al/Li surface.

TABLE 22. Polysulfone FT-IR spectra peak assignment (164).

Wave Numbers (cm^{-1})	Peak Assignment
3300	C-H stretching vibration
3000	Aromatic C-H stretching vibration
1590,1510,1490	Aromatic C=C stretching vibration
1412	Asymmetric C-H bending deformation of CH_3
1393,1368	Symmetric C-H bending deformation of CH_3 group
1325,1298	Doublet resulting from asymmetric O=S=O stretching of sulfone group
1245	Asymmetric C-O-C stretching of aryl ether
1172,1152	Asymmetric O=S=O stretching vibration
1108,1092	Aromatic ring vibrations
1020	Symmetric O=S=O stretching vibration
874,850	Out of plane C-H deformation of isolated hydrogen in 1,2,4 substituted phenyl ring
832	Out of plane C-H deformation characteristic of p-substituted phenyl
700-560	C-S stretching vibrations

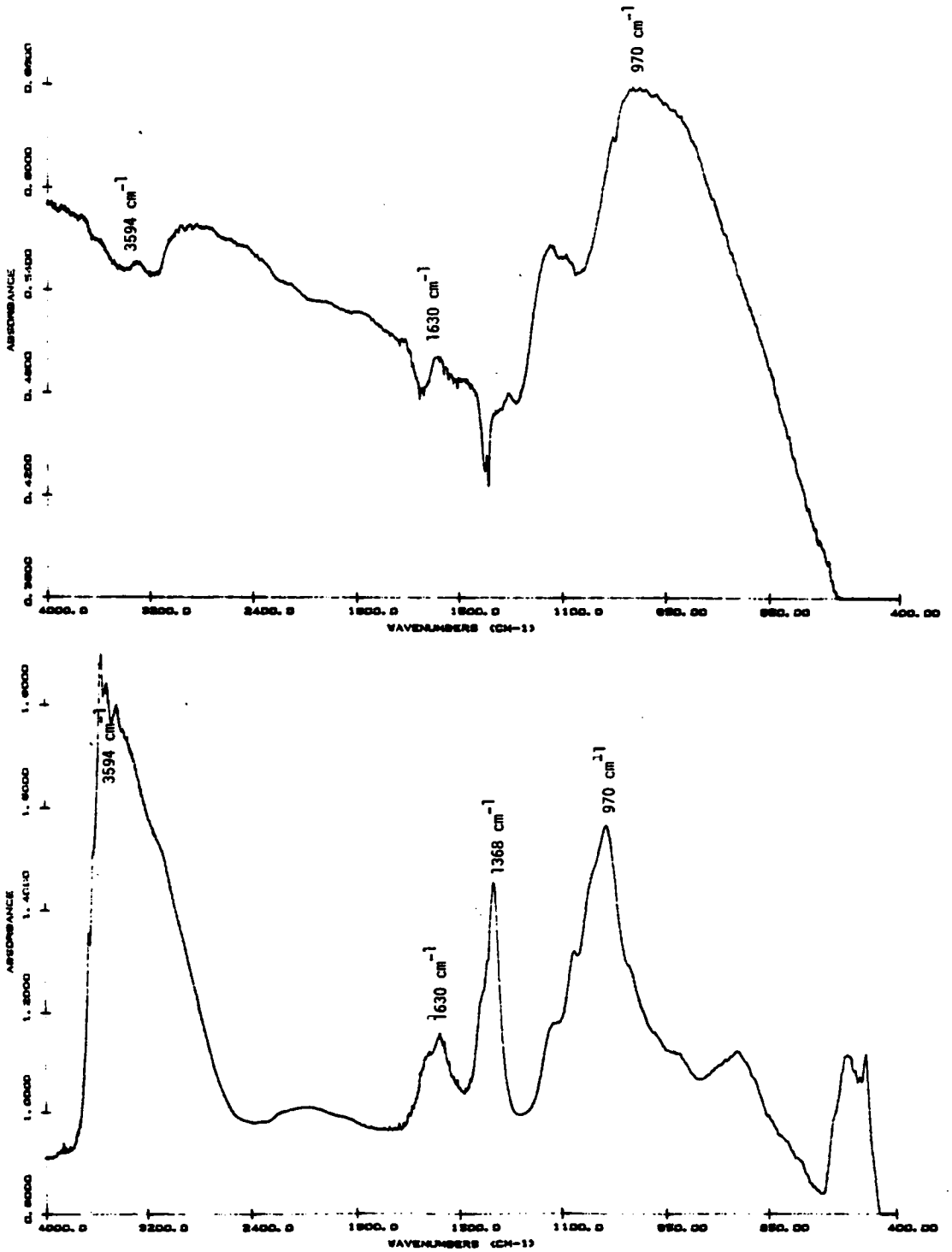

Figure 40. DRIFT spectra of PAA Al/Li bare surface, a) before environmental exposure and b) after 71 C & 100 % R.H. environment.

shows a very low content of water (1630 cm^{-1}) and no defined hydroxyl bands are observed at around 3594 cm^{-1}. The aluminum oxide peak at 970 cm^{-1} is detected and is identified as an amorphous Al_2O_3. Therefore the major component of the PAA surface is aluminum oxide with virtually no surface hydroxyl concentration. The PAA sample which was exposed to the hot-humid environment in Fig. 40b shows a high concentration of hydroxyl groups (3594 cm^{-1}) which are associated with aluminum hydroxide. Although a lesser amount, the aluminum oxide peak at 970 cm^{-1} is also detected.

3. PAA Spin Coated With 3.0 wt. % Polysulfone

Figure 41 shows the IR spectrum after subtraction of the PAA bare oxide layer. The IR spectra of 3 wt. % polysulfone film on PAA shows peaks at 1245 cm^{-1} characteristic of the C-O-C stretching of the aryl ether group. Also, doublets in the region of 1298-1325 cm^{-1} resulting from asymmetric O=S=O stretching were observed. Aromatic ring vibrations at 1020 cm^{-1} were consistent with para substituted products. The spectrum is very similar to spectrum of the spin cast polysulfone on polished Al/Li samples (see Fig. 39) and also similar to a neat polysulfone film (166). This indicates that either there is no chemical interaction taking place between the polysulfone and aluminum or that the polysulfone coating is too thick for the PSF-Al interaction to be observed by DRIFT. A thinner coating was prepared and the results are discussed below.

4. PAA Spin Coated With 0.125 wt % Polysulfone

Figure 41b shows the IR spectrum of PAA Al/Li with a

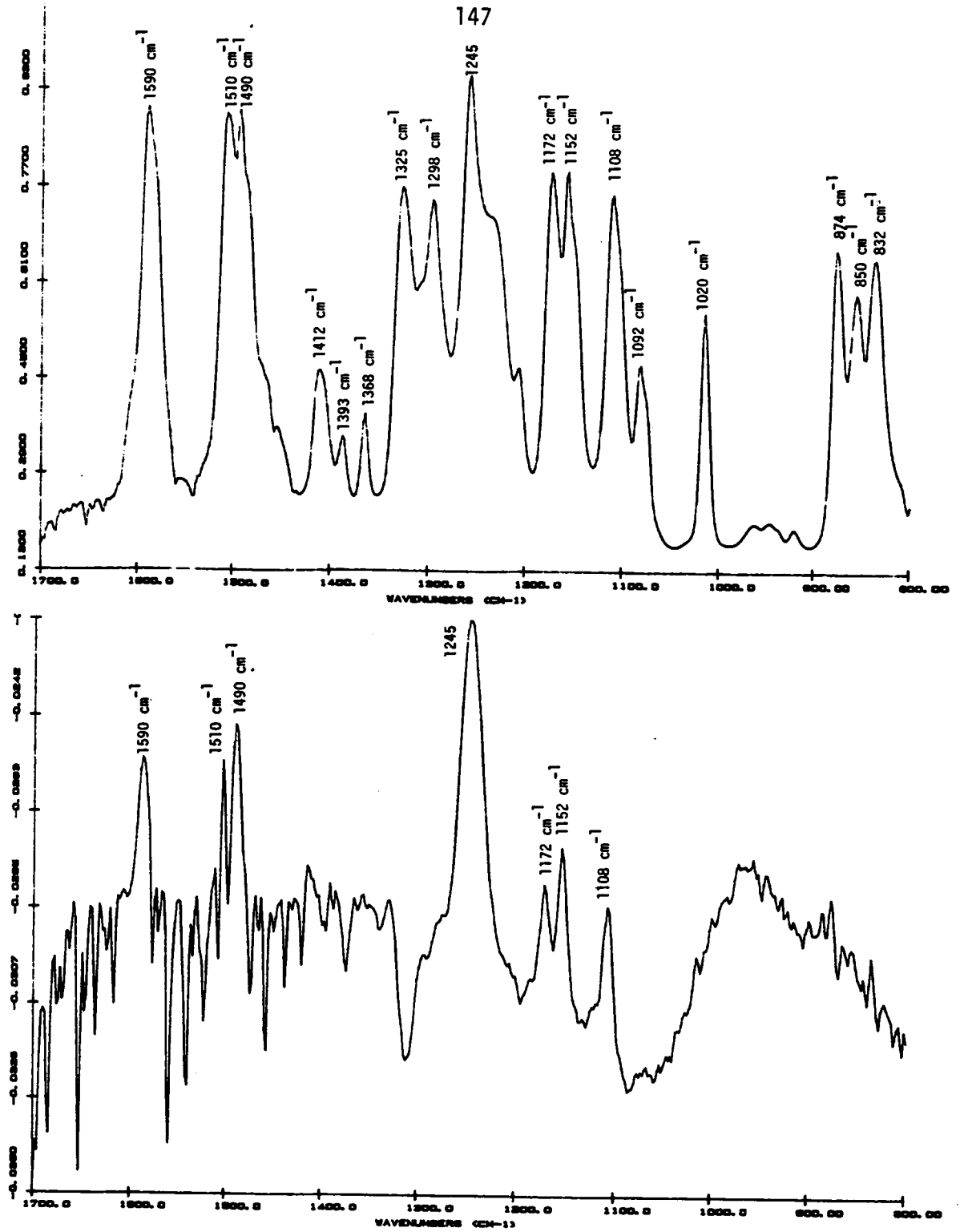

Figure 41. DRIFT spectra of PAA Al/Li surface, a) coated with 3.0 wt. % polysulfone and b) spin coated with 0.125 wt. % polysulfone.

0.125 % polysulfone spin cast coating. When the same 0.125 % polysulfone solution was spin coated on a polished Al/Li sample, the thickness of polysulfone film measured by ellipsometry was in the range of 7-12 nm.

Similar to the 3 % PSF on PAA samples, peaks at 1245 cm^{-1} characteristic of C-O-C stretching of the aryl ether group and at 1172 cm^{-1} characteristic of asymmetric O=S=O stretching were observed. However, unlike the 3.0 % PSF on PAA sample which is considerably thicker (1-2 um) than the 0.125 % PSF spin coated sample, the asymmetric O=S=O stretching in the region of 1298-1325 cm^{-1}, the symmetric O=S=O stretching of 1020 cm^{-1} and C-H deformation in the 874, 832 cm^{-1} region was not detected. This is due to a very thin PSF film which decreases the measured signal (152).

This same 0.125 % polysulfone spin cast on a PAA sample was probed in XPS for elemental analysis, and the binding energies and atomic fractions are listed in Table 23. The O 1s photopeak assigned to the aluminum oxide at 531.3 eV is present. The Al 2p photopeak is present at 74.3 eV. Furthermore, the P 2p photopeak at 134.0 eV on this surface is from residual phosphoric acid used in the anodizing bath. However, the sulfur peak expected at 167.7 eV indicating the presence of polysulfone is not detected by XPS.

XPS analysis of 0.125 % PSF spin coated onto a polished mirror finish surface listed in Table 24 shows a high sulfur (2.9%) and a low Al (1.1%) concentration. This XPS result confirms complete coverage of PSF on a polished Al/Li surface.

TABLE 23. XPS analysis of a 0.125 wt. % polysulfone spin cast on PAA Al/Li.

Photopeak	B.E. (eV)	A.F.
C 1s	284.6	0.17
O 1s	531.3	0.55
Al 2p	74.3	0.26
S 2p	----	NSP
P 2p	134.0	0.02

TABLE 24. XPS analysis of a 0.125 wt. % polysulfone spin cast on mirror finish Al/Li surface.

Photopeak	B.E. (eV)	A.F.
C 1s	284.6	0.82
O 1s	533.0	0.14
	531.6	
Al 2p	73.9	0.01
S 2p	167.7	0.03
P 2p	----	NSP

Using DRIFT, the 0.125 wt. % polysulfone film on the PAA Al/Li pretreated surface was detected by the O=S=O asymmetric stretching at 1152-1172 cm^{-1} region (see Fig. 41b). The reason why IR can detect O=S=O asymmetric stretching and why XPS did not detect any sulfur peak may be due to the fact that at very low concentration of polysulfone applied to the porous surface, the polymeric molecules may be concentrated at the bottom of the pores. When the X-rays bombard the surface, those electrons which are photo-ejected mainly originate from the top of the pores and not from the bottom of the pores and therefore the polysulfone is not detected by the XPS. DRIFT which is less surface sensitive technique than XPS, i.e, DRIFT has a greater sampling depth, can detect the presence of polysulfone.

Therefore using DRIFT, no evidence was found that polysulfone interacts to form a chemical bond with PAA Al/Li. This finding is what was expected and therefore supports the previous discussions where no chemical interaction between PSF-Al/Li oxide was assumed.

CONCLUSIONS

The goal of this study was to correlate the results of wedge tests (measured at 71 °C and 100 % R.H.) of FPL etched as well as anodized surfaces before and after exposure to a hot-humid environment, with the chemical composition and the morphological features of the oxide layer on Al/Li alloy. From this investigation, the following highlights were noted.

1. Lap shear strengths of PAA and SAA pretreated Al/Li samples were slightly greater than those of FPL-etched samples.
2. Wedge test performance on PAA and SAA adherends was superior to that for the FPL etched adherends.
3. The failure path observed with the FPL pretreated samples was at the adhesive/oxide interface.
4. The locus of failure for the PAA and SAA was within the adhesive but the crack occasionally diverged into the oxide.
5. When polysulfone is thermally pressed or primed onto the microporous surface, the polysulfone indeed penetrated into the porous oxide and may have provided a mechanical means of adhesion.
6. The porous structure of anodic oxides on Al/Li formed in both sulfuric acid and phosphoric acid was shown to undergo dramatic changes in morphology after short term (< 90 hrs) exposure to 71°C and 100 % R.H.
7. The morphologically different hydroxides had the same chemical composition when probed by energy dispersive analysis of x-rays. The difference in morphologies was

not due to the metal sulfates but may have been due to differences in crystallinity.

8. AES depth profiling showed that Li is not surface concentrated and therefore the effect of Li on bond durability may be minimal. The oxide on Al/Li alloy was thicker than on Al 2024 alloy when the PAA pretreatment was used.

9. When the bonded joints are failed before environmental exposure either in mode I or mixed mode, the fracture surfaces show no difference in chemical composition or morphological structure.

10. For the cyclic loaded samples, the mode of failure has shifted to mixed mode failure from cohesive failure in the static loaded samples.

11. The failure path for the FPL etched and PAA was both cohesive failure when the wedge test was done at 71°C and 0 % R.H.

12. The DRIFT technique gave no evidence for chemical interaction of polysulfone with the PAA Al/Li oxide layer.

CHAPTER IV

EXPERIMENTAL ANALYSIS OF THIN FILMS FOR MOISTURE INTRUSION INTO THE Al/Li-POLYSULFONE INTERFACE

It has been demonstrated convincingly in CHAPTER III that the Al/Li-polysulfone bond is subject to reduced durability in a hot-moist environment.

Since a surface aluminum oxide changes to aluminum hydroxide upon exposure to a high temperature and high humidity environment (6,65), one can study the mechanism of moisture intrusion into the bondline by following this conversion process. It was mentioned previously in the LITERATURE REVIEW section that moisture intrusion into a bondline can occur, either by diffusion through the adhesive or transport along the oxide-adhesive interface. The mode of moisture intrusion into the bondline was of interest in this work and the oxide to hydroxide transformation is used as an indicator for moisture intrusion into the aluminum oxide-polymer interface. This is the first report of using the surface transformation of aluminum oxide to track moisture intrusion.

EXPERIMENTAL

A. PSF Coating-Solvent Cast on PAA Al/Li

Small quantities of 0.125, 3, and 10 wt % solution of PSF in chloroform were solvent cast on PAA Al/Li samples. This procedure gives a varying thickness of PSF on the phosphoric acid anodized Al/Li oxide surface. The samples were placed in a hot-moist (71 °C and 100 % R.H.) environment for 115 hours. After environmental exposure, the samples were placed in chloroform for 4 hours to remove the PSF. HSEM photomicrographs were taken of the underlying oxide surface. While this method was useful in placing varying thicknesses of PSF on the anodized Al/Li surface, the method described below gave a more uniform PSF thickness.

B. PSF Coating-Spin Cast on PAA Al/Li

In spin casting thin polymer films, the PAA Al/Li samples were secured to a custom made spinning platform (see Fig. 10) by means of double stick tape. The PAA Al/Li substrates were flooded with polymer solutions of known concentration (0.125 % PSF and 0.3 % PSF) and spun at an average speed of 1500-1600 rpm for five seconds. This method of sample preparation gives the same thickness of PSF at the edge and at the center of the sample. A much thinner coat is obtained by spin casting than is possible with thermally pressed film.

The samples were placed in a hot-moist environment for 15 hours. After environmental exposure, the samples were placed in chloroform for 4 hours to remove the PSF

film and the underlying oxide was examined by HSEM.

C. PSF Coating-Thermally Pressed on PAA Al/Li

PAA samples were thermally pressed with neat PSF film using 0.305, 0.076, and 0.038 mm (0.012", 0.003", and 0.0015") thick spacers. This method of sample preparation gives the same thickness of PSF at the edge and the center of sample. The samples were placed in a hot-moist environment for 96 hours. After environmental exposure, the samples were placed in chloroform for 4 hours to remove the PSF and the underlying oxide surface was examined by HSEM.

RESULTS AND DISCUSSION

A. Effect of Chloroform on PAA Al/Li

HSEM photomicrographs in Figure 42 for PAA Al/Li sample before (Fig. 42a) and after placing in chloroform (Fig. 42b) show no physical change of the oxide due to chloroform exposure. Also, a PAA Al/Li freshly pretreated surface was compared to a sample of PAA Al/Li which was exposed to room temperature environment for 120 hours. No physical change of the oxide is observed during room temperature environment exposure.

B. XPS Results of PSF Coating-Solvent Cast on PAA Al/Li

The XPS results for PAA pretreated Al/Li which were exposed in 71°C and 100 % R.H. environment for 115 hours, followed by solvent removal of PSF are shown in Table 25. The results are equivalent for the two concentrations in that both show low atomic concentration of sulfur indicating that most of the PSF is dissolved away. Also no Cl peak is detected indicating no residual solvent is on the surface. The HSEM photomicrograph shown in Figure 43a for the 0.125 % PSF sample is representative of both the edge and center of the sample, and shows hydration products. The HSEM photomicrograph in Figure 43b for 10 % PSF taken from the edge shows more signs of hydration than from the center (Figure 43c). However, when the 10 % PSF drop was initially placed on the PAA Al/Li surface, the edge and center thickness may differ, and one could erroneously interpret the difference in oxide transformation shown in Figs. 43b and 43c to be wicking of

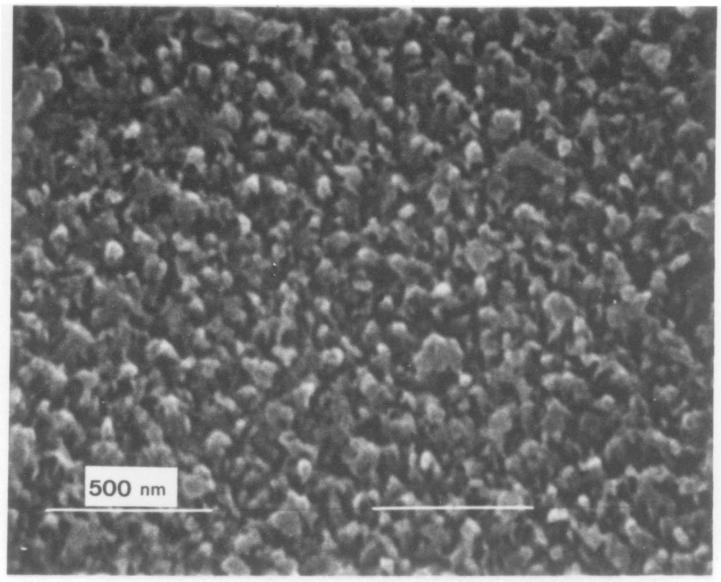

a

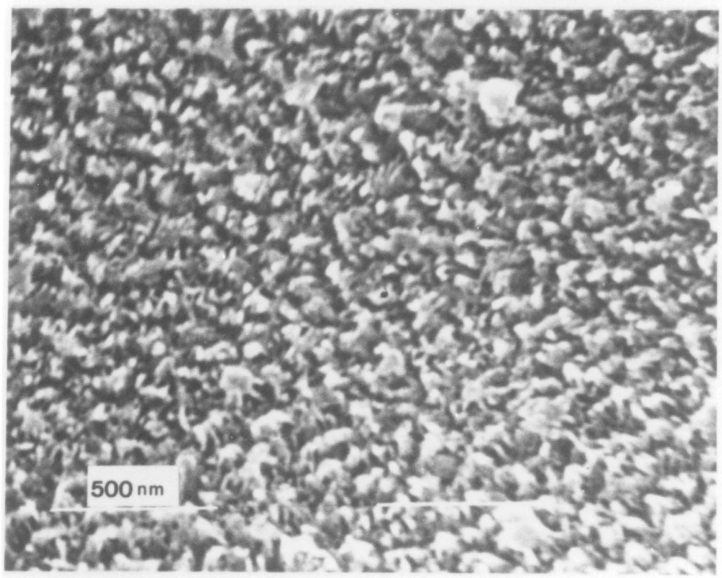

b

Figure 42. HSEM photomicrographs of PAA Al/Li sample a) before 71°C & 100 % R.H. environment, 50,000 X and b) after placing in chloroform for 4 hrs, 50,000 X.

TABLE 25. XPS analysis of 10 % PSF and 0.125 % PSF on PAA surface, placed in 71°C & 100 % R.H. environment for 115 hours and then placed in chloroform to remove PSF.

	10 % PSF		0.125 % PSF	
Photopeak	B.E.(eV)	A.F.	B.E.(eV)	A.F.
C 1s	284.6	0.22	284.6	0.21
O 1s	531.7	0.59	531.9	0.62
Al 2p	73.8	0.18	74.0	0.16
S 2p	167.6	0.005	168.2	0.003
P 2p	133.4	0.005	----	NSP

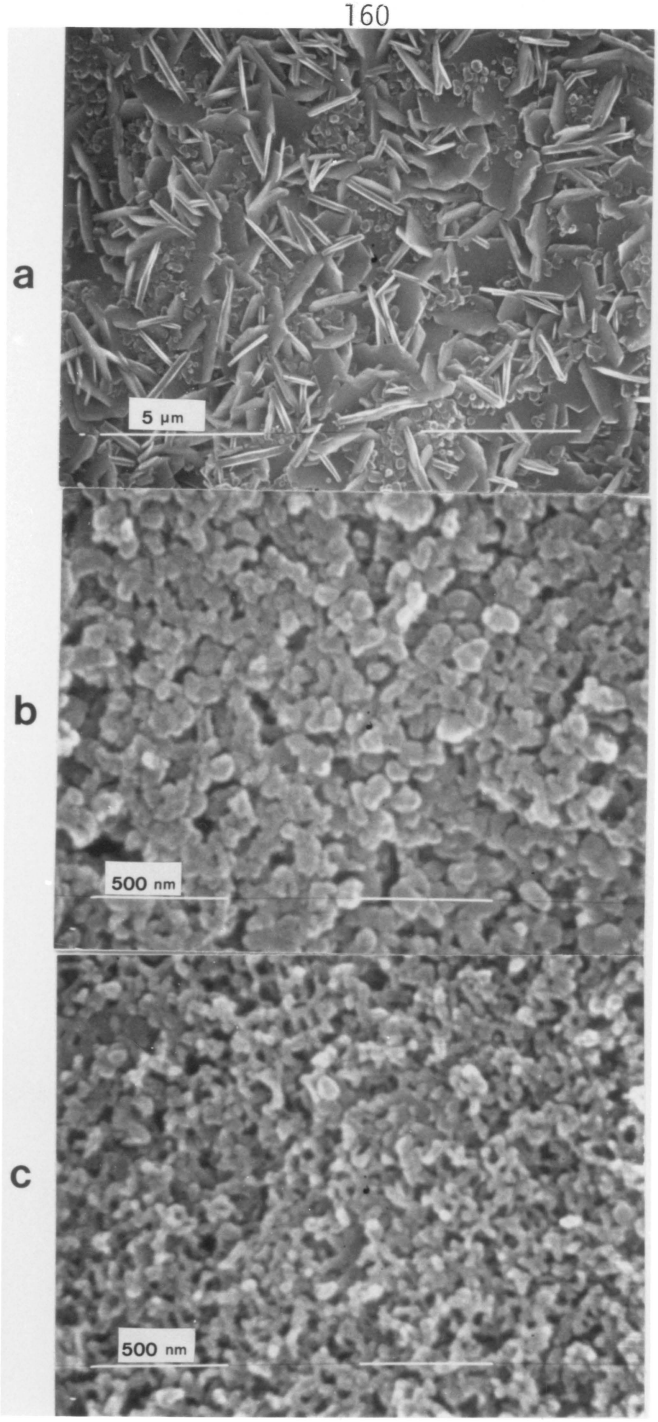

Figure 43. HSEM photomicrographs of a) 0.125 % PSF sample on edge and center, b) 10 % PSF on edge, 50,000 X and c) 10 % PSF on center of the sample, 50,000 X.

water molecules along the interface. Therefore, a new sample preparation in which the PSF thickness from edge to center is constant was done.

C. PSF Coating-Thermal Press

The HSEM photomicrographs of PAA Al/Li samples which were thermally pressed with 76 and 38 μm thick PSF films followed by 96 hours of environmental exposure are shown in Figures 44 and 45. Figures 44a and b show the center and edge of the 76 μm coated sample which showed no signs of hydration at either place. Figures 45a and b show the center and edge of the 38 μm coated sample which again showed no signs of hydration. Therefore, these results indicate that the PSF film is too thick for moisture to diffuse through the PSF film in 96 hrs but more importantly that no moisture penetrated along the oxide/polysulfone interface.

D. PSF Coating-Spin Cast

The HSEM photomicrographs of a PAA Al/Li sample are shown in Figure 46 for a 0.125 % spin coated PSF solution after 15 hours of exposure. Both the edge (Fig. 46a) and center (Fig. 46b) of the sample showed hydration products. The HSEM photomicrograph of a PAA Al/Li sample is shown in Figure 47 for a 0.3 % spin coated PSF solution after 15 hours of environmental exposure. The center and edge of the sample show no hydration products but rather the porous structure characteristic of a freshly anodized surface before environmental exposure. If the moisture had penetrated to the joint by transport along the

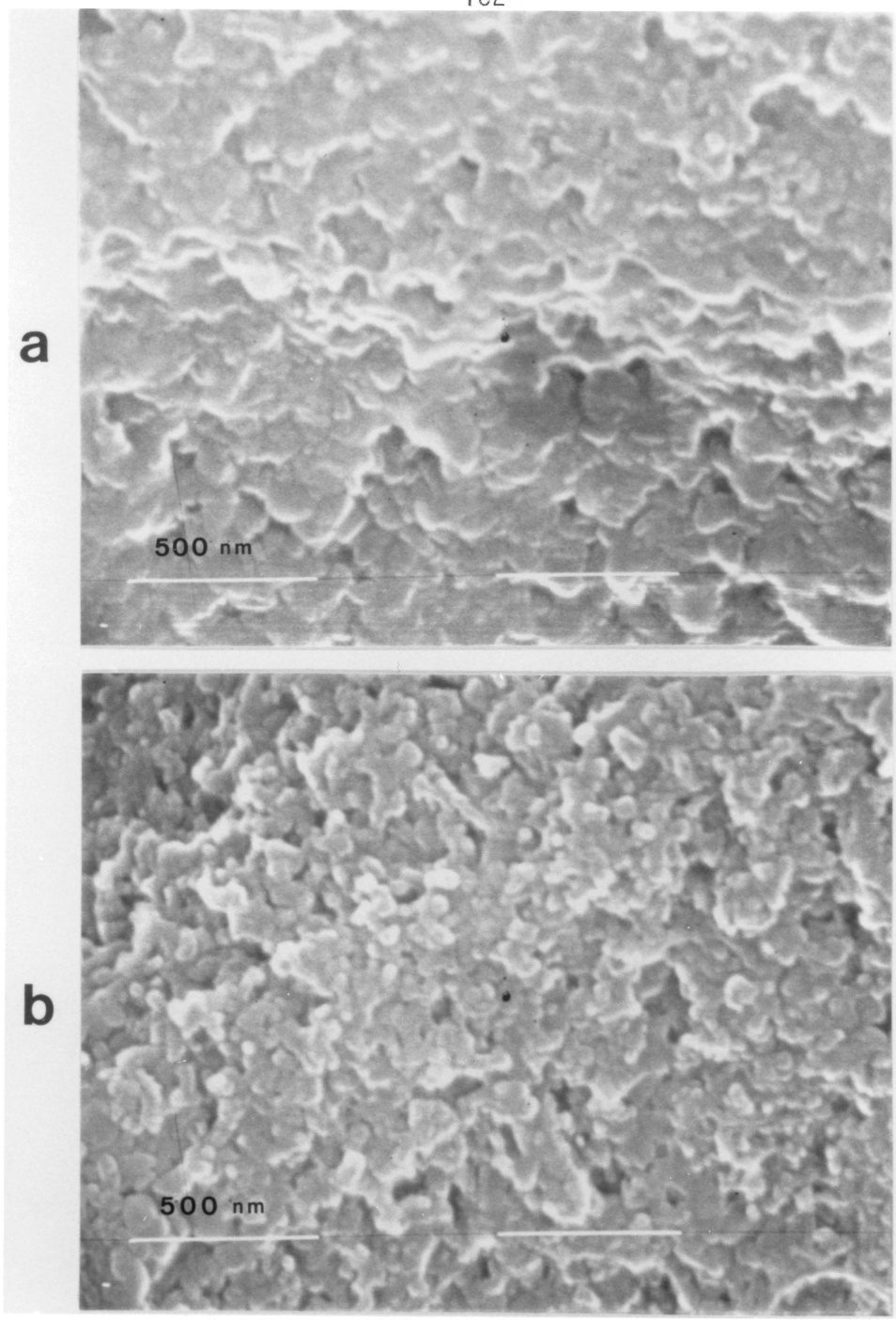

Figure 44. HSEM photomicrographs of 76 μm thick film sample after 96 hrs on a 71°C & 100 % R.H. environment. After chloroform dissolution, a) center of the sample, 50,000 X and b) edge of the sample, 50,000 X.

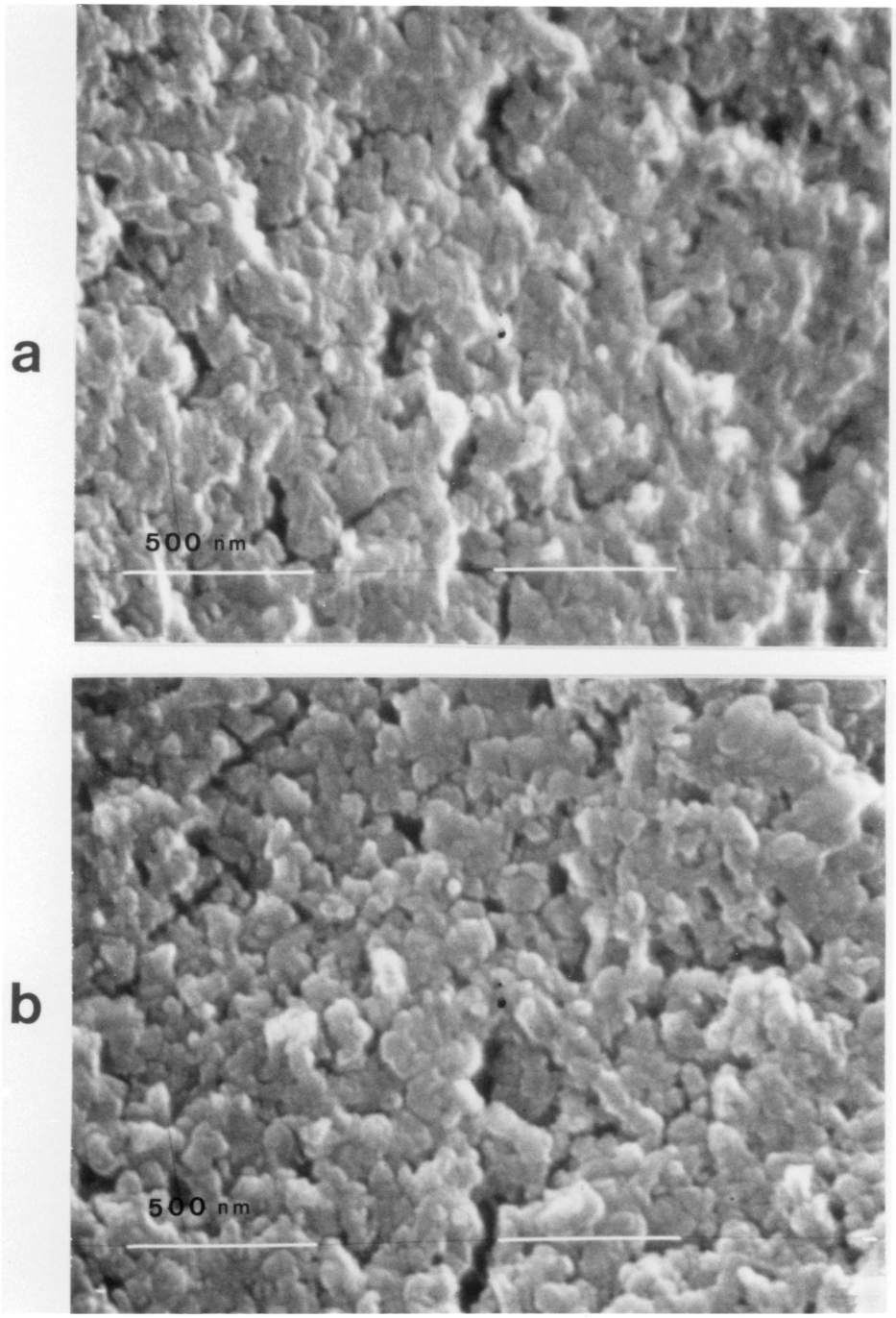

Figure 45. HSEM photomicrographs of 38 μm thick film sample after 96 hrs in a 71°C % 100 % R.H. environment. After chloroform dissolution, a) center of the sample 50,000 X and b) edge of the sample, 50,000 X.

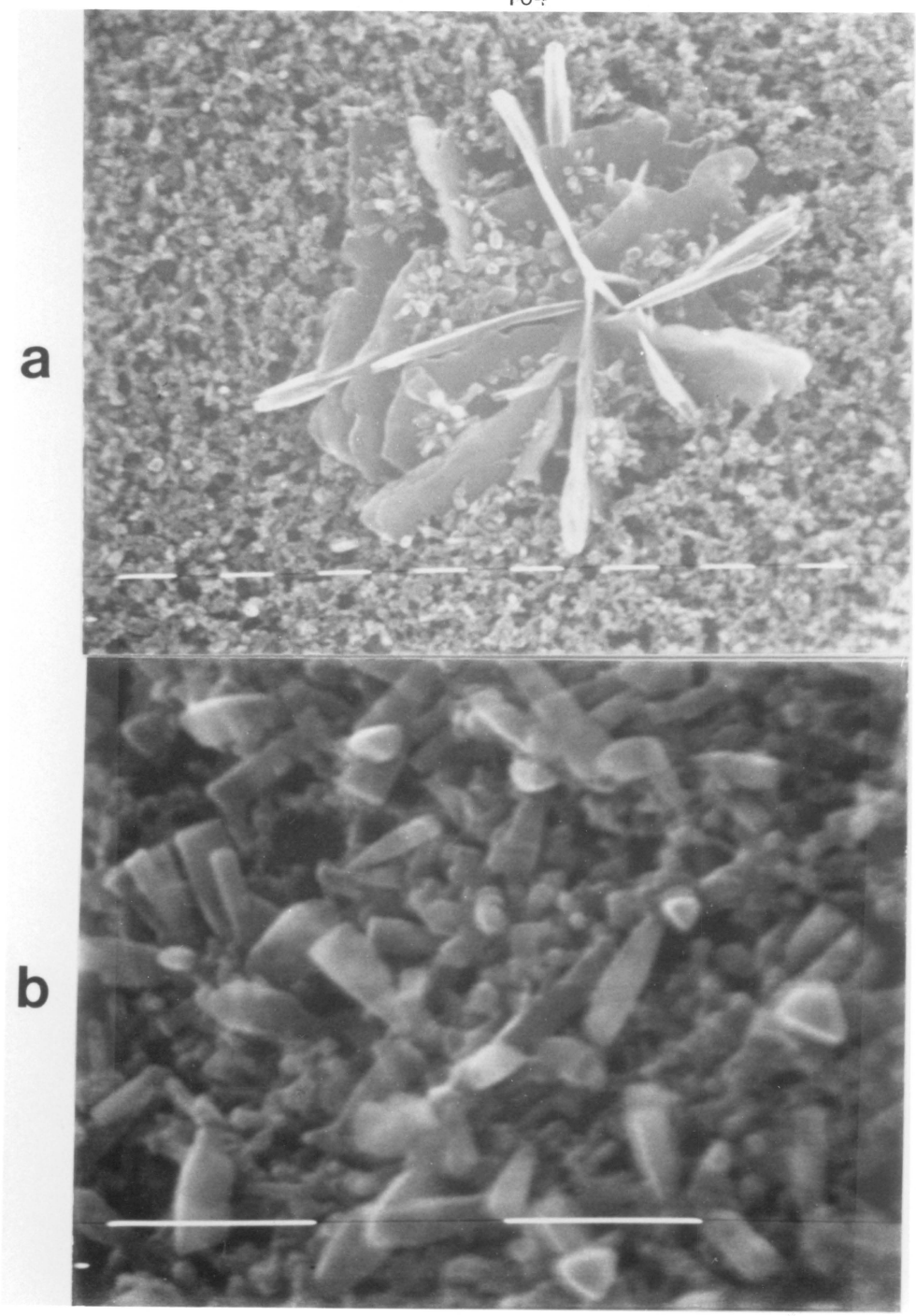

Figure 46. HSEM photomicrographs of 0.125 % PSF coat after 15 hrs in a 71°C & 100 R.H. environment.
After chloroform dissolution, a) center of the sample, 12,500 X and b) edge of the sample, 50,000 X.

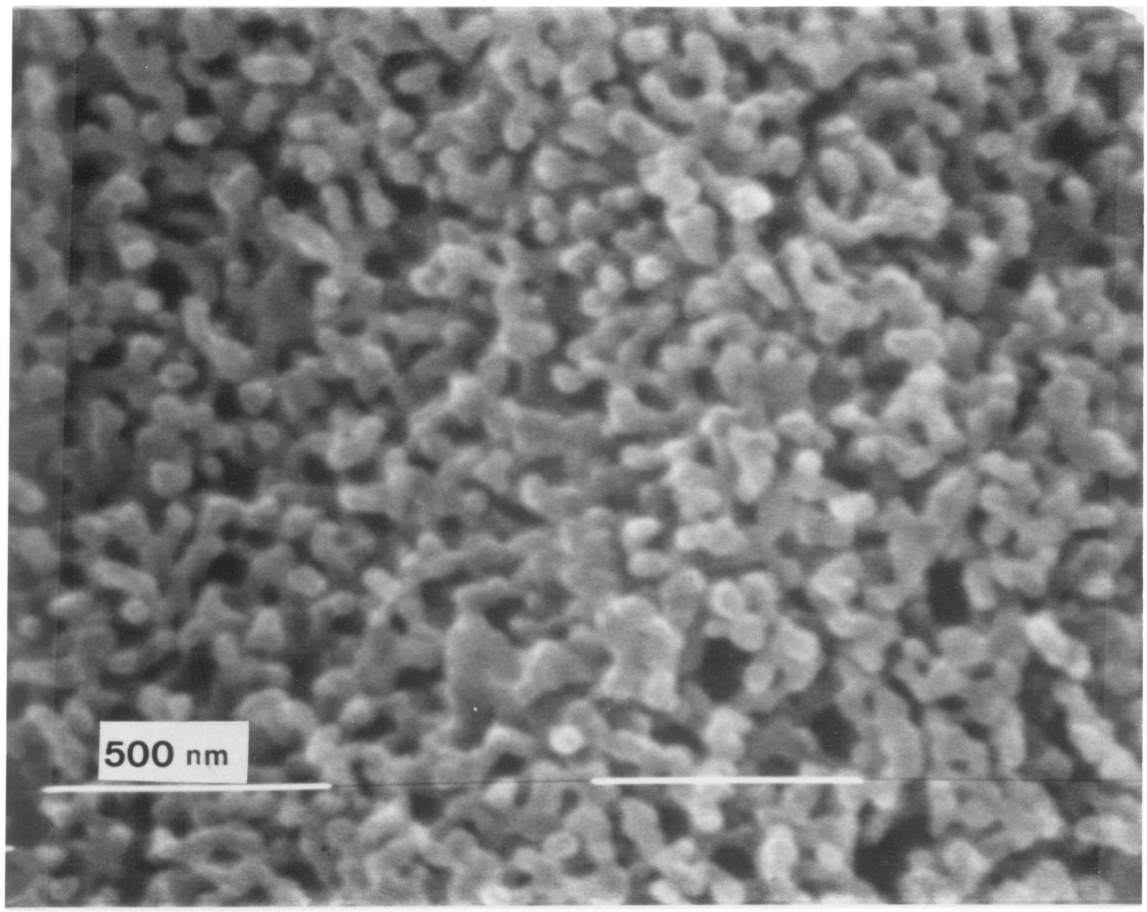

Figure 47. HSEM photomicrograph of 0.3 % PSF coat after 15 hrs in a 71°C & 100 % R.H. environment. After chloroform dissolution center and edge of the sample, 50,000 X.

interface, then the edge side should form hydroxide. Since no hydroxide formation was observed at the edge of the sample, the diffusion of water molecules is through the polysulfone film coating and to the polymer-oxide interface and not by transport along the polymer-oxide interface.

There has been work with the diffusion and/or solubility characteristics of water and other molecules in polymeric materials and the influence of moisture on the properties of polymers (199,200). It is generally believed that the effect of moisture on the polymeric adhesive is to depress the glass transition temperature of adhesives and lower modulus and strength. Water entering a joint may cause swelling and thereby introduce stresses into the joint thus lowering the strength of the bond. These literature investigations have tried to explain the role of chain chemistry in affecting the sorption-desorption process as well as the effect of moisture on polymers. However, such testing cannot give any information on the effect of water at the substrate/adhesive interface but it can be used to screen water sensitive adhesives.

CONCLUSIONS

The goal of this study was to monitor the mode of moisture intrusion into the bondline. The following highlights were noted from this investigation.

1. HSEM photomicrographs for the 0.125 wt. % (115 hr environmental exposure) PSF spin cast sample on the edge and in the center both show hydration products. For the 10 wt. % PSF (115 hr environmental exposure), the sample edge shows signs of hydration whereas the center of the sample does not.
2. HSEM photomicrographs of 0.3 wt. % PSF (15 hr environmental exposure) spin cast samples from the center and the edge show no signs of hydration products. Water molecules diffuse through the polysulfone and then to the polymer/oxide interphase rather than intrusion along that interface.

CHAPTER V

EFFECT OF SURFACE TOPOGRAPHY ON THE RELAXATION BEHAVIOR OF THIN POLYSULFONE COATINGS ON ALUMINUM SUBSTRATE

As discussed in the LITERATURE REVIEW section, various factors are involved in polymer-metal adhesion, for instance, the physical and chemical nature of the metal surface (18,36), the existence of a weak boundary layer (111), and toughening mechanisms as well as the internal stresses of the adhesive (108).

The objective of this investigation is to determine the viscoelastic response of thin polysulfone coatings on pretreated aluminum surfaces using dynamic mechanical thermal analysis (DMTA) and dielectric thermal analysis (DETA). In order to study the interaction of the aluminum oxide layer with polysulfone, XPS was used to investigate properties of the metal-polymer interface by monitoring the energy shift of the core electrons for differently pretreated interfaces. Neat films of polysulfone and thin polysulfone films coated onto a smooth Al substrate and a porous Al substrate were compared. The goal here was to determine whether the polymer which penetrated the porous oxide has a different material property than the polymer in the bulk and an attempt was made to correlate the dynamic mechanical properties to the interfacial bonding characteristics.

EXPERIMENTAL

A. Sample Preparation

1. Polysulfone Samples

A thin (0.260 mm) polysulfone film was prepared by compression molding at 290°C followed by thermal treatment at 215°C for 24 hours in order to eliminate internal stresses due to pressing.

2. Polysulfone Coated Samples

a. Surface Pretreatments

Prior to coating the thin aluminum foil (99.5 % Al) of 0.2 mm thick (Al foil was used because thin Al/Li foil was not available), the samples were pretreated by degreasing and phosphoric acid anodization. The degreasing leaves a smooth surface whereas the PAA treatment leaves a porous surface. These pretreatment procedures are described in Appendix 1 in the Surface Pretreatments section.

b. Spin Coating

Thin PSF films were prepared from solutions in chloroform by spin coating (Photo-Resist Spinner model R485, Headway Research Inc, Garland, TX). Coating thickness was controlled by varying solution concentration as well as the spin coater speed. Samples were annealed at 210° C for 10 min prior to analysis in order to avoid results characteristic of the sample preparation. The DETA samples were thicker than the DMTA samples, and the thickness of the DETA samples was determined by fracturing the polysulfone film in liquid nitrogen after removing the aluminum alloy in 5 % NaOH solution and measuring the

fractured thickness with the SEM.

B. Characterization of Substrate Surfaces.

1. HSEM

HSEM studies utilizing a Philips EM-420T electron microscope is described in Chapter III within the EXPERIMENTAL Section.

2. XPS

The XPS studies using a Physical Electronics ESCA/SAM 550 electron spectrometer with a magnesium anode (1.254 KeV) is described in Chapter III in the EXPERIMENTAL section.

Argon ion beam sputtering was performed in order to remove the polysulfone film from the coated sample and observe the PSF-Al oxide interphase. Ion sputtering was done with 3 kV energy beam of argon ions having a beam current of 30 μA, for successive periods of 5 minutes. The sputtering was continued until both the Al 2p and S 2p photopeaks were detected.

3. Dynamic Mechanical Thermal Analysis (DMTA)

In the dynamic mechanical technique, a small sinusoidal mechanical stress is applied to the sample and the resulting sinusoidal strain detected. Comparison of the amplitude of the signals yields the complex dynamic modulus E* in the bending mode (G* in shear). The phase lag (δ) of strain behind stress allows the complex modulus to be expressed as a storage modulus (E' or G') and a loss (E'' or G'') modulus. Then the mechanical loss tangent,

tan δ is given by,

$\tan \delta = E''/E' = G''/G'$ [27]

From the frequency (f) dependence of the tan δ versus temperature curves, activation energies were calculated using an Arrhenius type equation,

$E^* = d(\log f)/d(1/Tmax)$ [28]

The temperature dependence of the dynamic storage modulus (E'), dynamic loss modulus (E''), and dynamic loss tangent (tan δ) were scanned at 1 deg/min. from 160 to 250 C with a multifrequency (0.3, 3, and 30 Hz) analysis routine for these samples using Polymer Laboratories (Amherst, MA) Dynamic Mechanical Thermal Analyzer (DMTA).

The viscoelastic behavior of polymer system can be explained in the following way. In the simplest terms, the damping (dissipation factor G''/G' or E''/E') goes through a maximum and then a minimum as the temperature is raised for a polymer as shown in Figure 48 (124). At low temperatures, molecular motion of the chain segments is frozen in. Deformation results primarily from the bending of valence angles of the atoms in the polymer chain, so the modulus is high, and the material has nearly perfect elasticity. A perfectly elastic spring stores energy only as potential energy and does not dissipate any of it as heat. Thus, an elastic material or a stiff spring has low damping. At temperatures above the glass-transition region, the damping is low again. A good rubber, like a weak spring, also stores energy without dissipating it into heat. In the rubbery region, molecular segments are not frozen in but are free to move, so the modulus is low. Thus, if chain segments are completely frozen in or are completely free to move, damping is low.

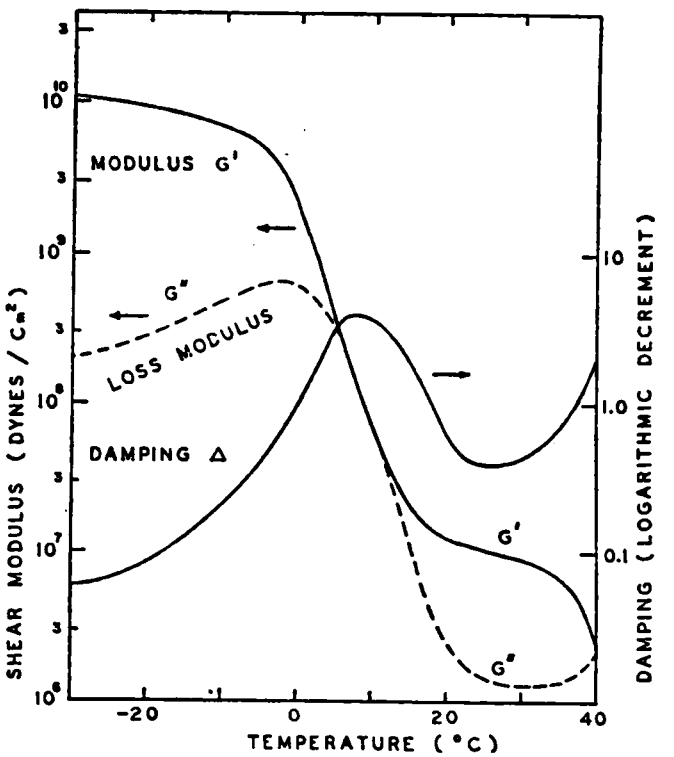

Figure 48. Typical dynamic mechanical behavior of uncrosslinked amorphous polymers. The material is a copolymer of styrene and butadiene (124).

The damping is high in the transition region because some of the molecular chain segments are free to move while others are not. A stiff spring (frozen-in segment) can store much more energy for a given deformation than a weak spring (rubbery segment free to move). Thus, every time it is stressed, a frozen-in segment becomes free to move, and its excess energy is dissipated into heat. One characteristic of the transition region is that part of the molecular segments are free to move, and the longer the time a segment is under stress, the greater is the probability that it will have a chance to move so as to relieve a part of this stress. This delayed response to a stress gives rise to high damping and makes the strain lag behind the stress. The damping peak occurs in the temperature region where many of the frozen-in segments may become mobile in a time comparable to the time required for one oscillation.

The loss modulus G'' goes through a peak (see Fig. 48) at a slightly lower temperature than does the dissipation factor G''/G'. The maximum heat dissipation for a unit deformation occurs at a temperature where G'' is maximum, and the temperature of this maximum at one cycle per second is very close to the value of the glass-transition temperature as obtained by volume-temperature measurements. Generally, the temperature of maximum damping G''/G' is 5 to 15 $^{\circ}$C higher than the conventional glass transition temperature if the dynamic measurements are made at about 0.1 to 1.0 cycle per second. In the following discussion, the temperature at which the damping (G''/G' or delta) is a maximum will be referred to as the

glass transition temperature for convenience.

The temperature at which the damping is a maximum depends on the frequency of measurement. For most polymers, an increase of a factor of ten in frequency will raise the temperature of maximum damping approximately 7 C. Table 26 shows how this temperature shift is a function of the absolute temperature of the glass transition and the energy of activation. Similar results may be obtained from the Williams-Landel-Ferry treatment (120). The close correspondence of the glass-transition temperature and the temperature of maximum damping at low frequencies is one of the important reasons why many dynamic measurements are made at low rather than at high frequencies (124).

4. Dielectric Thermal Analysis (DETA)

In the dielectric technique, a small sinusoidal electric field is applied to the sample and the electric displacement (charge Q) followed. This latter is usually followed via current i which is equal to dQ/dt. The complex dielectric permittivity e* is obtained from the amplitude, and phase measurement allows resolution into the storage part (dielectric constant) e' and the loss part (dielectric loss) e''. The dielectric loss tangent is given as (201),

$$\tan \delta = e''/e' \qquad [29]$$

In the dielectric experiment, the molecules are interacting with an applied electric field, thus coupling can only occur with dipolar or charged species in the polymer. A polymer such as polyethylene should be completely inactive in a DETA scan because it has zero

TABLE 26. Temperature shift factor of damping peak for a decade change in frequency (124).

Temperature of maximum damping T (K)	Energy of Activation ΔH (cal/mole)	Shift in Damping peak per decade change in frequency
200	1×10^4	20
200	5×10^4	4
200	1×10^5	2
200	1×10^4	49
300	5×10^4	8.5
300	1×10^5	4
400	1×10^4	90
400	5×10^4	15
400	1×10^5	7.5

dipole moment and no charge location sites. However, such polymers are normally mildly oxidized and contain ionic catalyst residues. The detection of very low levels of dipolar and ionic impurities is one of the advantages of the dielectric techniques.

The dielectric relaxation processes is well understood theoretically and relates to the extent of freedom attained by dipoles in that process (202). The strength of the relaxation process ($e'_r - e'_u$) is related to the strength of the molecular dipole (u) involved in the molecular motion by the equation,

$$\frac{(e_r' - e_\mu')(e_r' + e_\mu')}{e_r'(e_\mu' + 2)} = \frac{4\pi}{3KT} g\langle\mu^2\rangle \qquad [30]$$

where g is a dipole correlation term. In this equation, e'_r is the dielectric constant at the end of the relaxation process (relaxed) and e'_u is the dielectric constant at the beginning of the relaxation process (unrelaxed). In the mechanical case, unfortunately no such relationship exists relating mechanical relaxation to particular molecular motions.

The dielectric loss factor, $\tan\delta$, was followed as a function of both temperature and frequency with a Polymer Laboratories (Amherst, MA) dielectric thermal analyzer (DETA). Samples were analyzed at minimum voltages (<0.1 volt) in order to avoid dielectric breakdown, and scanned at 4 deg/min. from 160 to 250°C with a multifrequency analysis routine at 0.1, 1 and 10 kHz. The minimum range for tan δ with DETA is 0.001.

RESULTS AND DISCUSSION

A. HSEM Results

The degreased aluminum surface was studied with HSEM in order to determine the surface topography. The resulting HSEM photomicrograph in Figure 49a at 25,000 X revealed that pretreatment of the aluminum surface by just vapor degreasing results in a relatively smooth surface showing some machine rolling marks. Phosphoric acid anodization on the other hand results in a porous surface topography. Figure 49b at 50,000 X shows the fully developed porous oxide layer with pore diameters of approximately 100 nm.

B. XPS Results

1. Neat PSF Film

In Figure 50, both the O 1s and S 2p photopeaks are shown for the different samples studied. The binding energies in eV for each observed photopeak are tabulated along with the calculated values of the atomic percentage in Table 27.

For the PSF neat film, the O 1s photopeak shows a doublet when the peaks are curve fitted (see Fig 50-I a). The peak at 533.2 eV is assigned to the S=O group in PSF, and the other peak at 531.9 eV is associated with the 
-O group in PSF. The carbon 1s peak at 284.6 eV gives a calculated atomic percentage of 79 %. The binding energy of sulfur is at 167.8 eV with an atomic percentage of 2.5 % (see Fig. 50-I b).

The PSF neat film was argon ion beam sputtered and

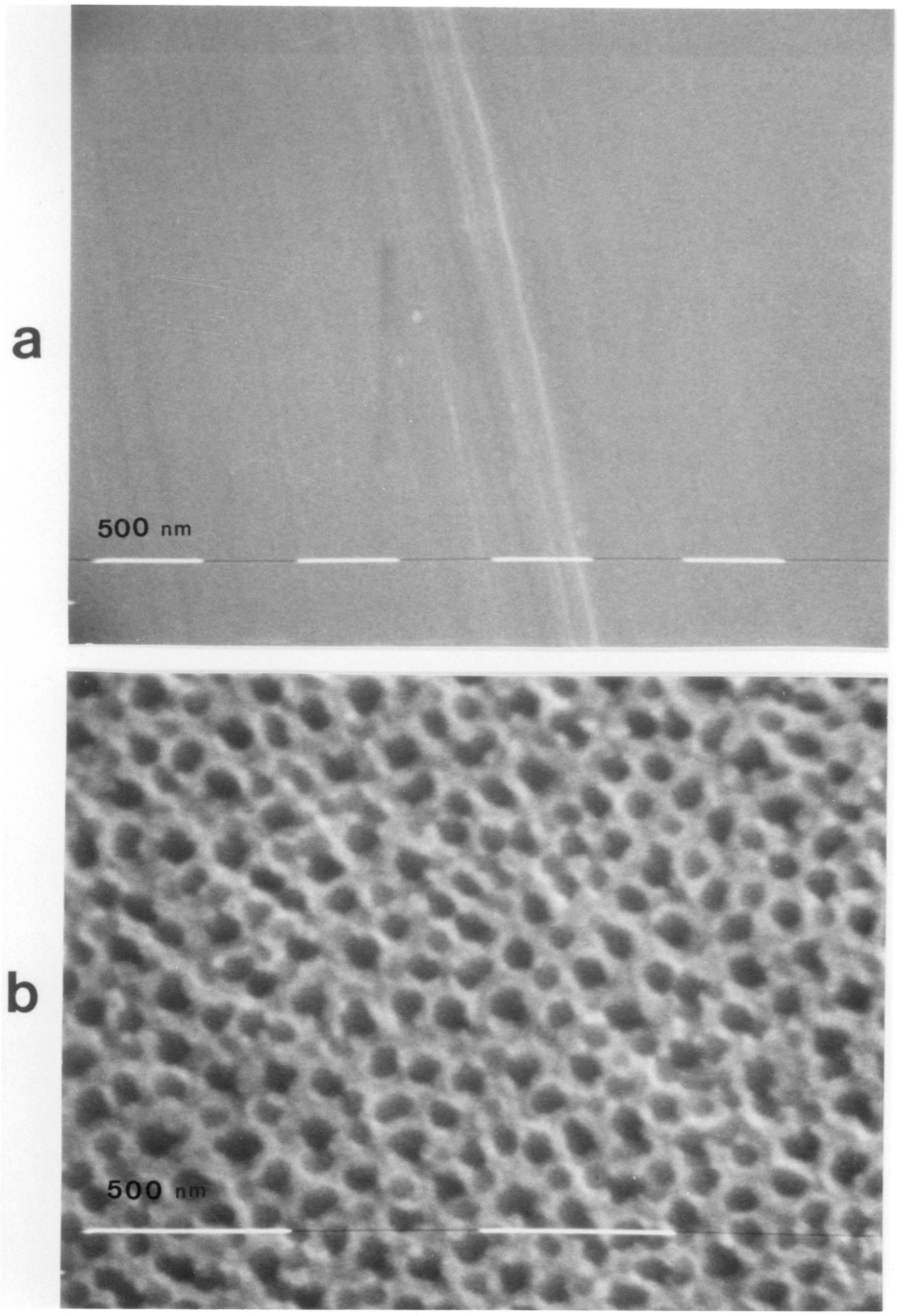

Figure 40. Topography of Al surfaces a) degreased sample, 25,000 X and b) PAA sample, 50,000 X.

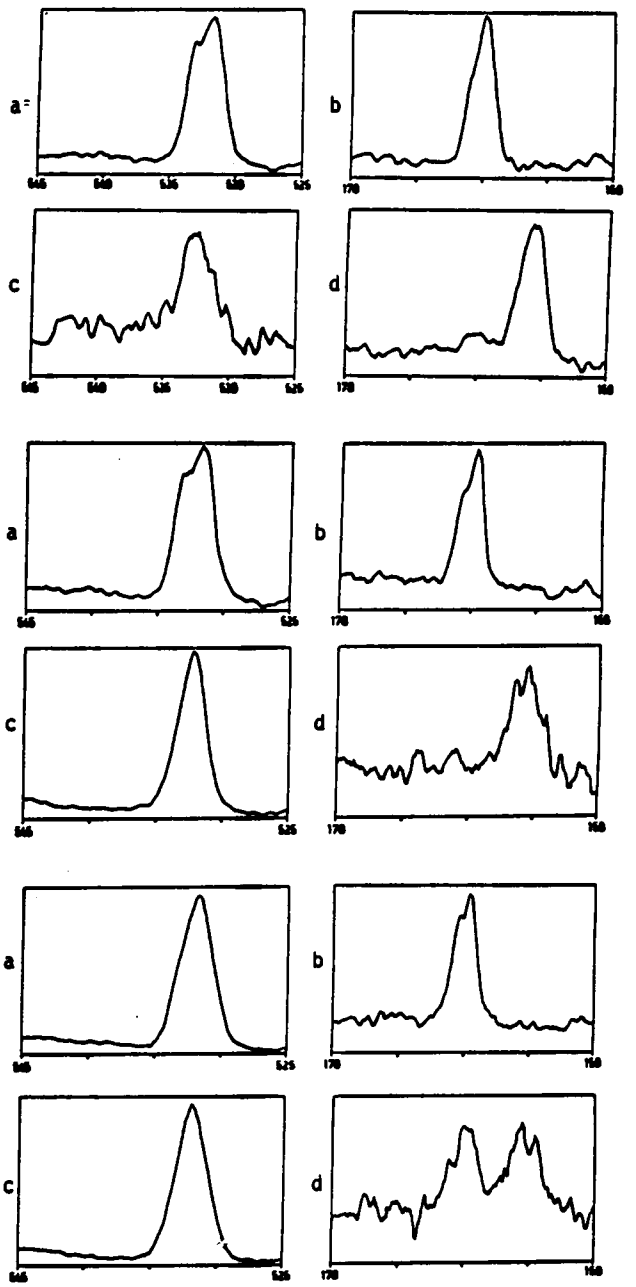

Figure 50. XPS result of O 1s and S 2p photopeaks, I a,b) neat polysulfone film, c,d) after Ar ion beam sputter, II a,b) PSF coating on degreased Al, c,d) after Ar ion beam sputter, III a,b) PSF coating on PAA Al, c,d) after Ar ion beam sputter.

TABLE 27. XPS results of a neat polysulfone film, polysulfone coating on degreased Al, and polysulfone coating on PAA Al before and after Ar ion sputter.

	PSF film			
	Before Ar ion sputter		After Ar ion sputter	
Photopeak	B.E.(eV)	A.F.	B.E.(eV)	A.F.
C 1s	284.6	0.79	284.6	0.94
O 1s	533.2	0.18	532.5	0.04
	531.9			
S 2p	167.8	0.025	163.8	0.02
	PSF coating on degreased Al.			
C 1s	284.6	0.72	284.6	0.52
O 1s	533.2	0.21	532.2	0.27
	531.8			
Al 2p	74.4	0.04	75.4	0.19
S 2p	167.7	0.028	163.3	0.013
	PSF coating on PAA Al.			
C 1s	284.6	0.56	284.6	0.40
O 1s	531.7	0.31	532.0	0.40
Al 2p	74.5	0.11	74.7	0.18
S 2p	167.6	0.02	167.9	0.01
			163.6	
P 2p	134.6	0.01	134.9	0.01

subsequently analyzed by XPS in order to examine any changes induced in the film by the ion sputtering process. It is shown in Fig 50-I d that the binding energy of the sulfur photopeak shifted to 163.8 eV from 167.8 eV suggesting decomposition of the S=O group in PSF by argon ion beam bombardment. Clark et al. (203) has reported similar changes as shown in Figure 51. Here both the F 1s and C 1s spectra of a largely alternating ethylene-tetrafluoroethylene copolymer (52 % TFE) show changes after sputtering with a low energy (2 kV) beam of argon ions having a beam current of 5 μA, for successive periods of 5 sec. It is clear that argon-ion bombardment causes extensive modification within the XPS sampling depth. The main features are as follows. The F 1s signal decreases as does the high binding energy component of the C 1s levels due to CF_2 structural features with a concomitant increase in intensity of a component of intermediate binding energy in the C 1s spectrum due largely to CF-type environments. These preliminary observations are consistent with a cross-linking mechanism in which CH_2 and CF_2 features are converted to CH and CF, respectively. For the polysulfone case, the surface is modified by the argon ion bombardment in which S=O group in polysulfone is decomposed.

2. PSF on Degreased Surface

XPS results for the degreased aluminum sample with 0.1 % PSF coating is shown in Fig. 50-II a,b. The film thickness was 10 nm as measured by ellipsometry on a Ferrotype plate. The XPS result showed a O 1s doublet photopeak with binding energies at 533.2 and 531.8 eV.

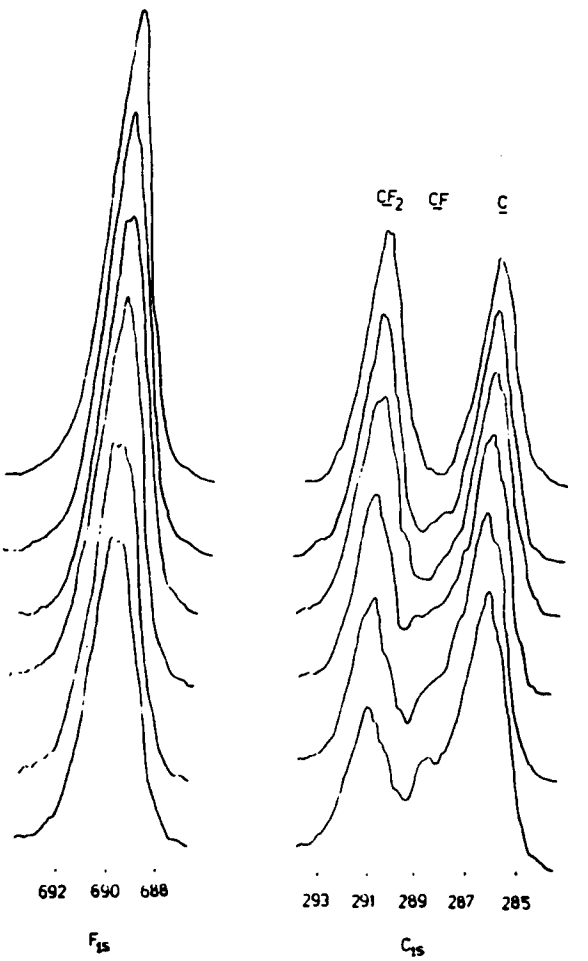

Figure 51. F 1s and C 1s core-level spectra of an ethylene-tetrafluoroethylene (52 % TFE) film before treatment and after successive 5 sec treatments from an argon ion gun (203).

The binding energies as well as the atomic percentages of the C 1s peak and the S 2p peak are similar to the values for the neat PSF film.

When the above coated sample was sputtered with an argon ion beam, the atomic percentage of aluminum in the sputtered sample increased indicating that XPS is probing the PSF-AL interphase region. Also, the oxygen peak is now a single peak (Fig. 50-II c) and the binding energy of the S 2p peak is shifted from 167.8 eV to 163.3 eV (Fig. 50-II d), which resembles the results for a sputtered neat film. The XPS results indicate that the PSF coating covers the smooth surface, and has a uniform thickness throughout the surface. This is clearly shown with SEM photomicrograph as discussed in DETA section.

3. PSF on PAA Surface

A PSF coating 50 nm thick (by ellipsometer on a Ferrotype plate) on a PAA Al surface was analyzed by XPS. The thicker film had to be applied in order to cover the entire porous oxide layer. Prior to sputtering, the Al 2p photopeak assigned to the aluminum oxide is present at 74.5 eV, and the sulfur peak at 167.6 eV is present with atomic percentage of 2.0 %. The P 2p photopeak at 134.6 eV on this surface is from the phosphoric acid used in the pretreatment.

When the sample was sputtered with an argon ion beam, the XPS results were very much the same as the surface before sputtering, except the sulfur peak now has two separate peaks, one at 167.9 eV and the other at 163.6 eV (Fig. 50-III d). The polysulfone film from the top of the pores is changed (S 2p peak from 167.6 eV to 163.6 eV,

Fig. 50-III d) when ion sputtered. However, the peak at 167.9 eV may be due to polysulfone within the porous oxide which was not affected by the sputtering process. Hence it appears that XPS is probing a part of the surface, namely the pores, which is not affected by ion beam sputtering.

From the above analysis, the polysulfone molecules have penetrated into the oxide pores for the case of PAA aluminum sample. Therefore, the polysulfone in the pores which might have somewhat different material properties than the polysulfone in the bulk region was studied here. Polysulfone coatings on a smooth Al surface versus the coatings on a porous Al surface were investigated by using both DMTA and DETA techniques. The same analysis was performed on a neat film and compared to the above two samples.

C. DMTA Results

Figure 52 illustrates how coating in thin layers on PAA aluminum affected the $\tan\delta$ of a polysulfone sample. The thickness of the coated film is 0.35 um. In this case the glass transition temperature was very broad. The DMTA result showed a loss temperature of 188°C for the neat PSF and 195 °C for the PSF film on PAA aluminum surface. Figure 53 shows the Arrhenius plot for polysulfone in different film states. From the slopes of the curves, the activation energy for relaxation can be obtained. The activation energy for the relaxation of the coated PSF on PAA aluminum sample was higher (1250 +/- 152 kJ/mol) than for the neat PSF film (735 +/- 168 kJ/mol). Since DETA

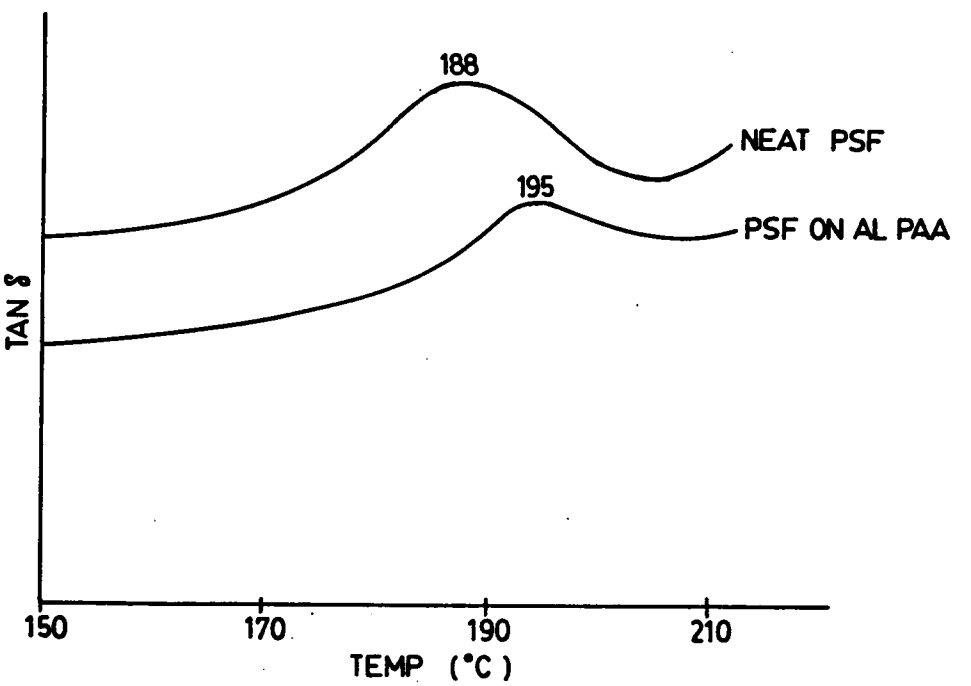

Figure 52. Tan δ versus T for a) neat polysulfone film and b) polysulfone coating on a porous PAA Al surface.

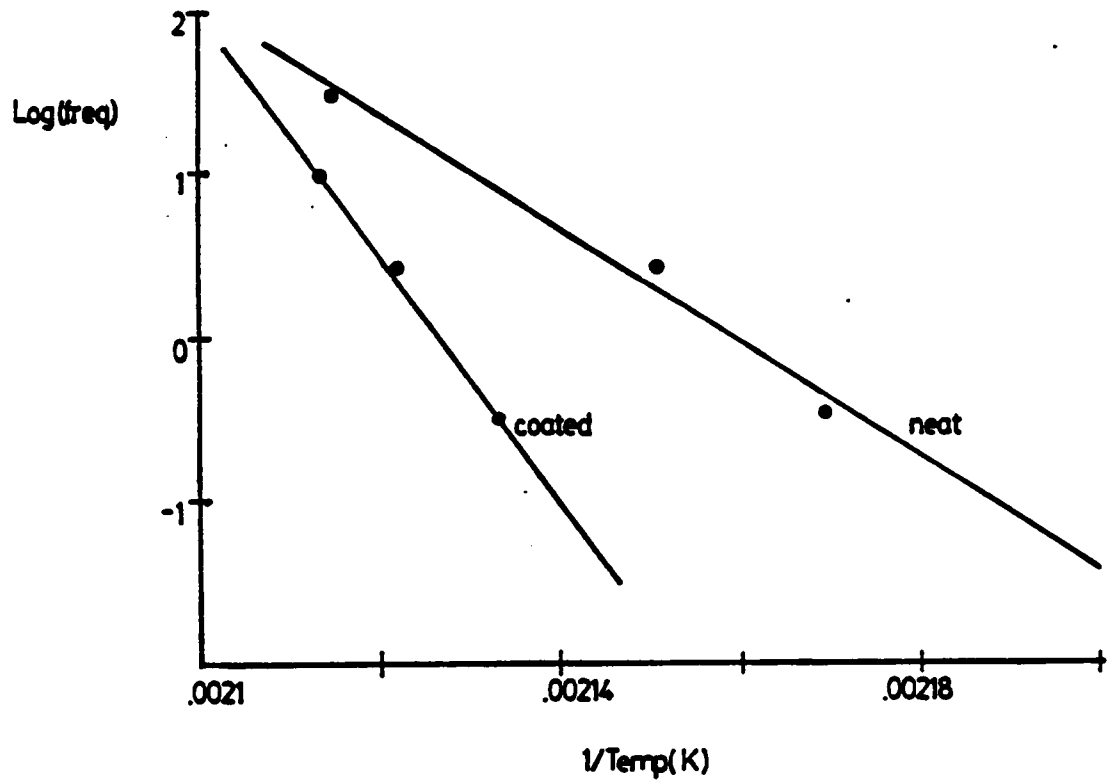

Figure 53. Arrhenius plot for, a) neat polysulfone and b) polysulfone coating on a porous PAA Al surface.

was a better technique in terms of sensitivity for this experiment, further discussion of this behavior is in the DETA section.

D. DETA Results

Before discussion of the DETA results, the thickness of the PSF film is shown in Figure 54. The aluminum substrate was flooded with the 10 wt % PSF solution and spun at 2200 rpm. Different film thickness can be obtained by varying the concentration and the spin coater speed. The polysulfone coating were fractured in liquid nitrogen after removing the Al substrate and the resulting fractured thickness was measured using SEM. The film thickness on degreased Al substrate is shown to be about 2.0 μm (see Fig. 54a). Using the same concentration of PSF and spin coater speed, the film thickness on the PAA Al is about 4.2 μm, which includes the overlayer and the whiskers which penetrated the pores (see Fig. 54b). The whisker diameter is about 100 nm which matches that of the pore diameter. The overlayer film which were on top of the pores is about 2.0 μm thick, the same thickness as the film on the smooth degreased aluminum surface.

The effect of film state was investigated and the dielectric relaxation of neat polysulfone, polysulfone on vapor degreased aluminum, and polysulfone on anodized aluminum was studied. Figure 55 gives the tan δ versus temperature curves for a neat film, 2.0 μm coating on degreased aluminum, and 4.0 um coating anodized aluminum. The Tg of the film on anodized aluminum (210 $^{\circ}$ C) is 10 degrees higher than that of the neat film while the Tg of

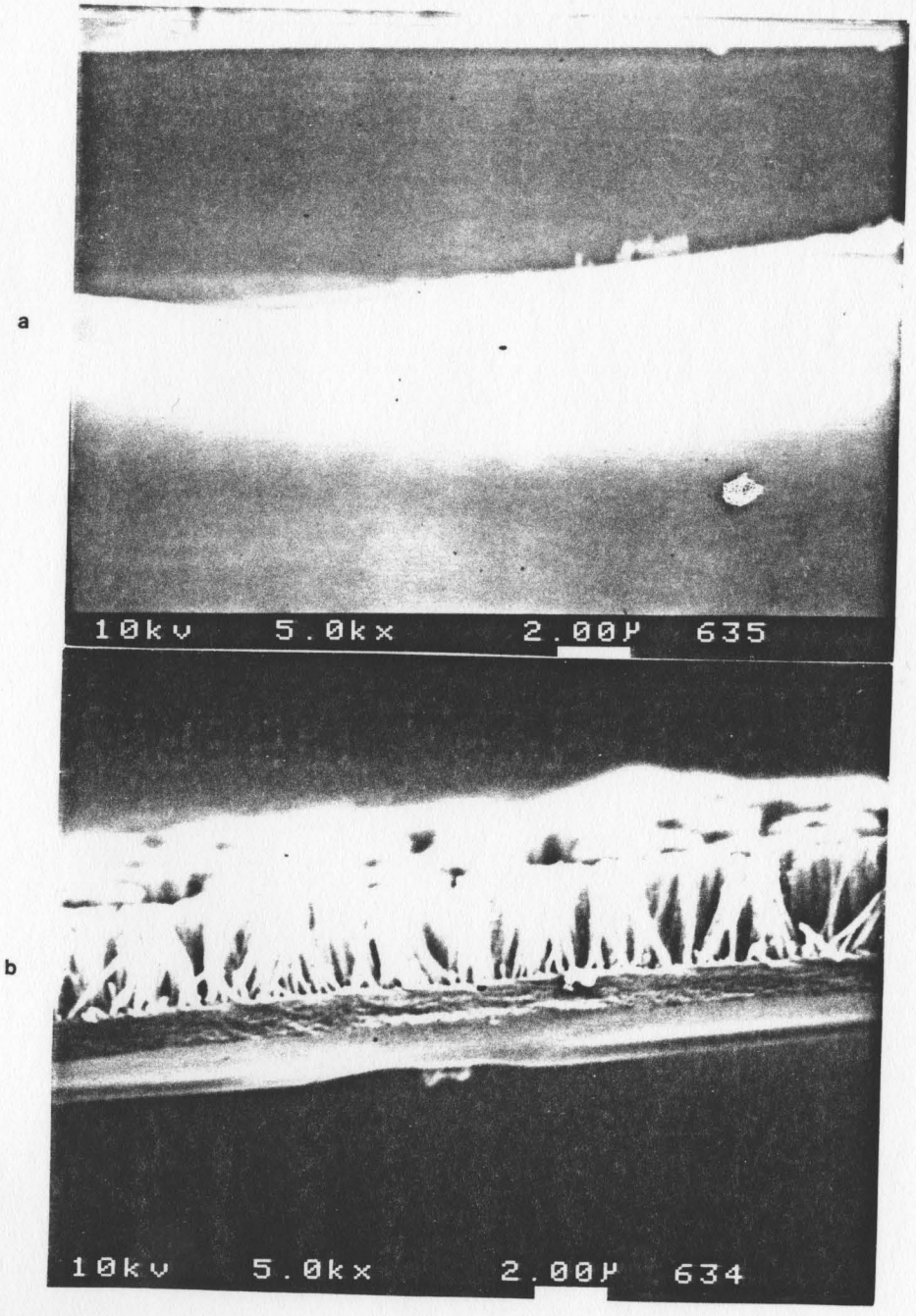

Figure 54. SEM photomicrographs showing the thickness of PSF film coated on a) degreased Al and b) PAA Al.

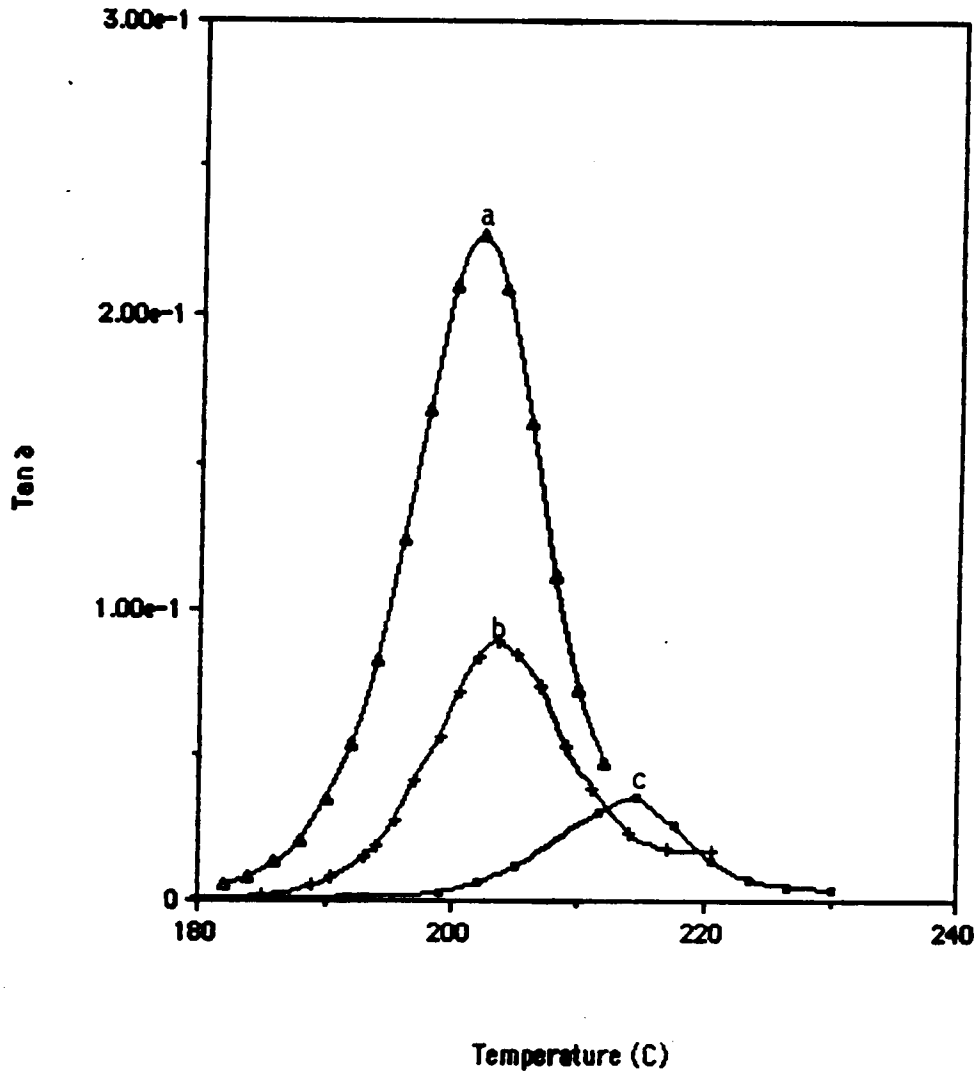

Figure 55. Tan δ versus T for a) neat PSF film, b) PSF coating on smooth degreased Al surface and c) PSF coating on porous Al surface.

the film on vapor degreased aluminum (202°C) is only 2 degrees higher than that of the neat film (200°C). Also, evident from the tan δ curves is the much lower values of tan δ for the polysulfone film on the PAA surface, and the much lower values of tan δ for both the coatings in contrast to the values for the neat film.

Figure 56 is the Arrhenius plot for polysulfone in various film states. The neat film activation energy is compared to coated films: 2.0 μm polysulfone film on degreased aluminum and 4.0 μm film on an anodized surface. It is noted that the activation energy of the film on the porous aluminum surface is much greater (865 +/- 19 kJ/mol) than that of either the film on the smooth-vapor degreased surface (558 +/- 44 kJ/mol) or the neat film (525 +/- 26 kJ/mol). It is evident that the activation energies for relaxation for the coatings are dependent on substrate topography and different from that of the neat film.

Figure 57a and 57b gives the calculated activation energy for polysulfone on degreased, and PAA sample as a function of film thickness. The activation energy decreases as film thickness increases and approaches that of the neat film (525 kJ/mol). Since all samples were annealed prior to analysis, the differences in the Arrhenius activation energy with coating thickness suggest a gradient of relaxation properties in the interphase, which for polysulfone on degreased Al level off and approach that of the bulk or neat film state at around 1.5 μm. For the polysulfone coating on PAA Al, even at thickness of 4.2 μm, the activation energy is higher than

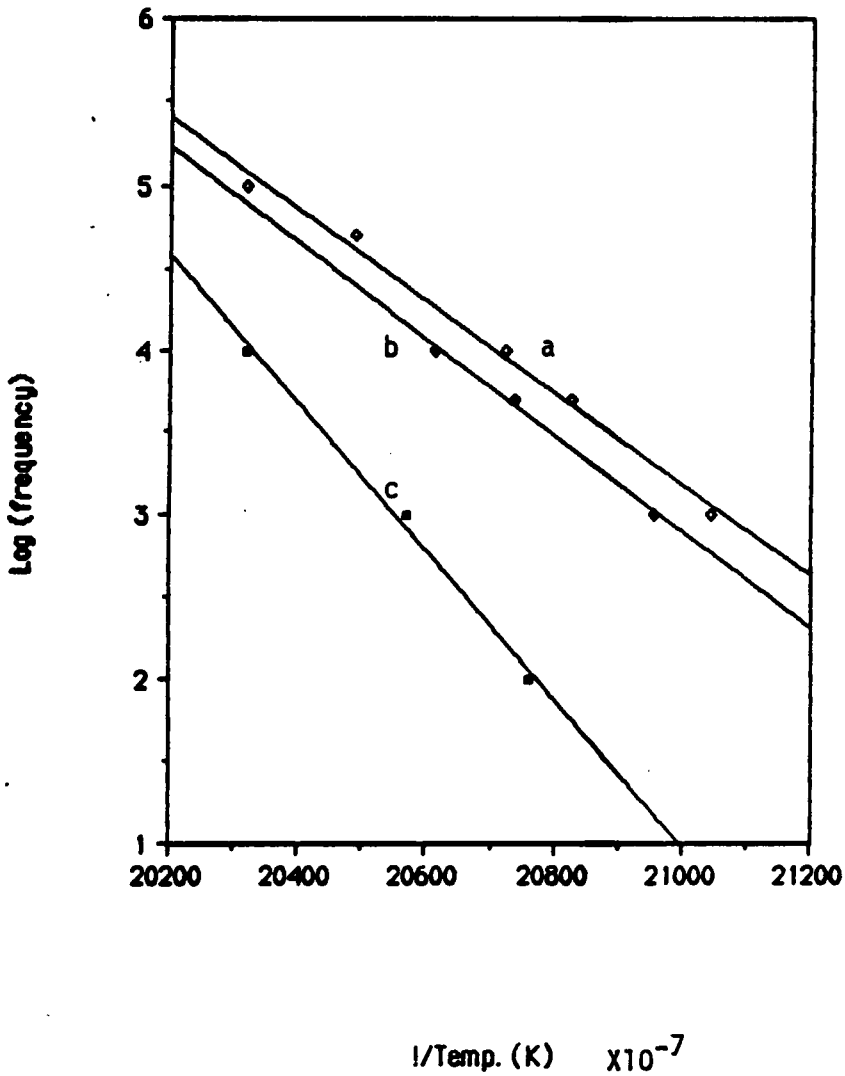

Figure 56. Arrhenius plot for a) neat PSF film b) PSF coating on smooth degreased Al surface and c) PSF coating on porous Al surface.

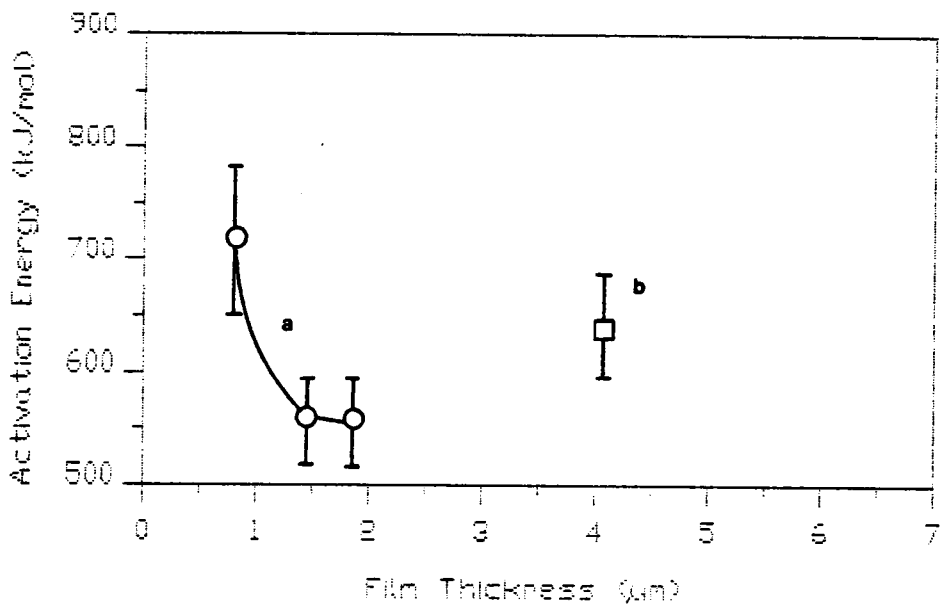

Figure 57. Activation energy versus coating thickness on a) degreased Al and b) PAA Al.

that of the polysulfone film on degreased film at 2.0 μm. This indicates that the restricted layer in the pore region influences further into the bulk film in the case of the PSF film on PAA Al.

The Tg and the activation energy for the relaxation process were highest for the polysulfone film on the PAA surface. It is significant that the magnitude of tanδ was highest for the neat film and lowest for the polysulfone film on PAA aluminum. Since the XPS and SEM results on cast films on Al/Li surface (see Fig. 54b) show penetration of polysulfone into the porous aluminum oxide surface, entropic arguments can explain the higher Tg, higher E*, and lower tan δ for the film coated onto the PAA aluminum surface. This is because for very thin films, if the chains are laid down in two dimensions, entropy would be reduced and the Tg is raised. That is, the adsorption of a macromolecule on a solid surface results in a reduction in the number of configurations the macromolecule can assume when compared to that which exists in the free state. All the bulk polymer molecules are in constant thermal motion. The amplitude of the motion is determined by the amount of available free volume within which they may oscillate, rotate and vibrate. If an adjacent molecule occupies more of its share of the free volume, there is less available for the others. Thus if the sorbed molecule is attached to the active sites of a surface, it usually occurs via specific moieties which are ordinarily displaced some distance from one another, and thus a considerably greater volume is excluded than when it is in the free or unattached state.

The result is a surface molecule which is looped and bent. The movement of the adjacent molecules (those not on the surface) is then restricted. In turn those nearest the adjacent ones are also affected. The restriction could be reflected in glass transition temperature measurements. McLoughlin and Tobolsky (204,205) studied PMMA over the temperature range both above and below the glass transition. They found that stress relaxes more rapidly with a rigid polymer quenched from the melt than from a polymer cooled slowly from the melt. This should be a general phenomenon since the quenched polymer has a larger free volume. The amount of free volume may explain why the energy dissipation (tan δ value) was highest for the neat PSF film when compared to the coated films (see Fig. 55). That is, the thickness of PSF neat film was greater than the thickness of PSF coating on an aluminum substrate.

The relatively immobilized segments in the interface region produce effects similar to that which is observed in cross linked systems. It would appear reasonable at least as a first approximation to expect that the greater extent of hindrance to segmental motion, the stronger the adhesive bond should be. In other words, the thicker the layer of restricted movement the stronger the bond. This is demonstrated in Fig. 57 where the depth of thickness of molecular motion restriction is greater for the PSF on PAA Al than the PSF on degreased Al due to the porous nature of the PAA surface. The restricted movement is reflected in the magnitude of tan δ values as well. The magnitude of tan δ for PSF on degreased and PAA Al was about 0.09

and 0.04, respectively (see Fig. 55). That is the energy being dissipated is higher at the interface if the adhesion is poor. The relationship of strip peeling test to dynamic mechanical tests have been reported by Murayama and Lawton on poly(ethylene terephthalate)-rubber (206), and Chua on glass fiber-polyester (207) system, where the higher peeling load show lower values of tan δ at the glass transition temperature.

The restricted layer may also influence the durability of the polysulfone-PAA aluminum bonds if the main mode of moisture intrusion is by diffusion across the polysulfone as demonstrated in CHAPTER IV. Recall, the mode of failure of PAA Al/Li in 71 °C & 100 % R.H. environment is a cohesive failure with the crack tip occasionally diverging into the interface as shown in Fig. 25b in CHAPTER III. The mechanism of failure was due to moisture which causes the hydration and debonding of PSF from the hydrated oxide layer. Since the moisture has to diffuse across the polysulfone layer and attack the porous oxide, then by having a thick restricted layer present at the interphase region, the moisture penetration into the polysulfone would be delayed and this would improve durability of polysulfone-aluminum bonds in a hot-moist environment. Therefore, this restricted layer is important not only for the initial strength of adhesive bonds, but may play an important role in determining the durability of adhesive bonds as well.

This recent finding is an important one because the correspondence found between viscoelastic response and interfacial topography in PSF-Al/Li interphase is a first

step toward establishing methodologies for studying interfacial properties of polymer composites.

CONCLUSIONS

The goal of this study was to correlate observed DMTA and DETA results with the chemical composition and topographical features of the aluminum foil substrate. From this investigation, the following highlights were noted.

1. The degreased sample had a smooth surface whereas the PAA surface was porous with a pore diameter of approximately 100 nm.
2. The XPS and SEM results revealed that the PSF uniformly coated the degreased substrate, whereas polysulfone migrated into the porous oxide.
3. The Tg of the polysulfone films and activation energy were dependent on the physical state of the film: whether free standing, coated onto a smooth-degreased aluminum surface, or coated onto a porous aluminum surface.
4. The Arrhenius activation energy for relaxation was seen to decrease with thickness and approach that of the neat film at about 1.5 μm for the polysulfone film on a smooth degreased aluminum substrate.
5. The activation energy was higher for the coating on a PAA surface even for a 4.2 μm thick coating, which indicates that the restricted layer in the pore region influences further into the bulk film.
6. The magnitude of the dielectric loss factor of polysulfone was greatest for the neat film and was lowest for the film on the PAA surface. This was due to amount of free volume, which is related to the amount of restricted polymer segments in the film.

7. The difference in the magnitude of the dielectric loss factor of the polysulfone on PAA Al and the polysulfone on degreased Al when compared at same coating thickness can be related to the adhesive bond strength. The restricted layer at the interphase region may influence durability of adhesive bonds as well.

SUMMARY

The overall summary is given below.

1. Lap shear strengths of PAA and SAA pretreated Al/Li samples were slightly greater than those of FPL-etched samples.

2. Wedge test performance on PAA and SAA adherends was superior to that for the FPL etched adherends.

3. The failure path observed with the FPL pretreated samples was at the adhesive/oxide interface.

4. The locus of failure for the PAA and SAA was within the adhesive but the crack occasionally diverged into the oxide.

5. When polysulfone is thermally pressed or primed onto the microporous surface, the polysulfone indeed penetrated into the porous oxide and may have provided a mechanical means of adhesion.

6. The porous structure of anodic oxides on Al/Li formed in both sulfuric acid and phosphoric acid was shown to undergo dramatic changes in morphology after short term (< 90 hrs) exposure to 71°C and 100 % R.H.

7. The morphologically different hydroxides had the same chemical composition when probed by energy dispersive analysis of x-rays. The difference in morphologies was not due to the metal sulfates but may have been due to differences in crystallinity.

8. AES depth profiling showed that Li is not surface concentrated and therefore the effect of Li on bond durability may be minimal. The oxide on Al/Li alloy was thicker than on Al 2024 alloy when the PAA pretreatment

was used.

9. When the bonded joints are failed before environmental exposure either in mode I or mixed mode, the fracture surfaces show no difference in chemical composition or morphological structure.

10. For the cyclic loaded samples, the mode of failure has shifted to mixed mode failure from cohesive failure in the static loaded samples.

11. The failure path for the FPL etched and PAA was both cohesive failure when the wedge test was done at 71 C and 0 % R.H.

12. The DRIFT technique gave no evidence for chemical interaction of polysulfone with the PAA Al/Li oxide layer.

13. HSEM photomicrographs for the 0.125 wt. % (115 hr environmental exposure) PSF spin cast sample on the edge and in the center both show hydration products. For the 10 wt. % PSF (115 hr environmental exposure), the sample edge shows signs of hydration whereas the center of the sample does not.

14. HSEM photomicrographs of 0.3 wt. % PSF (15 hr environmental exposure) spin cast samples from the center and the edge show no signs of hydration products. Water molecules diffuse through the polysulfone and then to the polymer/oxide interphase rather than intrusion along that interface.

15. The degreased sample had a smooth surface whereas the PAA surface was porous with a pore diameter of approximately 100 nm.

16. The XPS and SEM results revealed that the PSF uniformly coated the degreased substrate, whereas

polysulfone migrated into the porous oxide.

17. The Tg of the polysulfone films and activation energy were dependent on the physical state of the film: whether free standing, coated onto a smooth-degreased aluminum surface, or coated onto a porous aluminum surface.

18. The Arrhenius activation energy for relaxation was seen to decrease with thickness and approach that of the neat film at about 1.5 μm for the polysulfone film on a smooth degreased aluminum substrate.

19. The activation energy was higher for the coating on a PAA surface even for a 4.2 μm thick coating, which indicates that the restricted layer in the pore region influences further into the bulk film.

20. The magnitude of the dielectric loss factor of polysulfone was greatest for the neat film and was lowest for the film on the PAA surface. This was due to amount of free volume, which is related to the amount of restricted polymer segments in the film.

21. The difference in the magnitude of the dielectric loss factor of the polysulfone on PAA Al and the polysulfone on degreased Al when compared at same coating thickness can be related to the adhesive bond strength. The restricted layer at the interphase region may influence durability of adhesive bonds as well.

REFERENCES

1. ASTM Glossary of ASTM Definitions, 2nd Ed., American Society for Testing and Materials, Philadelphia, PA, 1973
2. L.H. Sharpe, Aspects of Adhesion, D.J. Alner and K.W. Allen Ed., 7, 139 (1973).
3. Reliability of Adhesive Bonds under Severe Environments, National Materials Advisory Board, National Academy Press, Washington, D.C., 31 (1984).
4. C. Kerr, N.C. MacDonald, S. Orman, J. Appl. Chem., 17, 62 (1967).
5. P. Albericci, Durability of Structural Adhesives, A.J. Kinloch Ed., Applied Science Pub., London (1983).
6. J.D. Venables, Adhesive Joints: Formation, Characteristics, and Testing, K.L. Mittal Ed., Plenum Press, New York, 453 (1984).
7. E.H. Andrews and A.J. Kinloch, Proc. Roy. Soc. A332, 385 (1973).
8. A.N. Gent and A. Ahagon, J. Polym. Sci., Polym. Phys. Ed., 13, 1285 (1975).
9. R. Bailey and J. Castle, J. Mater. Sci., 12, 2049 (1977)
10. I.E. Klein, J. Sharon, A.E. Yaniv, H. Dodiuk, and D. Katz, Int. Adh. & Adhesives, 3, 159 (1983).
11. L. Pauling, The Nature of the Chemical Bond, Cornell University Press, New York, (1960).
12. D.G. Rance, Industrial Adhesion Problems, D.M. Brewis and D. Briggs, Ed., Orbital Press, Oxford, 48 (1985).

13. J.R. Huntsberger, Adhesives Age, 13 (11), 43 (1970).
14. I. Kusaka and W. Suetaka, Spectrochim, Acta., 36A, 647 (1980).
15. D. Tabor and R.H.S. Winterton, Proc. Roy. Soc., A312, 435 (1969).
16. W.C. Wake, Adhesion and Adhesives, R. Houwink and G. Salomon Ed., Elsevier Publishing Co., New York, 1, 375 (1965).
17. J.J. Bikerman, The Science of Adhesive Joints, Academic Press, New York, (1961).
18. J.D. Venables, D.K. McNamara, J.M. Chen, T.S. Sun, and R.L. Hopping, Appl. Surf. Sci., 3, 88 (1979).
19. D.J. Arrowsmith and A.W. Clifford, Int. J. Adh. and Adhesives, 3, 4, 193 (1983).
20. D.E. Packham, Developments in Adhesives - 2, A.J. Kinloch Ed., Applied Science, London, 315 (1981)
21. F. Beuche, W.M. Cashin, and P. Debye, J. Chem. Phys., 20, 1956 (1952).
22. S.S. Voyutskii, J. Adhesion, 3, 69 (1971).
23. S. Wu, H.K. Chuang, and C.D. Han, J. Polym. Sci., Polym. Phys. Ed., 24, 143 (1986).
24. B.V. Deryaguin and V.P. Smilga, Adhesion, Fundamentals and Practice, McLaren, London, 152 (1969).
25. B.V. Deryaguin, N.A. Krotova, V.V. Karassev, Y.M. Kirillova, and I.N. Aleinikova, 2nd Proc. Int. Conq. on Surface Activity-III, Butterworths, London, 417 (1957).
26. C.L. Weidner, Adhesives Age, 6(7), 30 (1963).
27. A. Dupre, Theorie Mechanique de la Chaleur, Gauthier-

Villars, Paris, 369 (1869).

28. T. Young, Phil. Trans. Roy. Soc., 95, 65 (1805).
29. D.H. Bangham and R.I. Razouk, Trans, Faraday Soc., 33, 1459 (1939).
30. D.H. Kaelble, Physical Chemistry of Adhesion, Wiley-Interscience, New York, 144 (1971).
31. F.M. Fowkes, J. Phys. Chem., 67, 2538 (1963).
32. F.M. Fowkes, J. Colloid Interf. Sci., 28, 493 (1968).
33. J. Schultz, K. Tsutsumi, and J.B. Donnet, J. Colloid Interf. Sci., 59, 277 (1977).
34. D.H. Kaelble and K.C. Uy, J. Adhesion, 2, 50 (1970).
35. J.B. Donnet, Pure Appl. Chem., 53, 2223 (1981).
36. J. Schultz, K. Tsutsumi, and J.B. Donnet, J. Colloid Interf. Sci., 59, 272 (1977).
37. R.N. Wenzel, Ind. Eng. Chem., 28, 988 (1936).
38. R.E. Johnson and R.H. Dettre, Contact angle, Wettability and Adhesion, ACS Adv. Chem. Ser., 43, 112, 136 (1964).
39. S.J. Hitchcock, N.T. Carroll, and M.G. Nicholas, J. Mater. Sci., 16, 714 (1981).
40. A. Carre and J. Schultz, J. Adhesion, 15, 151 (1983).
41. J. Comyn, Durability of Structural Adhesives, A.J. Kinloch Ed., Applied Science Pub., London, 85 (1983).
42. R.H. Norman, W.C. Wake, British Plastics Federation, Reinforced Plastics Conference No.4, Paper 1, (1964).
43. V. Stannett, J. Polym. Sci., 16, 81, 89 (1955).
44. N.C. MacDonald, The effect of Moisture on Adhesive bonds, Aspects of adhesion-5, University of London Press, London, 123 (1969).
45. R.A. Gledhill and A.J. Kinloch, J. Adhesion, 6, 315

(1974).

46. R.L. Patrick, J.A. Brown, L.E. Verhoeven, E.J. Ripling and S. Mostovoy, J. Adhesion, 6, 2, 136 (1969).

47. A.J. Kinloch, W.A. Dukes and R.A. Gledhill, Adhesion Science and Technology, L.H. Lee Ed., Plenum Press, New York, 597 (1975).

48. A. Carre and J. Schultz, J. Adhesion, 18, 171 (1984).

49. R.A. Gledhill, A.J. Kinloch and S.J. Shaw, J. Adhesion, 11, 3 (1980).

50. J. Crank, The Mathematics of Diffusion, 2nd Ed., Oxford University Press, Oxford (1975).

51. R.M. Barrer, J.A. Barrie and J. Slater, J. Polym. Sci., 27, 177 (1958).

52. D.M. Brewis, J. Comyn, R.J.A. Shalash and J.L. Tegg, Polymer, 21, 357 (1980).

53. H. Fujita, Adv. Polym. Sci., 3, 1 (1961).

54. E.L. McKague, J.D. Reynolds and J.E. Halkias, Trans. ASME., 98, 92 (1976).

55. K. Nakamura, T. Maruno, and S. Sasaki, Int. J. Adh. and Adhesives, 7, 2, 97 (1987).

56. J. Comyn, D.M. Brewis and S.T. Tredwell, J. Adhesion, 21, 59 (1987).

57. D.M. Brewis, J. Comyn and S.T. Tredwell, Int. J. Adh. and Adhesives, 7, 1, 30 (1987).

58. A. Aitken and R.M. Barrer, Trans. Faraday Soc., 51, 116 (1955).

59. G.J. van Amerongen, J. Polym. Sci., 5, 307 (1950).

60. D.W. Brubaker and K. Kammermeyer, Ind. Eng. Chem., 45, 1148 (1953).

61. H.A. Bent, J. Polym. Sci., 24, 387 (1957).

62. G.S. Park, J. Polym. Sci., 11, 97 (1953).

63. C.E. Rogers, Engineering Design for Plastics, E. Baer Ed., R.E. Krieger Publishing Co. New York, (1975).

64. R. Wegman, Picatinny Arsenal Tech. Rept. 4185, Picatinny Arsenal, Dover, N.J., March (1971).

65. C.U. Ko and J.P. Wightman, J. Adhesion, 24, 93 (1987).

66. J.A. Filbey, J.P. Wightman, and D.J. Progar, J. Adhesion, 20, 283 (1987).

67. T.A. DeVilbiss, D.L. Messick, D.J. Progar, and J.P. Wightman, Composites, 26, 3, 207 (1985).

68. P. Commercon and J.P. Wightman, J. Adhesion, 22, 13 (1987).

69. C. Chang, Surface Sci., 25, 53 (1971).

70. G. Kammlott, Surface Sci., 25, 120 (1971).

71. W.J. Russell and E.A. Garnis, SAMPE Quarterly, 5, April (1976).

72. J.C. McMillan, J.T. Quinlivan and R.A. Davis, SAMPE Quarterly, 5, April (1976).

73. W. Brockmann, O.D. Hennemann, H. Kollek, C. Matz, Int. J. Adhesion and Adhesives, 6, 3, 115 (1986).

74. T. Smith, J. Adhesion, 9, 313 (1977).

75. J.D. Venables, J. Matl. Sci., 19, 2431 (1984).

76. D.J. Packham, Adhesion Aspects of Polymeric Coatings, K.L. Mittal Ed., Plenum, New York, 19 (1983).

77. J.D. Minford, Adhesive Joints: Formation, Characteristics, and Testing, K.L. Mittal Ed., Plenum, New York, 485 (1984).

78. C.W. Jennings, J. Adhesion, 4, 25 (1972).

79. R. Walton, Plating, 3, 219 (1972).

80. N. Rodgers, U.S. Patent, 3,414,489, Dec. 3, (1968).

81. P. Bijlmer, Metal Finishing, 4, 30 (1972).

82. G.S. Kabayashi and D.J. Donnelly, Boeing Co. Rept. No. DG-41517 (Feb. 1974).

83. A. Guntherschulze and H. Betz, Z. Phys., 68, 145 (1931), 92, 367 (1934).

84. E.J.W. Verwey, Physica, 2, 1059 (1953).

85. J.S. Ahearn, T.S. Sun, C. Froede, J.D. Venables, SAMPE Quarterly, 12, 1 (1980).

86. S. Tajima, Advances in Corrosion Science and Technology, 1, M.G. Fontana and R.W. Staehle Ed., Plenum Press, New York, 229 (1970).

87. V.P. Parkhutik, Corrosion Science, 26, 4, 295 (1986).

88. G. Wood, J. O'Sullivan and B. Vaszko, J. Electrochem. Soc., 115, 618 (1968).

89. W. Vedder and D. Vermilyea, Faraday Soc., Trans., 65, 561 (1969).

90. J. Diggle, T. Downie and C. Goulding, Chem. Rev., 69, 365 (1969).

91. R. Harrington and H. Nelson, Trans. Amer. Inst. Met. Eng., 137, 128 (1940).

92. K. Wefers and C. Misra, Alcoa Research Laboratories Techical Paper #19, revised (1987).

93. R.W. Richards, Developments in Polymer Characterization-1, J.V. Dawkins, Ed., Applied Science, London (1978).

94. Rayleigh, Philos Mag., 37, 321 (1919).

95. P.J. Flory, Statistical Mechanics of Chain Molecules, Wiley-Interscience, New York, (1969).

96. P.J. Flory, Principles of Polymer Chemistry, Cornell University Press, Ithaca, N.Y., (1953).

97. H. Benoit, J.P. Cotton, D. Decker, B. Farnoux, J.S. Higgins, G. Jannink, R. Ober, C. Piat and J. des Cloizeaux, Macromolecules, 7, 863 (1974).

98. A. Carre, C. Mazeau and J. Schultz, Proc. Int. Adh. Conf., 1984, The Plastics and Rubber Institute, London, 14.1 (1984).

99. R. Bogue, D. Gamet and H.P. Schreiber, J. Adhesion, 20, 15 (1986).

100. K.L. Mittal, Pure and Appl. Chem., 52, 1295 (1980).

101. W.J. Van Ooij, Surface Sci., 89, 165 (1979).

102. D.M. Brewis, and Briggs, Polymer, 22, 7 (1981).

103. F.J. Boerio, C.A. Gosselin, R.G. Dillingham, and H.W. Liu, J. Adhesion, 13, 159 (1981).

104. W. Brockmann, O.D. Hennemann, and H. Kollek, Int. J. Adh. and Adhesives, 1, 33 (1982).

105. H.T. Hahn, J. Adhesion, 17, 21 (1984).

106. G.C. Knollman, Int. J. Adhesion and Adhesives, 5, 137 (1985).

107. J.D. Andrade, and W.Y. Chen, Surf and Interf. Sci. Analy. 8, 255, (1986).

108. T.C. Ward, M. Sheridan, D.L. Kotzev, Adhesive Joints: Formation, Characteristics, and Testing, K.L. Mittal ed., Plenum Press, New York (1983).

109. M. Sheridan, PhD. Dissertation, VPI & SU, (1985).

110. D.W. Dwight, E. Sancaktar and H.F. Brinson, Adhesion and Adsorption of Polymers, L.H. Lee Ed. Part A, 141, Plenum Press, New York (1980).

111. H. Schonhorn, and F.W. Ryan, J. Poly Sci. Part A-2,

6, 231 (1968).

112. D.M. Brewis, J. Comyn, A.J. Kinloch, D.P. Oxley, R.G. Pritchard, S. Reynolds, and C.R. Werrett, Surf. Interf. Analy., 6, 40, (1984).

113. F.J. Boerio, C.A. Gosselin, Polymer Characterization: spectroscopic, chromatographic, and physical instrumental methods, C.D. Craver Ed., American Chemical Society, Washington, D.C., 541 (1983).

114. M.K. Debe, Appl. Surf. Sci., 14, 1 (1982).

115. J.P. Luongo, and H. Schonhorn, Macromolecules, 2 (4), 366 (1969).

116. B.M. DeKoven, and P.L. Hagans, Appl. Surf. Sci, 27, 199 (1986).

117. P.O. Hahn, G.W. Rubloff, J.W. Bartha, F. LeGouses, R. Tromp, and P.S. Ho, Giess, E.A. ed., Materials Research Society, Symposia Proceeding, 40, 251 (1985).

118. P.S. Ho, P.O. Hahn, J.W. Bartha, G.W. Rubloff, F.K. LeGouses and B.D. Silverman, J. Vac. Sci. Technol. A3 (3), 739 (1985).

119. J.W. Bartha, P.O. Hahn, F. LeGoues, P.S. Ho, J. Vac. Sci. and Technol. A3, 1390 (1985).

120. M.L. Williams, R.F. Landel, J.D. Ferry, J. Am. Chem. Soc., 77, 3701 (1955).

121. I.M. Ward, Mechanical Properties of Solid Polymers, Wiley-Interscience, New York, (1971).

122. F.W. Billmeyer, Textbook of Polymer Science, 3rd Ed. Wiley-Interscience, New York, (1984).

123. J.D. Ferry, Viscoelastic Properties of Polymers, 3rd

Ed., John Wiley, New York, (1980).

124. L.E. Nielsen, Mechanical Properties of Polymers, Reinhold Publishing Corp., London, (1962).

125. O.H. Droste, and A.T. DeBenedetto, J. Appl. Polym. Sci., 13, 2149 (1969).

126. E. Price, D. French, and A. Tompa, J. Appl. Polym. Sci., 16, 157 (1972).

127. K. Iisaki, and K. Shibayama, J. Appl. Polym. Sci., 22, 1845 (1978).

128. J.L. Crowley, and A.D. Jonath, Adhesion and Adsorption of Polymer, Part A, L.H. Lee Ed., Plenum Press, New York, 165 (1980).

129. Y.S. Lipatov, and L.M. Sergeeva, Adsorption of Polymers, John Wiley, New York, 162 (1974).

130. Strength properties of Adhesives in Shear by Tension Loading (Metal to Metal), ASTM D1002-72 (1983).

131. J.A. Marceau, Y. Moji, and J.C. McMillian, Adhesives Age, 10, 28 (1977).

132. Adhesive-Bonded Surface Durability of Aluminum (Wedge Test), ASTM D3762-79 (1983).

133. A. Miller, Boeing Aircraft Company, personal communication

134. J.D. Andrade, Surface and Interfacial Aspects of Biomedical Polymers, Plenum Press, 1, 105 (1985).

135. J.S. Noland, Polymer Science and Technology, L.H. Lee Ed., Plenum Press, New York, 9A, 413 (1975).

136. H.R. Thomas, PhD. Dissertation, Univ. of Durham (1977).

137. D.T. Clark, Characterization of Metal and Polymer Surfaces, L.H. Lee Ed., Academic Press, New York, 2,

5 (1977).

138.T.W. Rusch, Perkin Elmer, Physical Electronics Division, Technical Bulletin, No. 7902 (1979).

139. C.D. Wagner, J. Elec. Spec. Related Phenom., 32, 99 (1983).

140. J.H. Scofield, J. Elec. Spec. Related Phenom., 8, 129 (1976).

141. K.L. Smith and J.S. Hammond, Appl. Surf. Sci., 22/23, 288 (1985).

142. D. Briggs and M.P. Seah, Practical Surface Analysis, Wiley, New York, (1983).

143. G.K. Wehner, Methods of Surface Analysis, A.W. Czanderna Ed., Elsevier, Amsterdam, (1975).

144. T.S. Sun, D.K. McNamara, J.S. Ahearn, J.M. Chen, B. Ditchek, and J.D. Venables, Appl. Surf. Sci., 5, 406 (1980).

145. A. Guinier and D.L. Dexter, X-ray Studies of Materials, Intersciences Publishers, New York, (1963).

146. C.S. Barrett, The Structure of Metals, 2nd ed., McGraw Hill Book Co., New York, (1952).

147. R.C. Furneaux, G.E. Thompson, and G.C. Wood, Corrosion Science, 18, 853 (1978).

148. J.H. Luft, J. Biophys. Biochem. Cytol. 9, 409 (1961).

149. F.J. Boerio, C.A. Gosselin, R.G. Dillingham, and H.W. Liu, J. Adhesion, 13, 159 (1981).

150. J.F. Rabolt, M. Jurich, and J.D. Swalen, Applied Spectroscopy, 39, 2, 269 (1985).

151. R.M. Henry, A.R. Drube, and M.K. Debe, Appl. Surf. Sci., 28, 63 (1987).

152. H.F. Webster, MS Thesis, VPI & SU, (1985)

153. M.K. Debe, Appl. Surf. Sci., 14, 1 (1982).

154. H. Kollek, Int. J. Adh. and Adhesives, 5, 2, 75 (1985).

155. S. Maviroj, J.L. Koenig, and H. Ishida, J. Adhesion, 18, 93 (1985).

156. H.O. Finklea and J.A. Melendez, Spectroscopy, 1, 47 (1986).

157. T.S. Srivatsan, E.J. Coyne, and F.A. Starke, J. Matl. Sci., 21, 1553 (1986).

158. R. Grimes, W.S. Miller, M.A. Reynolds, and A. Gray, 17th National SAMPE Technical Conf., 635, Oct. (1985).

159. B. Nobel, S.J. Harris and K. Dinsdale, J. Matl. Sci., 17, 461 (1982).

160. R.R. Delay, Machine Design, 7, 81 (1985).

161. E.A. Starke and T.H. Sanders, J. Metals, 8, 24 (1981).

162. V. Wigotsky, Aerospace Amer., 6, 74 (1984).

163. R.N. Johnson, Ency. Polym. Sci. and Tech., N.M. Bikales, Ed., Wiley, N.Y., 11, 447 (1969).

164. B.C. Johnson, I. Yilgor, C.Tran, M. Iqbal, J.P. Wightman, D.R. Lloyd, and J.E. McGrath, J. Polym. Sci., Polym. Chem. Ed., 22, 721 (1984).

165. R.N. Johnson, J. Poly. Sci., Part A-1, 5(9), 2375 (1967).

166. R. Viswanathan, PhD. Dissertation, VPI & SU (1981).

167. J.L. Hedrick, D.K. Mohanty, B.C. Johnson, R. Viswanathan, J.A. Hinkley, and J.E. McGrath, J. Polym. Sci., Polym. Chem. Ed., 23, 287 (1986).

168. M.J. Jurek, PhD Dissertation, VPI & SU, (1987).

169. M. Goland and E. Reissner, J. Appl. Mech., 11, 17A (1944).

170. E. Sancaktar, PhD. Dissertation, VPI & SU, (1979).

171. J.A. Filbey, PhD. Dissertation, VPI & SU, (1987).

172. G.D. Davis, T.S. Sun, J.S. Ahearn and J.D. Venables, J. Mater. Sci., 17, 1807 (1982).

173. Perkin Elmer, Handbook of x-ray Photoelectron Spectroscopy.

174. H. Akahori and T. Fukushima, J. Electron Microscopy, 13, 162 (1964).

175. D.H. Kaelble, P.J. Dynes, and E.H. Cirlin, J. Adhesion, 6, 23 (1974).

176. T.S. Sun, J.D. Venables, J.M. Chen, MML TR 80-34C (1980).

177. S. Mostovoy, P.B. Crosley, and E.J. Ripling, J. Matl., 2, 3 (1967).

178. M.H. Stone and T. Peel, RAE Tech Memo MAT 349 (Royal Aircraft Establishment, U.K.), July (1980).

179. K.W. Allen, T. Hatzinikolaou and D.B. Armstrong, Int. J. Adh. and Adhesives, 133 (1984).

180. O.D. Hennemann, personal communication

181. G.D. Davis, J.S. Ahearn, L.J. Mastienzo, and J.D. Venables, J. Matl. Sci., 20, 975 (1985).

182. R.A. Pike, Int. J. Adh. and Adhesives, 1, 3, (1985).

183. R.A. Pike, Int. J. Adh. and Adhesives, 6, 1, 21 (1986).

184. A.J. Kinloch and N.R. Smart, J. Adhesion, 12, 23 (1981).

185. A.J. Kinloch, H.E. Bishop, and N.R. Smart, J.

Adhesion, 14, 105 (1982).

186. J.M Chen, T.S. Sun, J.D. Venables, and R. Hopping, SAMPE 22, 25 (1977).

187. D.J. Field, G.M. Scamans and E.P. Butler, Al-Li Alloys II, T.H. Sanders and E.A. Starke Ed., Met. Soc. AIME, 325 (1981).

188. I.N. Fridlyander, A.I. Litvintsev, R.M. Gabidullin, S.I. Dudkina, L.N. Klimova, and N.V. Shiryaeva, Alyum, Splavy, 5, 335 (1968).

189. K. Wefers and F.A. Mozelewski, Alcoa Technical Report No. 87-58-01 (1987).

190. C.L. Chow and K.M. Ngan, J. Strain Anal., 15, 97 (1980).

191. E.J. Ripling, S. Mostovoy, and R.L. Patrick, Mater. Res. Studs., 64, 124 (1964).

192. A. Anandarajah and A.E. Vardy, J. Strain Anal., 19, 3, 173 (1984).

193. Y.W. Mai, J. Matl. Sci., 13, 2280 (1978).

194. C.L. Chow, C.W. Woo, and J.L. Sykes, J. Strain Anal., 14, 34 (1979).

195. G.C. Mays and G.P. Tilly, Int. J. Adh. and Adhesives, 109, April (1982).

196. J. A. Marceau, J.C. McMillan, and W.M. Scardino, SAMPE 22, 64 (1977).

197. R.M. Silverstein, G.C. Bassler, and T.C. Marrill, Spectrometric Identification of Organic Compounds, 3rd Ed., John Wiley, New York, (1974).

198. M. Auram and G.H. Mateescu, Infrared Spectroscopy, Wiley Interscience, New York, (1972).

199. E. Sacher and J.R. Susko, J. Appl. Polym. Sci., 23,

2355 (1979).

200. V. Stannet and J.L. Williams, J. Polym. Sci., 3, part C, No. 10, 45 (1965).

201. R.E. Wetton, M.R. Morton, A.M. Rowe, American Laboratory, January, 96 (1986).

202. H. Frohlich, Theory of Dielectrics, Oxford University Press, London (1958).

203. D.T. Clark, A. Dilks, H.R. Thomas, Developments in Polymer Degradation-1, Grassie, N. Ed., 87, Applied Science Publishers, London (1977).

204. J.R. McLoughlin, and A.V. Tobolsky, J. Polym. Sci., 7, 658 (1951).

205. J.R. McLoughlin, and A.V. Tobolsky, J. Colloid Sci., 7, 555 (1952).

206. T. Murayama, and E.L. Lawton, J. Appl. Polym. Sci., 17, 669 (1973).

207. P.S. Chua, SAMPE Quarterly, April, 11, (1987).

APPENDIX

A. Surface Pretreatment Procedure

1. Degreasing

Vapor degreasing was done with 1,1,1 trichloroethane for 30 minutes.

2. Forest Products Laboratory (FPL) Etch

The FPL etch pretreatment uses a solution containing 300 ml of H_2O, 55 ml of H_2SO_4, and 25 g of sodium dichromate. The etching procedure consists of heating the fresh FPL etch to 75 °C, then placing coupons in the etching solution to a depth of 3.5 inches for 9 min. After removing the coupons from the etchant, excess etchant is rinsed off with 80°C deionized water. Finally the coupons are air dried and bonded immediately.

3. Sulfuric Acid Anodization (SAA)

For the sulfuric acid anodization, the coupons are vapor degreased with 1,1,1-tetrachloroethane for 30 minutes. The coupons are then alkaline cleaned with 5 % NaOH solution at 70°C for 7 minutes and deoxidized with a dichromate solution of 4 g sodium dichromate, 40 g concentrated sulfuric acid, and 120 g H_2O at 70°C for 10 min. The coupons are anodized in 15 wt. % sulfuric acid solution for 20 minutes with a current density of 12.92 mA/cm^2 (12 amp/ft^2) at room temperature. The apparatus used for anodization is shown in Fig. 58. A

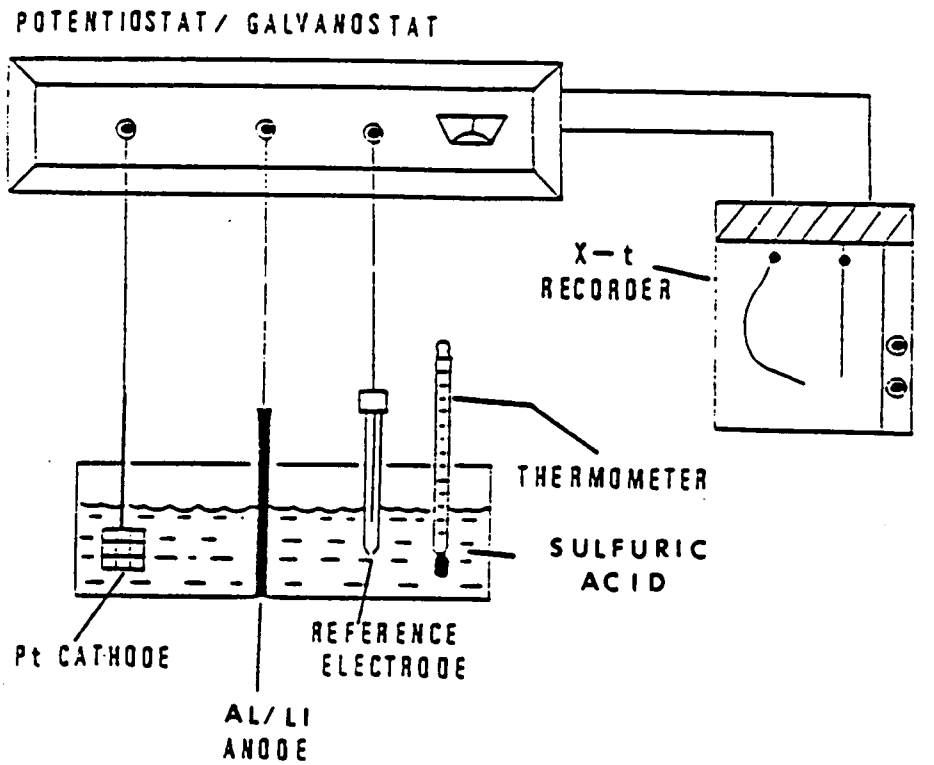

Figure 58. Schematic diagram of anodization apparatus.

potentiostat/galvanostat (Model 173 EG & G / Princeton Applied Research) was used along with an electrometer (Model 178 EG & G / Princeton Applied Research) to provide either constant potential or constant current for the anodization. The voltage and current output was recorded by a Fisher Recordall series 5000 two-pen strip-chart recorder.

4. Phosphoric Acid Anodization (PAA)

Phosphoric acid anodization uses a solution containing 69.54 ml of H_3PO_4 (85%) and 1000 ml of H_2O to prepare a 10 wt. % solution. The surface pretreatment procedure is the same as SAA except that the anodization is carried out in phosphoric acid with constant current density of 6.5 mA/cm^2 (6 A/ft^2). The apparatus used for anodization is the same one used for SAA.

B. Priming Procedure

1. Polysulfone Primer

The primer is prepared by dissolving 3 wt. % of polysulfone in chloroform. The solution was heated to 35 C with hot plate and stirred for 1 hour to completely dissolve the PSF. After the polymer has dissolved in the chloroform, then the primer is brushed on the pretreated surface four times to insure a good primer coating.

2. Aluminum Alkoxide Primer

The inorganic primer was formed by applying a 1 wt % toluene solution of aluminum alkoxide (sec-butyl) E-8385 [Stauffer Chemical Co.] to PAA pretreated Al/Li surfaces.

The alkoxide was converted to an oxide primer by solvent evaporation at room temperature. The aluminum alkoxide primer was coated 6 times to ensure complete coverage of the surface.

C. Bonding Procedure

After pretreatment of the Al/Li alloys, the coupons are bonded. For either lap shear and wedge specimens, the press was pre-heated to 288 C. The jig with the coupons ready to bond with the polysulfone film is inserted between coupons in the press. Both the lap shear and wedge sample bondline thickness was controlled with a 0.1 mm (4 mil) wire spacer. The press was heated to 288 C at 0 MPa for 3 minutes. The pressure was increased to 179.4 MPa (26,000 psi) and held at this pressure for 10 minutes. After 10 minutes, the jig was cooled to 77 C under pressure and the bonded coupons removed from the jig.

The vita has been removed from the scanned document